FE simulation of the SPR process to predict joint characteristics

Engineering Doctorate Portfolio:
Innovation Report

by

Mario Carandente

01/12/2016

Abstract

Self-pierce riveting (SPR) is the core joining technology used by Jaguar Land Rover (JLR) to join aluminium & mixed material body in white (BIW). Currently, the application of this process has a serious constraint to the business due to the high investment and intensive labour required by physically testing joint feasibility. This is a critical issue especially where different stacks need to be joined by one SPR gun. In this case, the selection of a common rivet/die combination which suits different material stacks requires labour intensive work that in some cases can create long delays during a vehicle development and commissioning. In this context, the development of a simulation technique, based on Finite Element Analysis (FEA), could allow virtual assessment of the manufacturing feasibility of a joint. This will enable significant business benefits including: saving time, costs and materials requirement for the experimental trials.

Three major challenges need to be addressed: short CPU time, accuracy and robustness in order for its application in a manufacturing environment**.** To achieve these objectives, detailed numerical methods capable of reproducing the key factors affecting the experimental process like tooling, boundary conditions and material plastic deformation are developed. For the first time, a thermo-mechanical finite element model for simulation of the SPR process has been proposed. This allowed consideration of the increase in temperature due to friction and plastic deformation generated during the rivet insertion. The effect of thermal softening and strain hardening were characterized for the development of the substrate material model and their influence on the numerical simulation was assessed. This study has been validated via production line data and a significantly high level of correlation between simulation and experimental data for over 1000 joints representative of a vehicle platform has been achieved.

The application of the developed simulation technique will enable several business benefits such as significant reduction of engineering time and costs in contrast to the experimental procedure. These advantages allow a smooth implementation of the SPR process in a JLR production line by providing engineering recommendations rapidly and consistently. All these features, combined with accuracy and robustness have enabled the application of the developed tool into JLR business.

Declaration

This innovation report is submitted to the University of Warwick in support of my application for the degree of Engineering Doctorate. It has been composed by myself and has not been submitted in any previous application for any degree. The work presented (including data generated and data analysis) was carried out by the author.

Acknowledgements

I would like to express my deepest gratitude to my industrial supervisor Dr. Li Han for her support, guidance and mentoring during my study. I also would like to thank my academic supervisors Dr. Iain Masters, Prof. Barbara Shollock and Prof. Richard Dashwood.

Much gratitude to Mr. Mike Shergold for recruiting me in the EngD programme and to all my colleagues at Jaguar Land Rover in the AME joining department for their support. In particular, I would like to say thank to Eddie Latimer and Dean Homewood for supporting me during the industrial trials.

Finally a sincere thanks to my parents and my girlfriend for giving me the drive and motivation to complete the project.

Table of Contents

List of Figures

List of Tables

Abbreviations

SPR	Self-pierce riveting
JLR	Jaguar Land Rover
FEA	Finite Element Analysis
BIW	Body in white
DIC	Digital image correlation
RSW	Resistance spot welding
AB	Adhesive bounding
CPU	Central processing unit

1. Project background

Joining materials has always been considered one of the most critical aspects of a manufacturing process. In the most common definition, a joining process consists in bringing together similar or dissimilar materials in order to create a continuous body or a unit (Messler, 2004). Nowadays, the development of new materials is pushing toward the application of new joining technologies. The latter is extremely important for the automotive industry which is currently focussed on lightweight vehicles to enhance both fuel efficiency and driving performance. Weight saving is normally achieved by replacing current high density materials, mainly used for the automotive BIW structures, with light-weight materials such as aluminium alloys, magnesium alloys, high strength low alloy steels and carbon fiber reinforced plastics (Mayyas *et al.*, 2011). However, the substitution of conventional steel with light-weight materials requires the development of new joining technologies. Even though spot welding is recognized as the conventional joining technology for the BIW assembly, several issues have been observed when welding light-weight materials such as aluminium alloys. Therefore, in order to allow the development and the subsequent application of new materials, developing new ways of joining is of primary importance for the automotive industry.

SPR has been the core joining technology for JLR lightweight vehicle manufacturing since 2003. Although, this technology has been also employed by several OEM's due to the capability of joining dissimilar metals with different surface coatings, the implementation of this process in a large scale production environment can be a serious constraint to the business. The main challenge of the SPR process is the requirement of a fixed rivet/die combination for a specific material stack owing to the inflexibility of changing rivet and die during application. Moreover, due to the demands for slower cycle time, reduced capital investment and design requirements for more materials and thicknesses flexibility, different stacks made of different material grades and thicknesses need to be joined by the same SPR gun. As a result, extensive experimental trials need to be conducted in order to assess the feasible rivet/die combinations and to assign the right combination to a BIW assembly facility. In addition, the lack of reliable non-destructive tests (NDT) makes the experimental trials even more labour intensive and prone to inaccuracy due to the necessity of cross-sectioning and subsequent measurements of joint characteristics. This has always presented issues to the business, such as time required for the experimental tests which can

delay engineering decisions, the demands in investment for equipment, materials and labour resource, etc. Therefore, having a virtual tool, which enables simulation of the SPR process and prediction of the joint characteristics, will allow reduction in investment costs and engineering time together with a smother implementation of the SPR process in a production line.

1.1 Objectives of this research

The aim of this study is to develop a simulation technique capable of simulating the plastic deformation during the SPR process and of producing cross-sections of the joints for prediction of joint characteristics.

The model must address three major challenges in order to enable its application in a manufacturing environment: short CPU time, accuracy and robustness.
To allow a short CPU time which is at least comparable with the time required for experimental testing, investigation of suitable mesh sizes and re-meshing techniques are required.
To enable accuracy, the development of detailed numerical methods, capable of reproducing the key parameters affecting the experimental process such as boundary conditions, tooling and material plastic deformation is required. Finally, in order to prove the robustness of the developed simulation technique, its validation needs to be provided based on a JLR vehicle platform in order to reflect the large variety of different rivet/die combinations and stack configurations typical of BIW assembly complexity.
To achieve these objectives, the following items have to be addressed:

- Development of boundary condition for FEA simulation
- Development of mesh parameters and friction coefficients
- Development of material models
- Validation of the method using a JLR vehicle platform

1.2 Portfolio and structure of the report

Chapter 1 has discussed the motivation and industrial relevance of this Engineering Doctorate project.

Chapter 2 provides a brief literature review on the conventional joining technologies used in automotive industry with focus on SPR and the current methods developed for the FE simulation.

Chapter 3 states the methodology used in this research.

Chapter 4 discusses the development of the finite element models with respect to input parameters such as boundary conditions, mesh parameters and friction coefficients.

Chapter 5 describe the application of a thermo-mechanical analysis for SPR simulation.

Chapter 6 investigates the development of material models for AA5754 and AC600T4 aluminium alloys

Chapter 7 reports the validation of the simulation technique using a JLR vehicle platform

Chapter 8 states the business benefits and dissemination of this research

Chapter 9 and 10 provides the conclusions and proposed future work

Table 1 lists the portfolio submissions completed during this project:

Table 1: Portfolio submissions and correlation with the sections in this document

Submission N°	Portfolio Submission Title	Innovation report section
1	Literature review: Introduction to Self-Pierce riveting and finite element analysis	1,2
2	Development of a finite element method for simulation of the SPR process	4,6
3	Experimental and numerical investigation of the temperature generated during the SPR process	5
4	Improvement in numerical simulation of the SPR process using thermo-mechanical finite element analysis (published in Journal of Material Processing Technology)	4,6
5	Experimental and numerical investigation on the rivetability of a 6xxx – T4 aluminium alloy	6
6	Innovation Report	
7	Personal profile	7

2. Literature review

2.1 Introduction

Due to environmental concerns, the automotive industry has been pushed toward a global challenge that involves the reduction of fuel consumption and carbon dioxide emissions while keeping customer expectations. In this context, the use of lightweight materials to reduce vehicles mass has been considered one of the most effective solutions (Davies, 2012a).

As reported by (Mayyas *et al.*, 2011) a weight reduction of 10% can guarantee an improvement of 5% in terms of fuel efficiency. Therefore, as BIW and closures account for more than 30% of the total vehicle weight (Figure 1), these represent the principal areas where the automotive industry is mainly focused to guarantee a significant weight reduction.

Approximate vehicle mass breakdown[a]	System	Major components in system
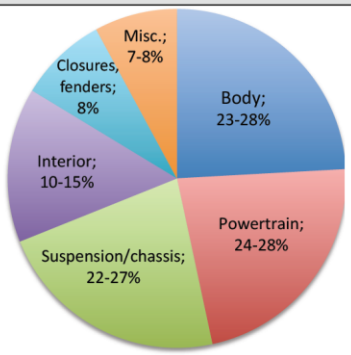	Body-in-white	Passenger compartment frame, cross and side beams, roof structure, front-end structure, underbody floor structure, panels
	Powertrain	Engine, transmission, exhaust system, fuel tank
	Chassis	Chassis, suspension, tires, wheels, steering, brakes
	Interior	Seats, instrument panel, insulation, trim, airbags
	Closures	Front and rear doors, hood, lift gate
	Miscellaneous	Electrical, lighting, thermal, windows, glazing

Figure 1: Vehicle mass breakdown by system and components (Luytsey, 2010)

However, the selection of lightweight materials in a vehicle BIW is not a trivial aspect; it may require not only different approaches on the vehicle design but also new manufacturing technologies including new joining methods (Mori *et al.*, 2013). In this context, JLR has been one of the leading car manufacturers using aluminium alloys for its body structures since 2003 when the first aluminium Jaguar XJ was launched. As shown in Figure 2, the BIW of the Jaguar XJ is characterized by 90% of aluminium stamping parts which are made of 5xxx and 6xxx series aluminium alloys. Aluminium castings and extrusions were also used respectively for the shock towers and front beams whilst a magnesium casting was used for the dash structure. Despite the aluminium architecture enabling significant weight savings in comparison to the previous steel structure, its implementation required a significant change in

terms of joining processes for the BIW assembly. A new joining method based on the combination of SPR and adhesive bounding was adopted. Nowadays, this technology represents the main joining process employed by JLR to assemble its aluminium BIW.

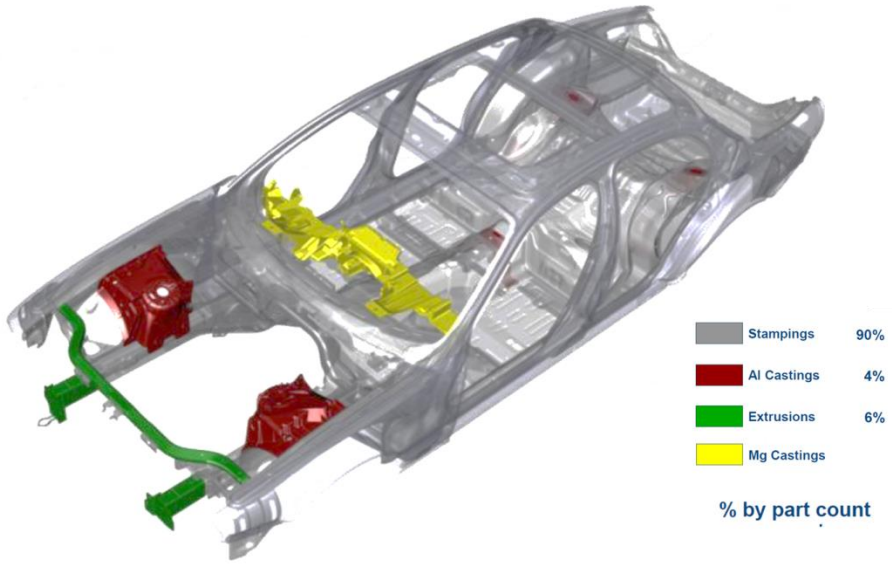

Figure 2: Body in white structure of the Jaguar XJ (2003)

It is clear that the introduction of lightweight materials in the automotive BIW has triggered the requirement for development of new joining technologies compatible with the new vehicle design. The three fundamental processes that allow the joining of material and structures are welding, adhesive bonding and mechanical joining.

Among the welding technologies, Resistance spot welding (RSW) is certainly the most common joining process used in BIW applications.

Despite this process being well established for steel, some issues have been found in welding of aluminium BIW. These issues are related to the experimental and chemical properties of aluminium alloys. One is the chemical reaction of aluminium with oxygen in atmosphere. As a result, the formation of an oxide layer, Al_2O_3, takes place on the metal surface. The latter protects the metal from corrosion but, due to its higher melting temperature compared to the bulk metal, the removal of this film (Han *et al.*, 2010) or regular electrode polishing are needed to allow weld formation to take place (Boomer *et al.*, 2003). Moreover, due to the experimental properties of aluminium alloys such as low electrical and thermal resistivity, higher welding current and electrode force are needed in comparison with steel. Therefore,

the welding current required to spot weld aluminium alloys is about two times greater than steel. Moreover, the electrode life for aluminium alloy spot welding is 2.5 to 5 times lower compared with the electrode life for the spot-welding of mild steel (Ambroziak and Korzeniowski, 2010). Although several researchers have shown that the spot welding of aluminium alloys can guarantee good joint performance, the different requirements on current and electrode life make the process used for steel spot welding, unlikely to be used for aluminium spot welding. Therefore, the application of aluminium spot welding in a large scale vehicle production is still a challenge.

Adhesive bonding (AB) is a joining technology based on the application of adhesive at the interface of the materials to be joined. The main advantages of adhesive bonding are: the more uniform stress distribution, the possibility to gain a lighter structure due to the elimination of mechanical fasteners such as rivets and the prevention of electrochemical corrosion in joint between dissimilar metals (Michalos *et al.,* 2010). The main applications of adhesive bonding in automotive industry concern the non-structural parts, however its application to sheet components for load-bearing parts is now increasing (Davies, 2012b) (Campbell, 2006). For instance, adhesive bonding can be used in combination with resistance spot welding or self-piercing riveting. A hybrid joint of adhesive bonding and RSW or SPR allows a sealed connection, the ability to damp noise and vibrations and a good fatigue resistance (Michalos *et al.,* 2010), (Di Franco *et al.,* 2013). Despite AB offering advantages in the form of hybrid joint, its application as a stand-alone process is still not possible, as in many cases, changing to adhesive would also require substantial change of the bill of the process. Moreover, the long-term durability of the adhesives is still not fully understood (Meschut *et al.,* 2014).

Due to the difficulties in welding aluminium alloys and mixed metal joints and limitation of AB as stand-alone process, mechanical joining has been the key technology to join lightweight materials in automotive BIW.

2.2 Mechanical joining

The use of mechanical joining technologies in automotive BIW has increased over the last decades due the possibility of joining aluminium alloys and mixed metals with different surface coatings. Indeed, mechanical joining only involves mechanical forces that arise from interlocking between the panels. Mechanical joining technologies like SPR and clinching are well established in many automotive production lines. Unlike conventional riveting systems like blind riveting, these technologies offer the advantage of no pre-drilled hole requirement which enables saving time and hole misalignment issues. Figure 3 shows the steps of a clinching process and emphasizes that, differently from the SPR, the technique is only based on a punch to form the material into a die without use of rivets.

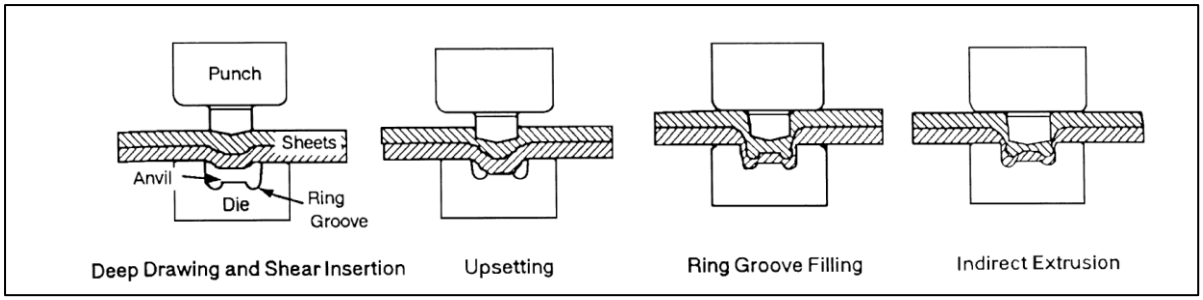

Figure 3: Spot clinching process (Barnes and Pashby, 2000b)

Despite clinching and SPR offering the capability of being applied to dissimilar materials, the main disadvantages of the two processes are the double-sided access and the quite large setting force which requires for a stiff C-Frame structure capable of withstanding the riveting force (Barnes and Pashby, 2000b).

2.2.1 Self-pierce riveting

SPR is “allegedly” a cold joining method that enables the joining of two or more materials by creating a mechanical interlock between the rivet and the substrate materials. As shown in Figure 4, the process is characterized by four successive steps: (I) clamping, (II) piercing, (III) flaring and (IV) releasing. Clamping is the first step where the rivet comes into contact

with the top sheet; the rivet then breaks through the top sheet and flares into the bottom sheet. Finally, the punch is released when reaching the value of the force or displacement given as an input. Figure 5 shows these four steps in relation to a typical force-displacement curve measured during the riveting process (Hou *et al*., 2004). This curve is usually used for process monitoring, since its shape is a characteristic of each SPR joint (He *et al*., 2006). King (1997) conducted a detailed study on the quality monitoring of the SPR process with reference to the behaviour of the force-displacement curve. It was observed that the shape of the curve is affected by rivet geometry, substrate material grade and thickness and die geometry (King, 1995).

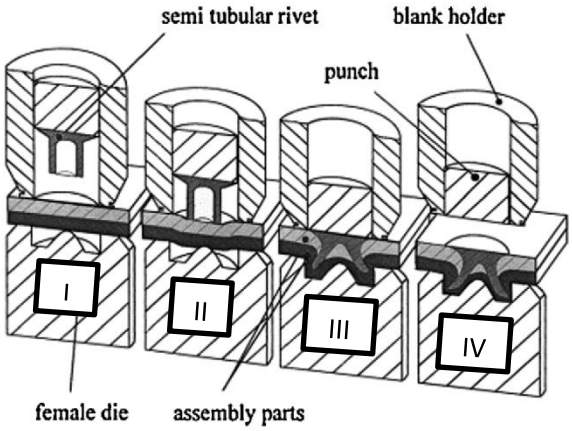

Figure 4: Schematic representation of the SPR process (Voelkner, 2000)

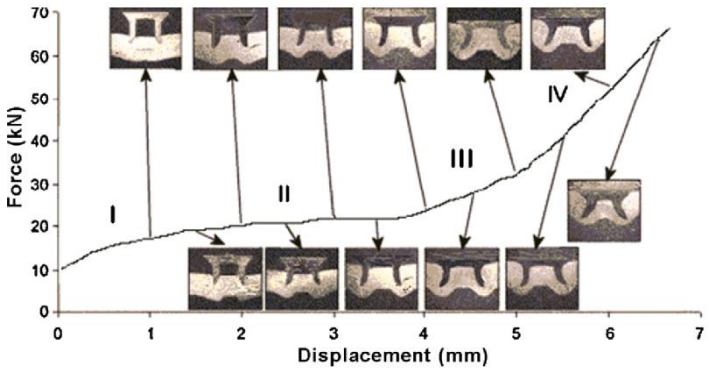

Figure 5: A typical force-displacement curve for a SPR process (Hou *et al.*, 2004)

The increased application of SPR has been justified by several advantages including: no predrilled hole requirements, the possibility of joining different metals with dissimilar surface coatings, the capability of joining various stacks with two or three layers of materials,

comparable cycle-time with spot welding, and no fume emission which makes the process environmentally friendly (Chrysanthou, 2014). Several researchers have discussed the behaviour of a SPR joint under fatigue and quasi-static loading. SPR showed improved fatigue life (Booth, 2000), and lap-shear strength in comparison to RSW (Han *et al*., 2009). However, in order to achieve the optimum joint performance, detailed investigation of the process parameters like rivet length, die design and rivet surface coating are required. Moreover, it was found that the presence of adhesive could provide significant increase in joint strength and energy absorption under the lap-shear condition (Stephens, 2014).
The comparable mechanical properties with RSW and the several advantages offered, have made the SPR process one of the main technologies to join aluminium and mixed metal BIW structures.

Audi was the first automotive manufacturer employing SPR as a joining process with its aluminium space frame technology in 1993. The Jaguar XJ (2004) used 3118 rivets in a monocoque vehicle where it was estimated that the overall weight of rivets was about 3Kg and the cost of each rivet is roughly £ 2 cents which gives a total cost of $100 per vehicle (Mortimer, 2001). Volvo utilized the SPR for its FH12 truck, where 42 rivets per cab were used to join high strength steel sheets (He *et al*., 2006). The recent application of SPR into the Ford F150 truck represents the first wide-scale application of SPR in a high volume production which involves the assembly of 60 units per hour (Weber, 2015).
Although, the application of SPR can lead to performance benefits in comparison to the conventional RSW, its application might be more critical from the economic perspective. A cost comparison between self-piercing riveting, resistance spot welding and friction stir spot (FSW) welding for high volume aluminium BIW was undertaken by (Briskham *et al.,* 2006). The study showed that, although, SPR would require lower electricity costs, its consumable costs (rivets) would be significantly higher.

Despite the recent developments in the SPR process, further improvements are required to enable its application on new emerging materials such as high strength steel, aluminium castings and composite materials. Moreover, the inability of changing rivet and die combinations during the process and the lack of non-destructive testing techniques present a serious constraint for a smooth implementation of the process in a high volume production environment. Therefore a simulation technique capable of simulating the process and to predict the joint characteristics is required.

2.3 Numerical simulation of the SPR process

Many researchers have investigated the simulation of the SPR process using different commercial finite element packages. A detailed review of the FE models developed for simulation of the SPR process was provided by (He, *et al.*, 2012).

Porcaro *et al.* (2006) developed a 2D axisymmetric simulation for a single rivet specimen where the variables of the model were thickness and material properties of the top and bottom substrate materials (Figure 6). An r-adaptivity method was implemented to deal with the large plastic deformation which occurred during the SPR process. Bouchard *et al.* (2008) used Forge 2005 finite element software to simulate the mechanical fields such as damage, residual stresses and strains occurring during the SPR process. Hoang *et al.* (2011) used a 3D model to simulate the joint strength by taking into account the effect of straining occurring from the riveting process and the increase in work-hardening due to natural ageing of the substrate materials AA6063 – W.

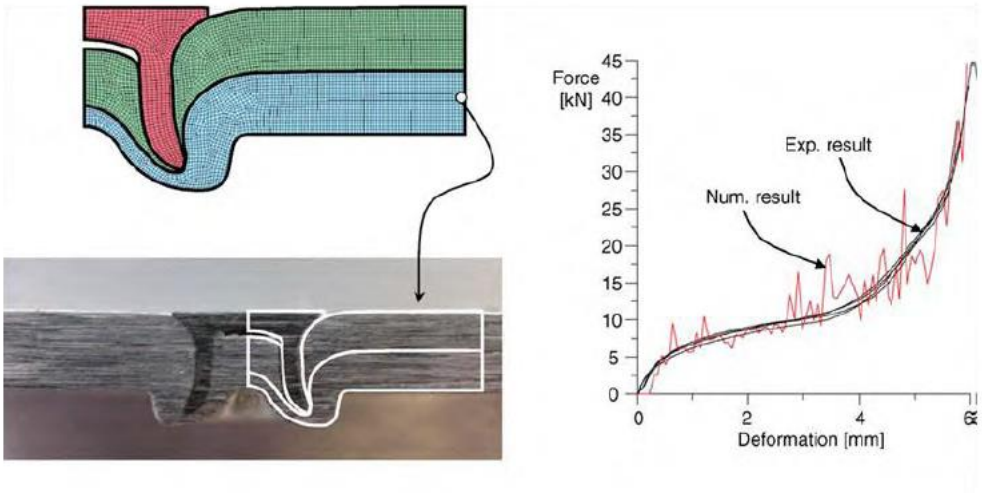

Figure 6: Comparison between numerical and experimental cross-section and force vs displacement curve (Porcaro *et al.*, 2006)

Hoang *et al.* (2010) provided a numerical analysis using aluminium SPR rivets. Successful joints were obtained by adjusting the strength of the aluminium rivet through heat treatment and by optimizing the die shape. Mori *et al.* (2006) used the LS-Dyna finite element code to simulate the joining of ultra-high strength steel to aluminium alloy. Defects like rivet compression, rivet fracture and rivet bending were avoided by optimizing the die geometry.

Mucha (2011) used Marc finite element software to analyse the effect of different variables on SPR quality parameters. The variables under investigation were: rivet proof strength, die impression profile and friction coefficients. The results showed that rivet strength and die profile had significant influence on the setting force and rivet spreading whilst marginal variation in setting force was observed by increasing of friction coefficients. Hoang *et al.* (2013) studied the effect of the friction coefficients on the strain localization at critical area of a AA7278 – T6 rivet. The author found that the friction coefficient between rivet and substrate materials had a significant effect on the compression of the rivet leg. Indeed, by increasing of friction coefficient, higher compression of the rivet leg was obtained. Moreover, it was observed that friction coefficients between 0.6 and 0.8 lead to strain localization along two perpendicular directions which indicated the potential cause of shear fracture (Figure 7).

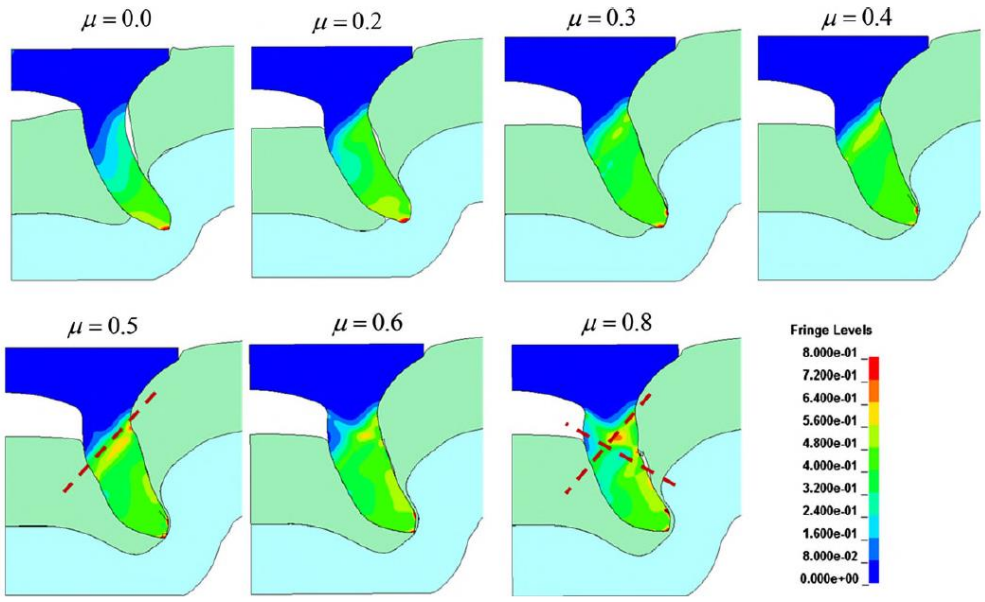

Figure 7: Effect of different friction coefficients on the equivalent plastic strain of aluminum rivet. (The dashed red line indicate the area where shear fracture might occur) (Hoang *et al.*, 2013)

The piercing process has often been simulated with a geometric failure criterion in which element removal takes place when the local thickness of the pierced sheet reaches a user defined critical value. An alternative method was provided by Casalino *et al.* (2008) in which, the failure of the upper sheet was modelled by imposing an effective plastic strain at fracture combined with the erosive Kill-element technique. However, in order to reduce the volume loss due to the erosion technique, finer mesh and higher effective plastic strain at the fracture were required (Figure 8).

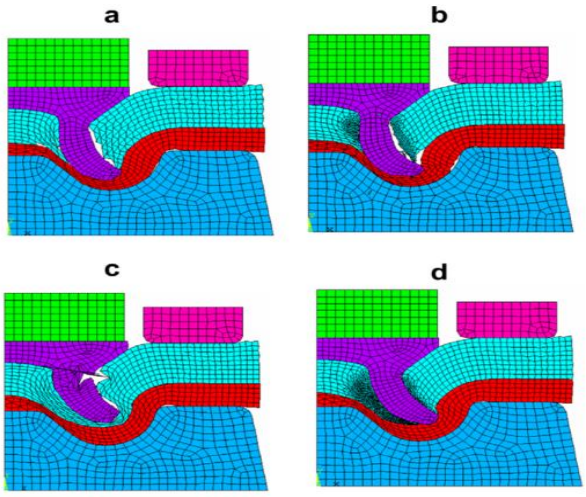

Figure 8: Final configurations for a) coarser mesh (minimum element size=0.2mm) and lower failure parameter ($\varepsilon_p = 1.1$); b) finer mesh (minimum element size=0.066mm) and lower ε_p; c) coarser mesh and higher ε_p (1.5); d) finer mesh and higher ε_p. (Casalino *et al.*, 2008)

Fayolle (2006) used the Lemaitre coupled damage model to simulate the piercing of the top sheet. In this model, the damage evolution during the rivet insertion influences the mechanical properties of the material and element removal takes place when the damage parameter reaches a critical value. However, its application is mesh sensitive and requires a very fine mesh for correct simulation of the element deletion.

While previous studies provided some insight into simulation of the SPR process, attention was mainly focussed on the structural behaviour of the joint or optimisation of the rivet and die geometry. None of the previous research has developed a simulation tool capable of predicting joint characteristics for complex industrial applications. In addition, the development of detailed boundary conditions and material models representative of the real process were often underestimated. For instance, as discovered in this study, accounting for the effect of thermal softening of the substrate materials due to plastic deformation and friction contacts is key for accurate simulation of the SPR process. Additionally, models have often only been validated against a small number of joint combinations and the importance of model robustness and CPU time have been neglected.

3. Research methodology

The ultimate objective of this research is to develop a simulation technique which requires short CPU, accuracy and robustness to enable applications in a manufacturing environment. The structure of this research methodology is characterized by four main pillars as indicated in Figure 9:

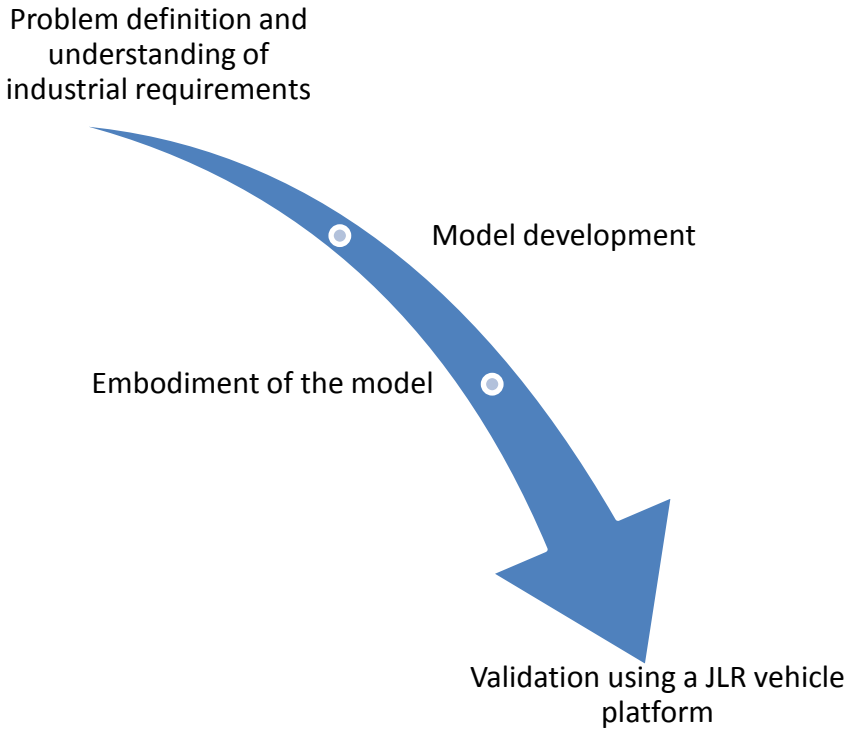

Figure 9: Research pillars

1. Problem definition and understanding of industrial requirements:

The common procedure used in the automotive industry to assess the feasibility of a SPR joint is based on experimental testing of coupon materials and subsequently cross-sectioning for measuring of the joint characteristics. A schematic of a SPR cross section is shown in Figure 10. In general, three geometric parameters are measured to assess joint feasibility:

- Head height – this measures the depth to which the rivet is inserted into the material. In general, during coupon testing the setting parameters of the SPR gun (e.g. velocity/

end position) are chosen in order to achieve a rivet head sitting flush with the surface of the top layer.

- Interlock – this measures how much the rivet legs spread into the bottom layer of the joint
- Remaining thickness (T_{min}) – this measures the thinnest gauge of the bottom layer achieved after the riveting process

Other factors that need to be checked are rivet cracking / buckling, cracking of the substrate materials and gaps between the panels. If a riveted joint has achieved certain characteristics according to the JLR standards then the joint can satisfy the requirement for joint strength, fatigue and corrosion behaviour.

As mentioned previously, the method of coupon testing represents a serious constraint to the business, as for any new vehicle platform development thousands of coupon tests are required to establish the feasible rivet/die combination within each cell of a BIW assembly facility. Therefore, if a robust simulation tool is available to predict rivetability, then a significant amount of time spent on experimental testing can be saved.

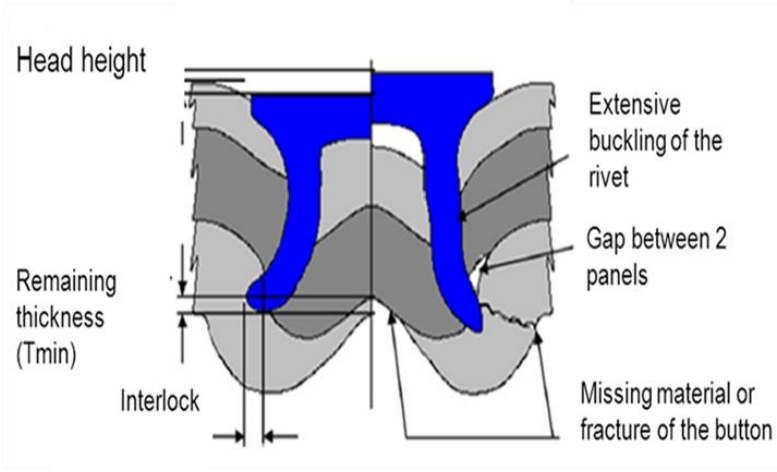

Figure 10: Characteristics of a SPR joint cross-section

2. Model development:

The development of the finite element model is characterized by two main phases. The first phase involves the development of the input parameters such as boundary conditions, mesh parameters and friction coefficients. The model was developed using a variety of different rivet and die CAD models representative of the real geometries while the kinematics of the tooling were simulated according to the kinematics of the process. Mesh parameters and friction coefficients were determined from inverse analysis and their values were kept constant for all the simulations.

The second phase involves the development of the material models which reflects the material response under the specific process conditions. In this context, as SPR involves large plastic deformations which affects both rivet and substrate materials, the simulation of this process through FEA requires a non-linear model in which the mechanical behaviour of the materials during plastic deformation can be considered. In this study, the material model for the substrate material has been developed by taking into account both strain hardening and thermal-softening. Therefore, uniaxial tensile tests were designed and performed under different temperature regimes. The experimental procedure is described in (Carandente *et al.*, 2016). The machine used for the tensile tests was a MTS_322 hydraulic press while the tensile samples were made according to the ISO 10130 standard. The heating was applied through an electromagnetic inductor in contact with the gauge length of the specimen (Figure 11a). The heating process was controlled through K-type thermocouples that were spot welded to the heated region of the samples.

Since SPR exposes the material to large plastic deformation, the development of a robust material model requires the study of the material properties at very large strain values. It is known that a conventional true stress vs true strain curve can only be applied with good accuracy until the moment of necking as the reduction of sample cross section area is not taken into account. In this study, the deformation of the samples was measured using a non-contact optical deformation measuring system based on digital image correlation (DIC). The images captured by the camera were analysed with the Aramis^{TM} from GOM in order to calculate the evolution of the true strain during testing. Finally, the area at fracture for each testing conditions were measured by means of SEM in order to calculate the true strain at fracture.

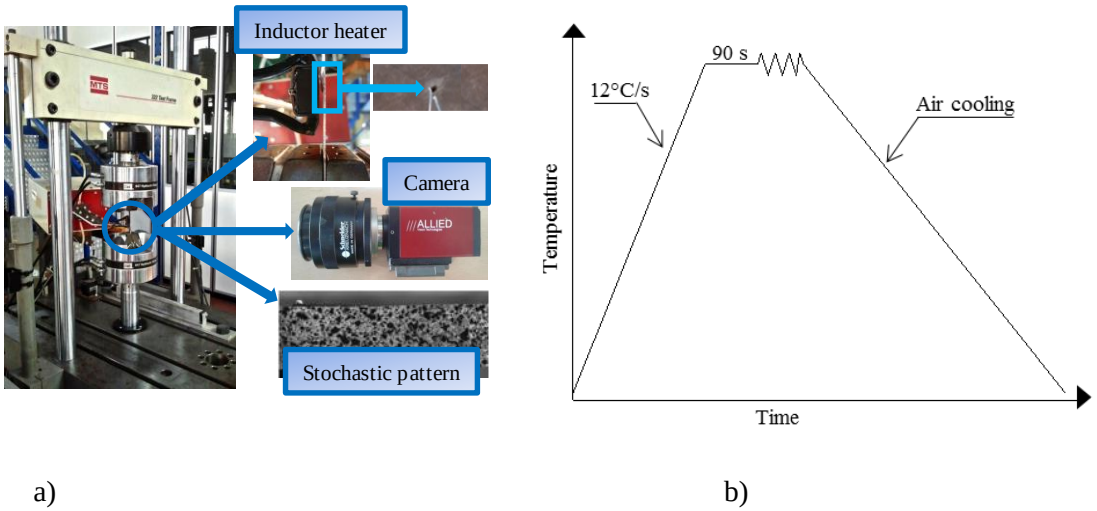

Figure 11. a) Experimental setup. b) Thermo-mechanical cycle of the tensile tests at high temperature

The benefit of using the DIC system is shown in Figure 12 where the comparison between true stress vs true strain curves obtained respectively with the conventional strain measurement based on cross-head displacement and Aramis system was provided. It can be noticed that the use of Aramis allowed detection of the true stress vs strain curves up to 0.4 of strain whilst the conventional strain measurement allowed detecting about half of the strain.

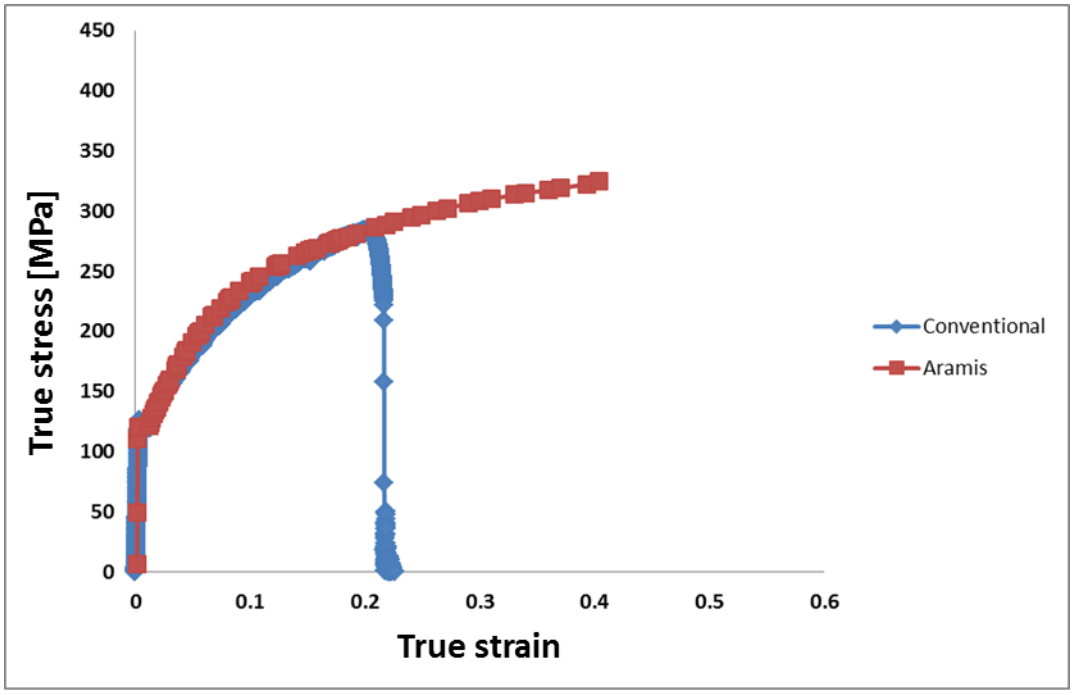

Figure 12. Comparison between true stress and true strain curves of AA5754 at ambient temperature and 0.01 s^{-1}obtained with conventional cross-head displacement and Aramis system

Material data for the rivets was provided by the SPR manufacturer. Three rivets made of boron steel and having different hardness levels: H_0, H_2, and H_4 were used in this study. The proof strength at 0.2% of strain (σ_y) of the three rivets are listed in Table 2. The rivets used in this study are covered by a zinc coating to prevent corrosion issues between the rivet (boron steel) and substrate materials (aluminium alloy). The main purpose of the coating is to inhibit corrosion issues but it can also act as lubricant by lowering the friction generated during the rivet insertion.

Table 2. Proof strength of rivets

Rivet n.	σ_y (MPa)
H_0	900
H_2	1350
H_4	1550

The thermal-softening of the rivet was not considered as the temperature experienced would only have a subtle effect on boron steel.

3. Embodiment of the model:

This study showed that a thermo-mechanical coupling finite element analysis, which allows consideration of the dependency of the material properties upon the temperature, leads to a more precise prediction of the mechanical behaviour of the materials. The latter was proved by the better correlation between the numerical and experimental cross-sections but also via experimental measurement of the temperature generated during the SPR process using infrared analysis. The model was validated for both 5xxx and 6xxx series aluminium alloys. Moreover, the effect of natural ageing of the AC600 T4 was also considered by developing material models for different periods of ageing.

4. Validation using JLR vehicle platform:

Validation of the accuracy and robustness of the developed simulation technique was provided using SPR joints representative of a JLR vehicle platform. More than 1000 joints with over 100 joint configurations made of 5xxx and 6xxx series alloys have been simulated and compared with the results from the experimental tests to assess accuracy and robustness of the technique.

4. Development of the Finite element models

The Finite Element Method (FEM) is a computational tool used to simulate mechanics, physics and engineering problems. The use of finite element analysis (FEA) has grown substantially over the last few years enabling major control of processes in both economic and engineering aspects. Nowadays, this method can be used in a manufacturing environment to lower tooling and equipment costs, to reduce material wastage and to allow the performance prediction of processes (Chenot and Massoni, 2006).
In this study, Simufact.forming^{TM} which uses a Marc non-linear solver was used to develop the FE analysis for numerical simulation of the SPR process. This section investigates the development of boundary conditions, mesh features and friction coefficients.

4.1 Boundary conditions

As for any simulations, the boundary conditions are crucial and need to be defined. In this context, the loads applied and the kinematics of all the tooling involved in the SPR process need to be developed. The first step concerns the development of a CAD model able to reproduce the geometry and shape of the SPR tooling. Figure 13a shows the geometry of the real SPR C-frame while Figure 13b shows the virtual gun developed for the FE simulation. In the latter, the entire C-frame shape has been replaced by three main rigid bodies which are the punch, blank holder and die. Therefore, the only deformable bodies are the rivets and substrate materials. The second step concerns the identification of the loads and motions applied by the system. In general, depending on how the rivet is inserted, SPR systems are classified in two categories: “punching” or “pushing”. In a punching system, the punch is accelerated to a certain speed defined by the user and hits the rivet with an impact; while in a pushing system, a gradually increasing force is applied to push the rivet into the workpiece until it reaches a user defined displacement (Li *et al.*, 2015).

The focus of this research was on the simulation of a pushing system. In this case, the process is characterized by two main steps, first the substrate materials are clamped between the die and blank-holder and then the punch pushes the rivet into the sheets until the rivet is sitting flush with the surface.

The kinematic of the punch was simulated using constant velocity of 100mm/s while the clamping force applied by the blank holder was modelled through a compressed spring with a force of 5 kN which is representative of a typical SPR gun (Figure 14).

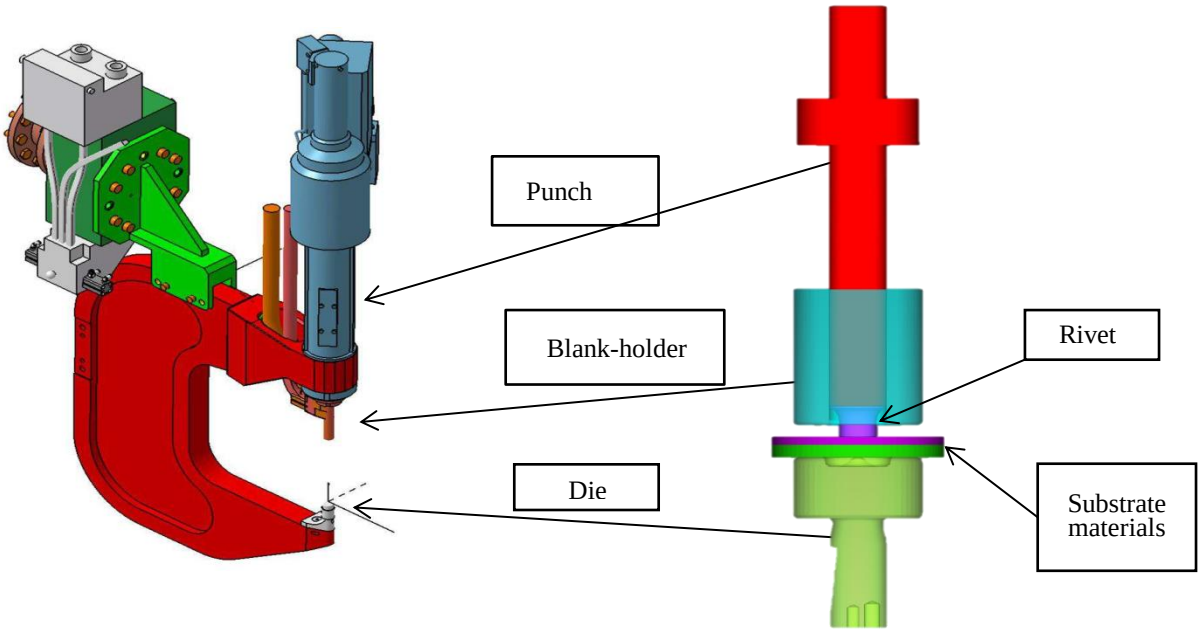

Figure 13. a) Real C-frame b) Virtual C-frame

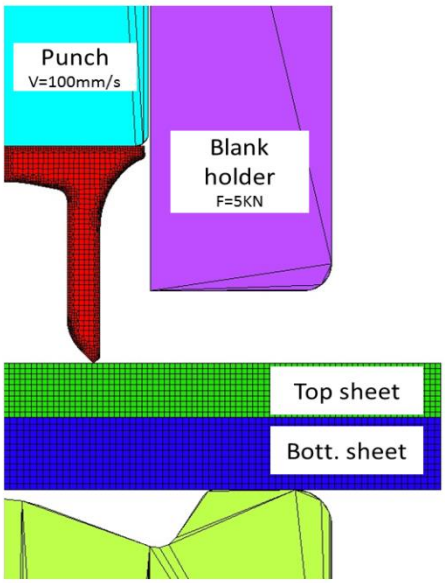

Figure 14. Schematic view of the axisymmetric model including the external loads applied

4.2 Mesh parameters

The mesh type and sizes represent an important aspect of the FEM as they affect both the CPU time and accuracy of the simulation results. The element type used for the numerical modelling was a 4-noded solid element (type 10) which is used for axisymmetric applications (Marc, 2013a).

The definition of the mesh sizes was carried out through inverse analysis in order to assess the optimum mesh dimensions which allow the lowest CPU time without affecting the accuracy of the results. Table 3 lists four different mesh sizes used for comparisons.

Table 3. Mesh sizes used for comparisons

Model No	Rivet [mm]	Top sheet [mm]	Bottom sheet [mm]	CPU time
1	0.05x0.05	0.1x0.1	0.1x0.1	37 min
2	0.05x0.05	0.1x0.1	0.15x0.15	31 min
3	0.07x0.07	0.15x0.15	0.2x0.2	14 min
4	0.07x0.07	0.3x0.3	0.3x0.3	6 min

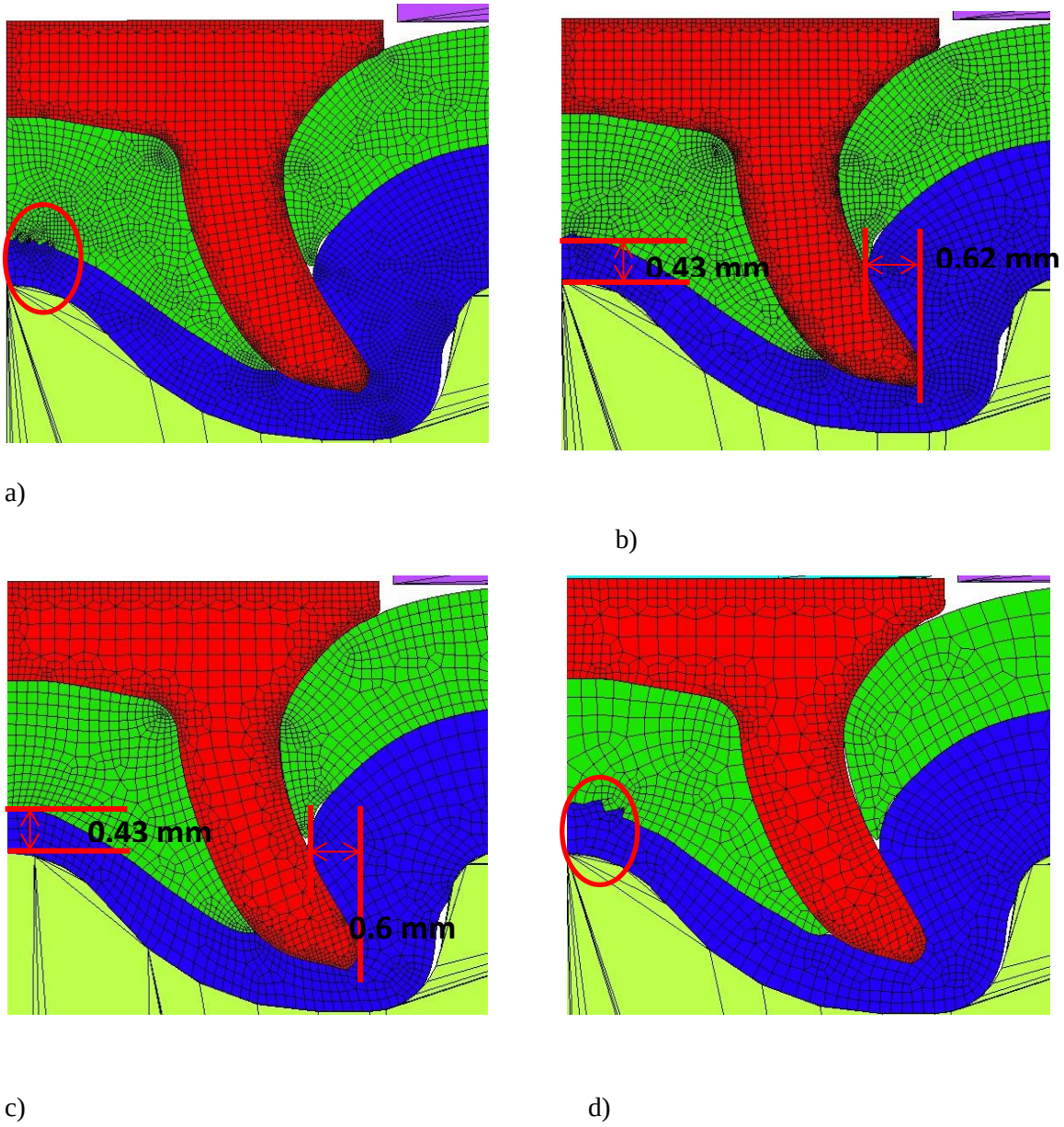

Figure 15. Comparisons of different mesh sizes: a) Model 1, b) Models 2, c) Model 3, d) Model 4. Model 1 (a) and Model 4 (d) show interpenetration (circled) between elements of top and bottom sheets

Figure 15a and 15d show that models 1 and 4, which represent respectively the case of finer and coarser mesh, reported element interpenetration (circled) between the top and bottom sheet meshes. In these cases meshes of the same size were applied to the upper and lower sheets. To avoid element interpenetration, the edge length of the rivet mesh was set marginally finer compared to that of the top sheet. Similarly, between the top and bottom sheet (model 2 and 3). This procedure is typical amongst finite element programmes. In

Marc, the use of direct contact methods is possible to avoid penetration between bodies. This method is based on the definition of touching-touched bodies which allows checking only for nodes of the touching body and reduces the number of times that boundary nodes are used in the creation of contact equations (Marc, 2013b). In this case, the contact directions were assigned in order to treat the rivet as the touching body with respect to the top and bottom sheets while the top sheet was treated as the touching body with respect to the bottom sheet. In general finer mesh is used for the touching body and coarser mesh for touched body.

As shown by the cross-section of model 2 and 3 (Figure 15b and 15c) the application of this method successfully avoided element interpenetration. Moreover, as the joint characteristics and force vs displacement curves (Figure 16) showed similar results in both the models, the mesh sizes used in this study were selected according to model 3 as it achieved a CPU time of 14 minutes in comparison to the 31 minutes required for model 2.

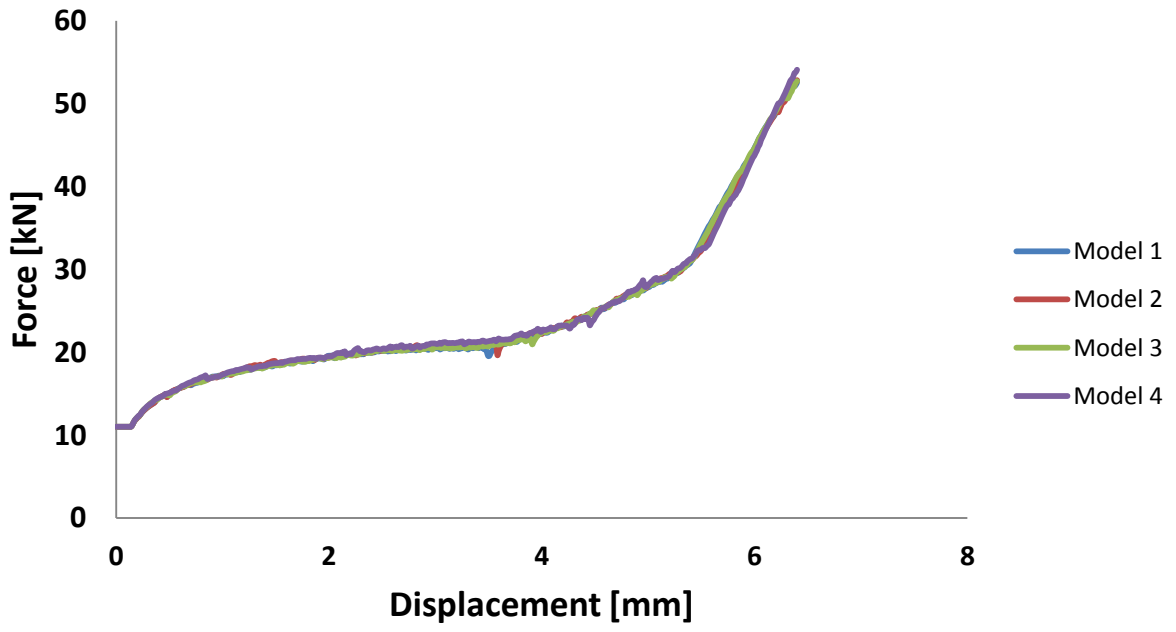

Figure 16. Comparison of force vs displacement curves obtained with models 1, 2, 3 and 4

Table 4 lists the mesh parameters used by previous researchers on SPR simulation. The sizes of the mesh used in this study are comparable with the literature, however, in this study different mesh sizes were adopted for each deformable body, whilst other authors tend to use the same mesh size for all the bodies.

Table 4: List of mesh parameters used in the literature for SPR simulation

Author	*Mesh parameters*
Bouchard *et al.* (2008)	$Not\ defined\ in\ the\ paper$
Porcaro *et al.* (2006)	$Size$: 0.1 x 0.1 $for\ rivets\ and\ substrate\ materials$
Mori *et al.* (2006)	$Not\ defined\ in\ the\ paper$
Casalino *et al.* (2008)	$Size$: 0.066x 0.066 $for\ rivets\ and\ substrate\ materials$
Mucha (2011)	$Size$: 0.15x 0.15 $for\ rivets\ and\ substrate\ materials$

In order to deal with the large deformation of the mesh elements, automatic mesh refinements were used. As shown in Figure 17, two re-meshing techniques available in Simufact.forming™ were implemented: the Advancing front quad method that was used to re-mesh the elements of the substrate materials and the Quadtree method which was used to re-mesh the elements of the rivet as it allows creation of a finer mesh on the boundary.

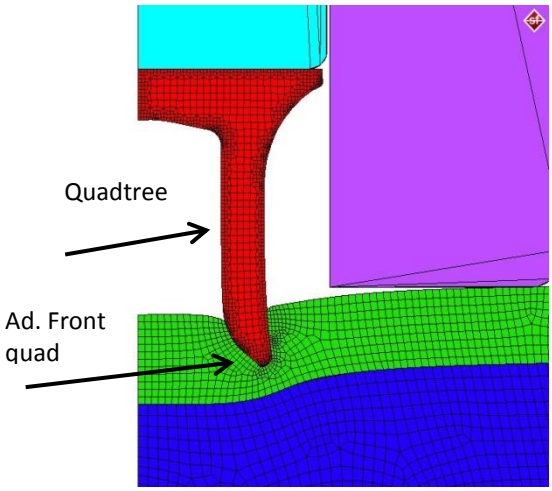

Figure 17. Mesh refinement used for the numerical simulation of the SPR process

Finally, in order to allow the splitting of the top sheet during the rivet insertion, a geometric failure criterion was applied. This method is based on an erosion technique which allows elements of the mesh to be deleted when a user defined thickness value is reached. The calibration of the user defined minimum element thickness was performed from inverse analysis by comparing the force vs displacement curves of numerical and experimental tests. The following three values were used for comparison: a) $T_{removal}$ = 0.02mm, b) $T_{removal}$ = 0.1mm and c) $T_{removal}$ = 0.2mm. Figure 18 shows the rivet insertion at time steps before and after the erosion technique takes place for the three values of $T_{removal}$.

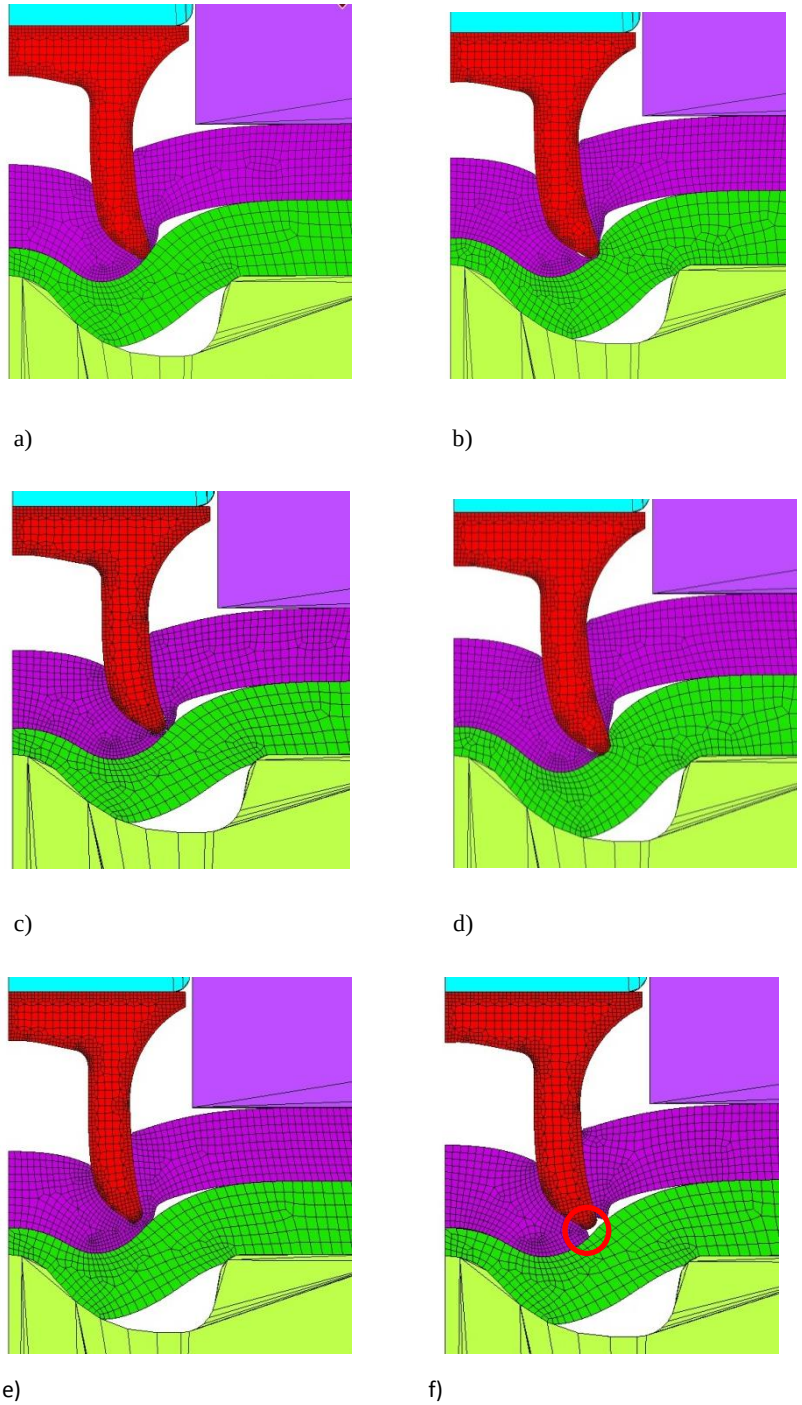

Figure 18. Rivet insertion at time steps before and after the erosion technique takes place: a) $T_{removal}$ = 0.02mm before erosion b) $T_{removal}$ = 0.02mm after erosion c) $T_{removal}$ = 0.1mm before erosion d) $T_{removal}$ = 0.1mm after erosion e) $T_{removal}$ = 0.2mm before erosion f) $T_{removal}$ = 0.2mm after erosion.

Figure 19 shows the comparisons between the experimental and numerical force vs displacement curves for the three user defined values. It can be noticed that for $T_{removal}$ = 0.1mm and $T_{removal}$ = 0.2mm, a drop of force, as a consequence of the elements removal, appears in the graph. This is most pronounced when using $T_{removal}$ = 0.2 where, as shown in

Figure 18f at the time step after the erosion technique has been applied, there are no elements touching the rivet tip (circled). The user defined thickness value used for all the simulations discussed in this study was $T_{removal}$ = 0.02mm as it achieved the best comparison with the experimental force vs displacement curve, as shown in Figure 19.

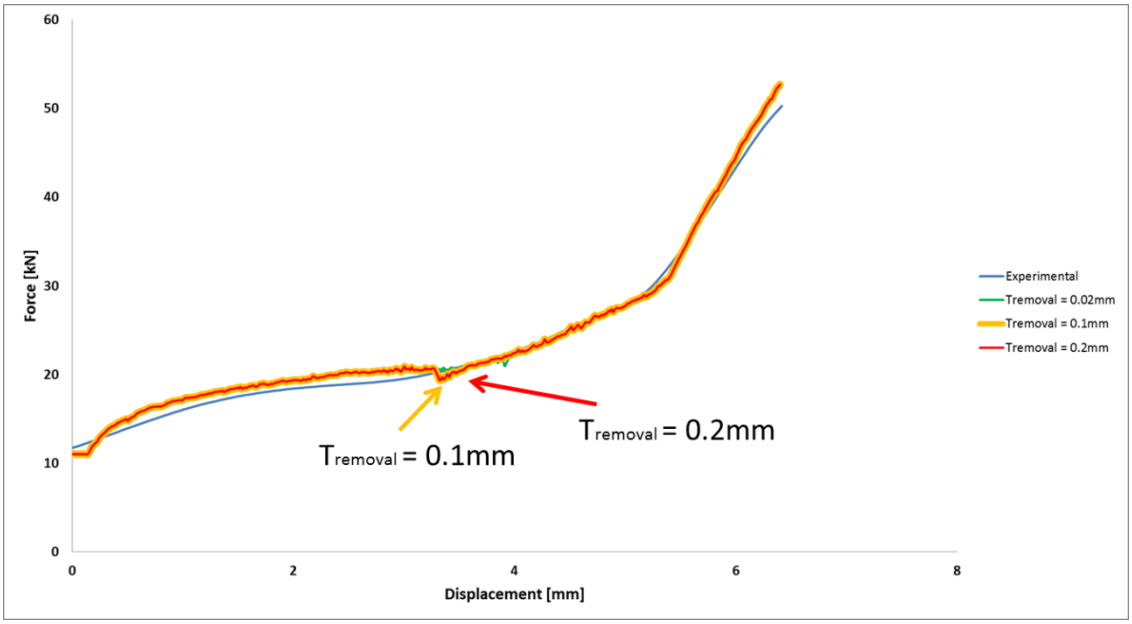

Figure 19. Comparisons of force vs displacement curves at $T_{removal}$ equal to 002mm, 0.1mm and 0.2mm

4.3 Coefficient of fiction

Another important aspect to take into account when modelling the SPR process is the friction generated between the contact bodies. There are several interfaces where frictional contacts occur: between the punch and rivet, between the substrate materials, between rivet and substrate materials, between top sheet and blank-holder and between bottom sheet and die. However, due to the difficulties in measuring the friction forces at these interfaces by in-situ methods, the coefficients of friction are often determined via inverse methods. Therefore, the coefficients of friction to assign into the FEM represent uncertain factors. As they affect the simulation results, a robust calibration of the friction coefficients is required in order to allow the use of the same values for any rivet / die combinations and stack thickness.

The friction model used in this study is based on the Coulomb law which describes the relationship between the applied normal pressure and friction force through a linear equation:

$$\tau = \mu P \qquad (1)$$

Where τ is the friction shear stress, P is the normal pressure and μ is the coefficient of friction.

The friction coefficients were determined from inverse analysis using one joint as reference and successively validated with a series of different joints. Figure 20 shows the effect of the friction coefficients on the numerical cross-section using two models as reference. In Model 1, the following coefficient of friction were used: μ = 0.09 at the interface between the sheets and between sheets and rivet, μ = 0.15 at the interface between the bottom sheet and die, between top sheet and blank holder and between rivet and punch. In Model 2, a friction coefficient of μ = 0.15 at the interface between the sheets and sheets and rivet, μ = 0.25 at the interface between the bottom sheet and die, between top sheet and blank holder and between rivet and punch. It can be observed that Model 1 provided a better representation of the experimental results (Figure 20a), whilst Model 2 showed lower flaring of the rivet (Figure 20b).

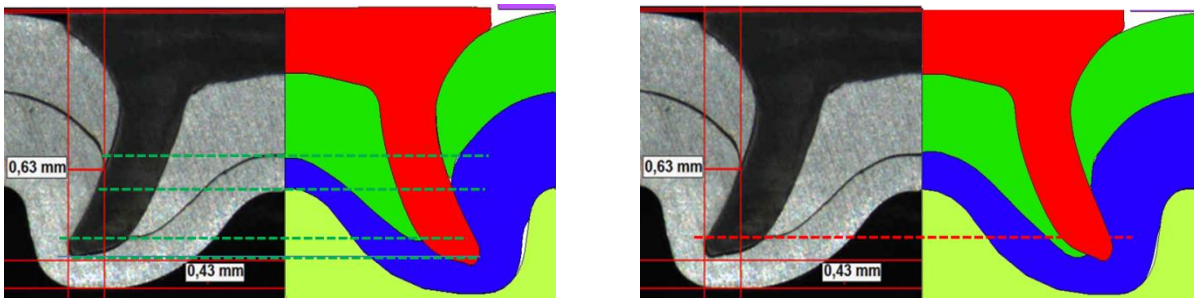

Figure 20. comparison of cross-section geometries. a) model 1 - μ = 0.09 at the interface between the aluminum sheets and μ = 0.15 at the interface between the bottom sheet and die. b) model 2 - μ = 0.15 at the interface between the aluminum sheets and μ = 0.22 a

Figure 21 shows the comparison of the two models in terms of force vs displacement curves. It can be noticed that Model 1 showed better agreement with the experimental curve which indicates the validity of the selected friction coefficients. Therefore, based on these results, the friction coefficients used in the FEM were defined according to Model 1 and were kept constant for all the simulations.

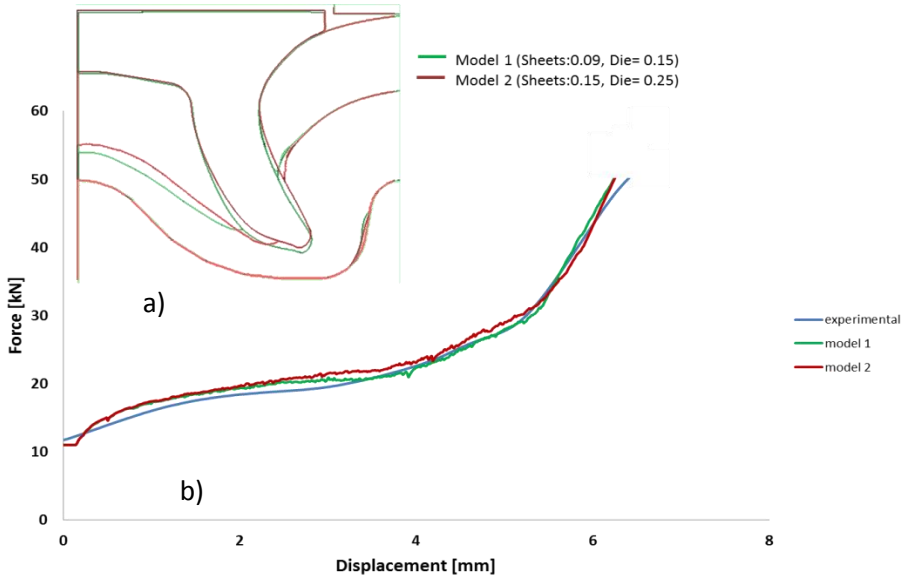

Figure 21. Comparison between model 1 and 2. a) cross-section geometries b) force vs displacement curves

Table 5 lists the friction coefficients used in the literature for SPR simulation. It can be observed that different researchers have used different friction coefficients, however the values fall in the range between 0.1 to 0.3, which is representative of the friction coefficients used in this study.

Table 5: List of mesh parameters used in the literature for SPR simulation

Author	Friction coefficient
Bouchard *et al.* (2008)	$\mu = 0.1$ **same for all the interfaces**
Porcaro *et al.* (2006)	$\mu = 0.15$ **between sheets** $\mu = 0.3$ **between blank holder and top sheet** $\mu = 0.3$ **between die and bottom sheet**
Mori *et al.* (2006)	$\mu = 0.2$ **same for all the interfaces**
Casalino *et al.* (2008)	$\mu = 0.1$ **same for all the interfaces**
Mucha (2011)	$\mu = 0.05$ **same for all the interfaces**

5. Discovery of the thermo-mechanical behaviour for SPR simulation

Adiabatic heating due to localized plastic deformation and frictional contact has been investigated in diverse areas such as ballistic impact, machining and high speed forming processes (Rogers, 1979). The amount of heat generated by plastic deformation was first studied by (Farron and Taylor, 1925) on steel, copper and aluminium. In all the cases, it was found that about 90% of the plastic work was converted into heat while the remaining 10% was stored in the material as internal energy. This is also valid for the dissipation of the friction energy, where according to (Archard, 1959) nearly all the friction energy is dissipated as heat.

The heat generated can either be dissipated to the surroundings or can determine a local temperature rise of the material which can affect its mechanical behaviour. The latter is the case of adiabatic heating where the rate of heat generation is greater than the rate of heat loss (Kapoor, 1998). The effect of softening due to adiabatic heating is widely accepted and often included in simulation of ballistic impact tests (Borvik *et al*., 2001) and friction welding processes (Awang *et al*., 2005).

SPR is essentially a cold forming operation where a rivet is inserted into a material stack in a fraction of second. The process involves highly localized plastic deformation and friction contacts which mainly affect the area surrounding the rivet legs and the area of the bottom layer material filling the die cavity. In these conditions, both plastic deformation and friction contact generate heating. Moreover, as the heat generated in the localised regions has no time to transfer, it leads to adiabatic conditions.

The development of a reliable and accurate numerical model requires a detailed investigation of the boundary conditions that affect the real process. One of the main challenges concerns the development of an accurate material model which reflects the material response under the specific process conditions. Therefore, a thermo-mechanical coupling finite element analysis, which allows consideration of the dependency of the material properties upon the temperature, might lead to a more precise prediction of the mechanical behaviour of the materials.

In this chapter, an experimental procedure to measure the heat generated during the SPR process has been proposed and the effect of thermal-softening has been validated via

numerical analysis. Finally, the effect the of friction coefficient, punch velocity and thermal conductivity on the temperature generated during the process have been investigated.

5.1 Experimental setup for temperature measurement during SPR process

In the SPR process, plastic deformation and friction contact mainly occur in the area between the rivet legs, therefore, the use of thermocouples to measure temperature changes might be ineffective due to the high pressure and large amount of plastic deformation involved which can damage the device. To overcome this issue, infrared thermography (IR) has been used in this study to measure the temperature generated during the SPR process. IR camera devices measure the infrared radiation emitted by an object and converts the energy detected into a temperature value. The thermal-camera used in this study was the Flir IR SC5200 with a resolution of 640x512 pixels.

The surface of the sample exposed to the thermal-camera was covered by a thin layer of matt black paint which has emissivity of 0.9 (Holst, 2000) (Figure 22). Moreover, the area of the SPR gun surrounding the samples to be riveted was also placed inside a box to avoid the influence of the environment.

The temperature generated during the SPR process mainly affects the area surrounding the rivet legs as this area is not visible, the riveting tests were only performed on a half portion in order to expose the other half to the thermo-camera. This was achieved by placing the coupon materials so they only covered half the die as shown in Figure 23a. The thermal-camera could then be oriented to capture images of the visible half of the rivet during the insertion process. Figure 23b shows the cross-section of the area visible to the thermal-camera for the temperature readings.

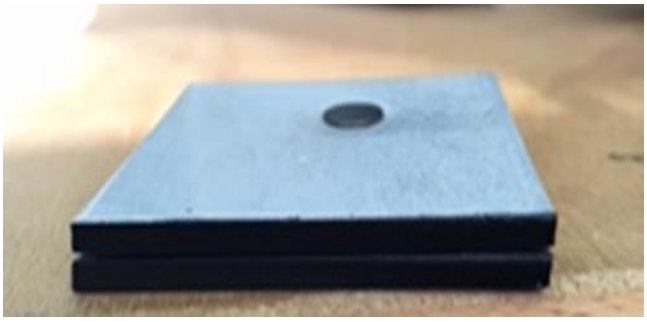

Figure 22: Thin layer of black paint applied on the lateral surface of SPR coupons

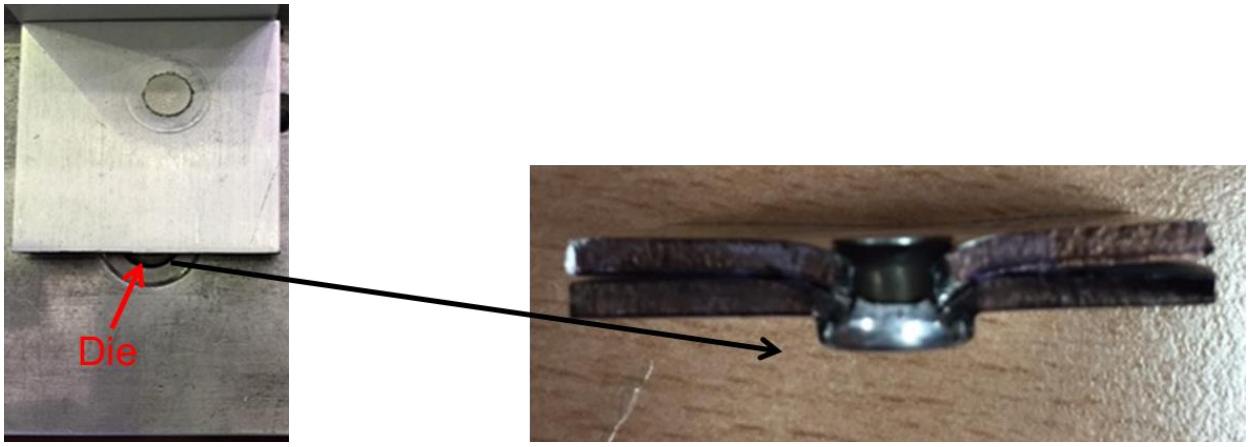

Figure 23: Experimental procedures a) Coupons placed on the top of the die before riveting. b) Coupons with rivet inserted on half section

5.2 Experimental Results

During the experimental tests the following data were recorded:

- Force vs displacement curves given by the SPR gun
- Infrared images acquired at a frame rate of 500 fps (frames per seconds)

The experimental tests were performed using two layers of 2.5mm AC600 T4 aluminium alloy as substrate material and boron steel rivets. As discussed in the previous section, only half of the rivet was inserted into the sheets, therefore not all the plastic deformation and

friction contact involved in a typical SPR process were considered. Figure 24 shows the force vs displacement curves obtained respectively from the full and half riveting process. It can be noticed that the reaction force recorded in the case of the full joint was higher compared to the half joint test with peak forces respectively 50kN and 37 kN. Therefore, it is expected that the temperature measured represents only a fraction of the temperature generated during the full process.

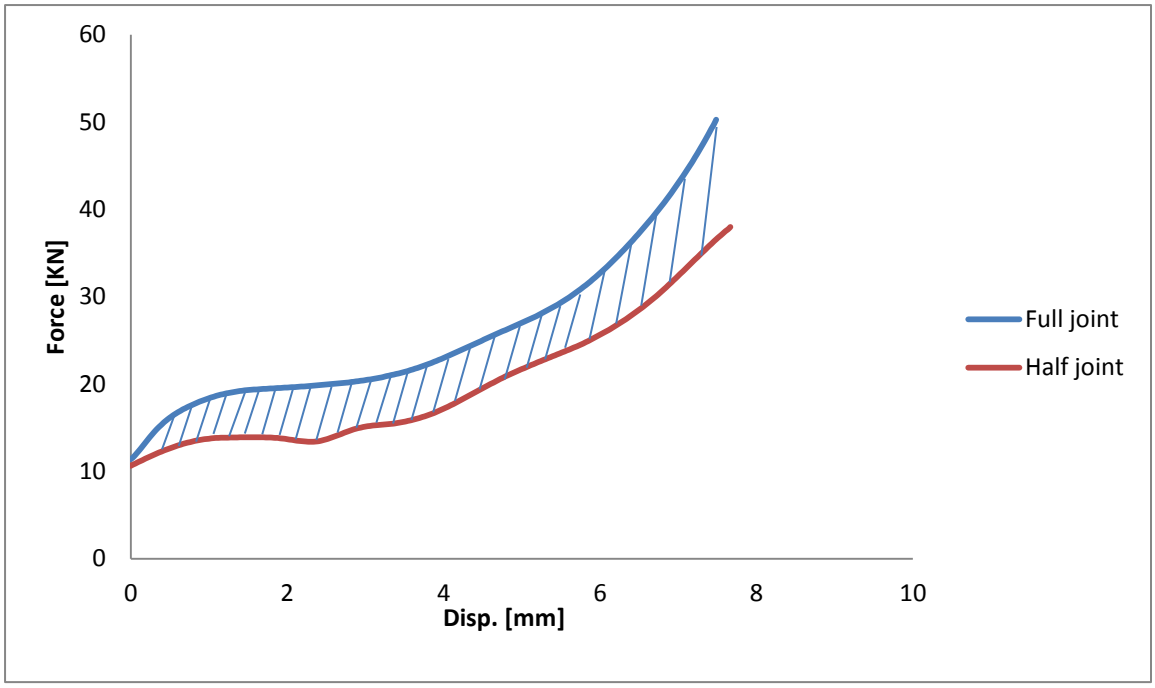

Figure 24: Comparison of force vs displacement curves for full and half joints

The temperature profile measured with the thermal-camera is reported in Figure 25 and shows a peak temperature of about 125 °C. Moreover, Figure 26a shows the images captured by the thermal-camera at the frame number where the peak temperature was recorded. It was observed that the temperature generated during the SPR process mainly affects the area surrounding the tips of the rivet skirt. Figure 26b shows the area of the riveted sample where the peak temperature occurs.

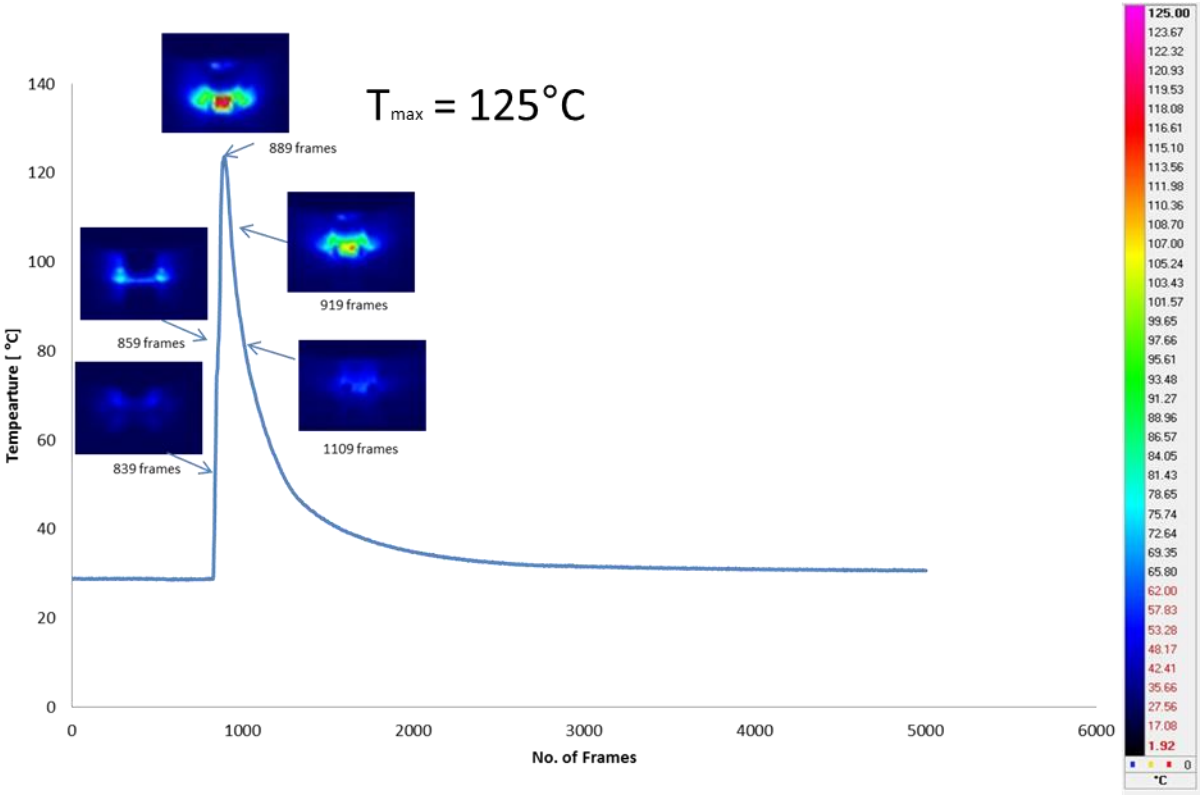

Figure 25: Temperature profile during SPR insertion

a) b)

Figure 26: Area of peak temperature on SPR cross-section. a) IR image, b) experimental sample

5.3 Comparison between experimental and numerical temperature generated during the SPR process

The FE model used to compare the temperature profile of the numerical analysis with the experimental tests was developed using the boundary conditions, mesh features and friction coefficients described in Chapter 4. The model developed in this study is based on 4 main assumptions:

1. Constant coefficient of frictions according to the Coulomb's law
2. Constant Taylor- Quinney coefficient (β)
3. The heat generated during the SPR process is assumed to be adiabatic due to the short time scale
4. High temperature tensile tests performed to study the softening effect of the substrate materials

The joint used for the numerical simulation is the same as the previous section; it consists of two layers of AC600 T4 in 2.5mm gauge. The geometry of the rivet and die used for the simulations are shown in Figure 27. The hardness level of the rivet was H4 and its proof strength is listed in Table 2 whilst the material model of the substrate material (AC600 T4) is discussed in Chapter 7.

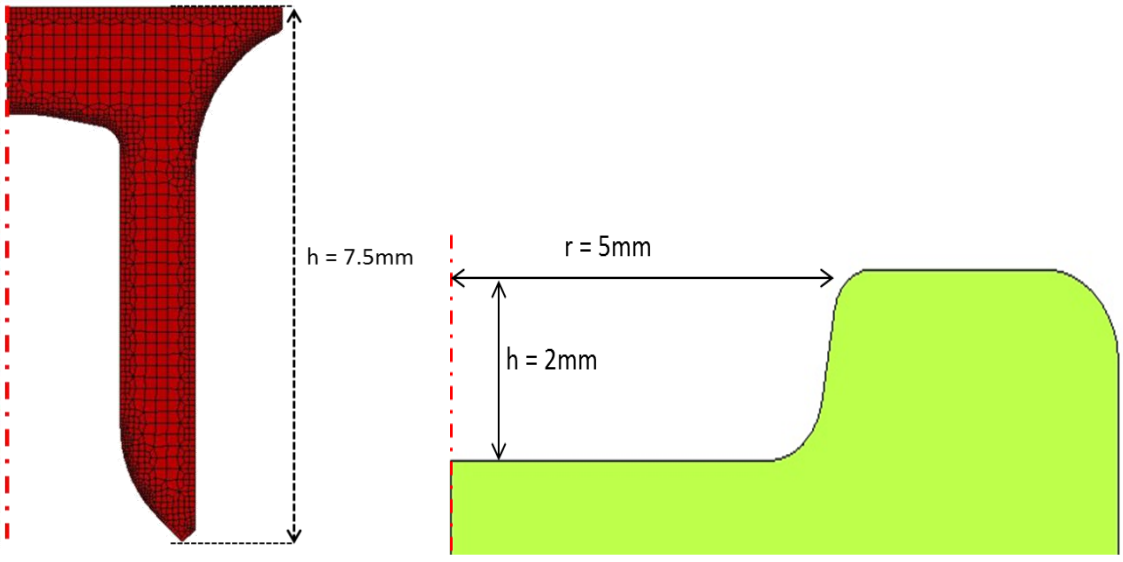

a) b)

Figure 27. Cross-section geometries. a) rivet. b) die

In a thermo-mechanical model three parameters need to be specified: the Taylor- Quinney coefficient (β) which states the amount of plastic energy converted into heat (Perez-Castellanos, 2012), the thermal conductivity and the specific heat capacity.

For this model, the Taylor- Quinney coefficient (β) was set equal to 0.9 (Perez-Castellanos, 2012), while thermal conductivity and specific heat capacity are listed in Table 6.

Table 6: Thermal conductivity and specific heat capacity used in the FE model (Smithells, 1990).

Material	Thermal Conductivity [J/m*s*K]	Specific heat capacity [J/Kg*K]
Boron steel	**32**	**400**
Al-Mg-Si (AC600 T4)	**188**	**900**
Al-Mg (AA5754)	**142**	**900**

The finite element analysis shows that the temperature peak is observed at the tip of the rivet legs where the FEA has recorded a temperature of about 200 °C (Figure 28). The result is in agreement with the experimental temperature if considering that only a half section was taken into account during the experimental tests. The greater temperature at tip of the rivet leg is justified by the higher energy required to deform the rivet which is made of boron steel in comparison to the aluminium substrate materials. The latter indicates that majority of the rivet plastic deformation is localised in the area of the tips. Moreover, the lower thermal conductivity of the rivet (steel) in comparison to the substrate material (aluminium) justifies the temperature gradient within rivet where no heating effect was observed in the area of the rivet head.

Figure 29a and Figure 29b show respectively the temperature profile of the top and bottom sheet. It can be observed that the heat affected zone is mainly localized in the area between the two rivet legs where the top sheet material showed a maximum temperature of about 150 °C. Moreover, it can be observed that the temperature of the bottom layer is around 120 °C which is in agreement with the results of infrared thermography where a peak temperature of 125 °C was measured in proximity of the tip of the rivet leg.

The good agreement between numerical and experimental results is also supported by the

high correlation between the SPR joint characteristic as indicated in Figure 30. A good correlation is also found in terms of the force vs displacement curves where, as shown in Figure 31, a maximum deviation of about 1.5 kN, which corresponds to less than 10% variation, is found between numerical and experimental results.

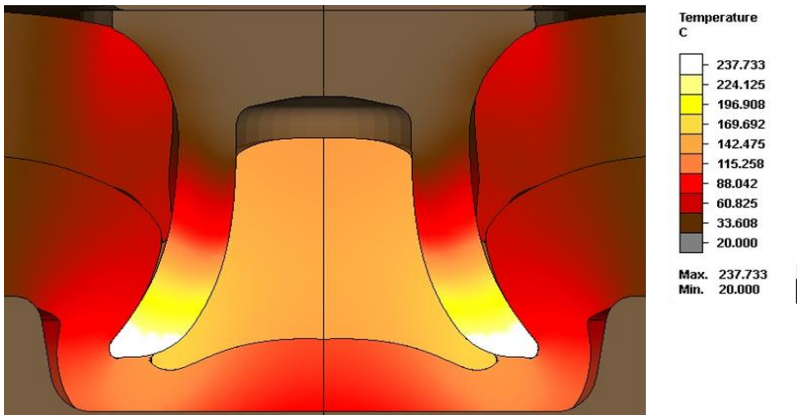

Figure 28. Temperature profile obtained with the numerical analysis

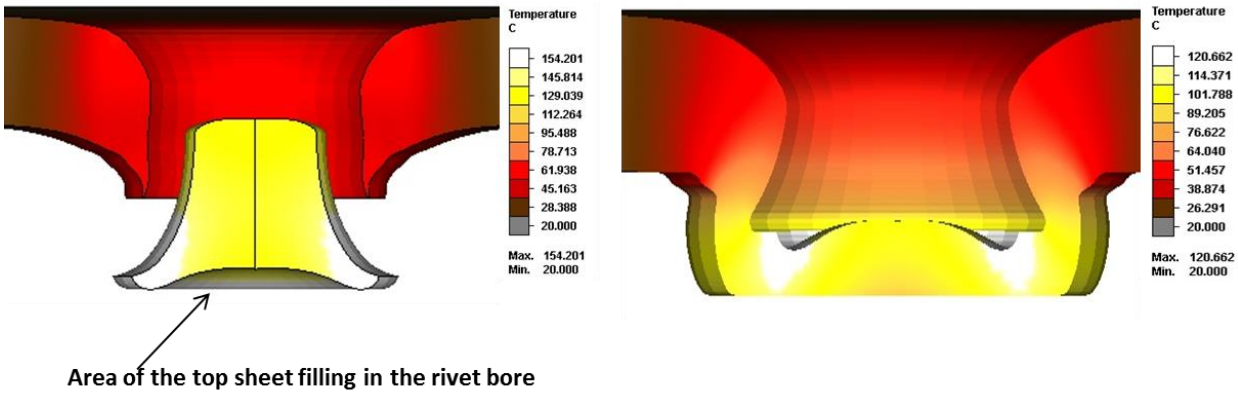

Figure 29. Temperature profile: a) top layer, b) bottom layer

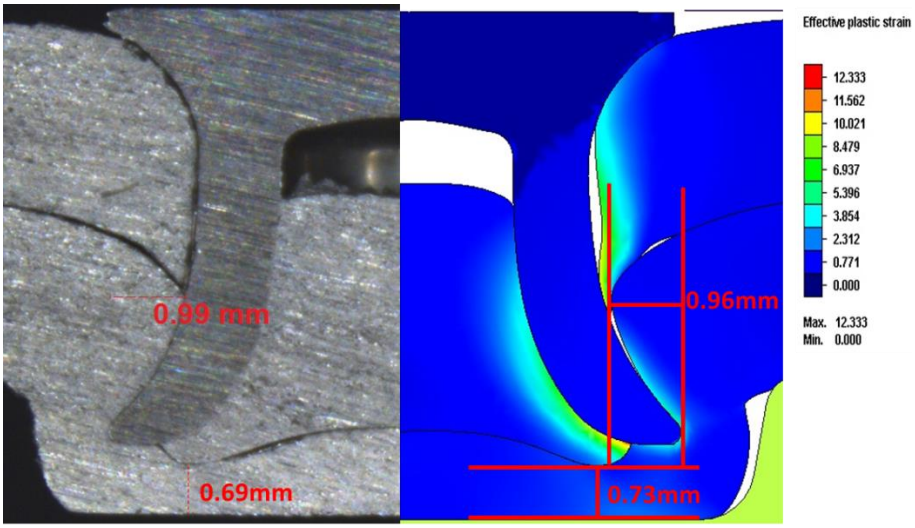

Figure 30. Comparison between experimental and numerical cross-section obtained with thermo-mechanical model

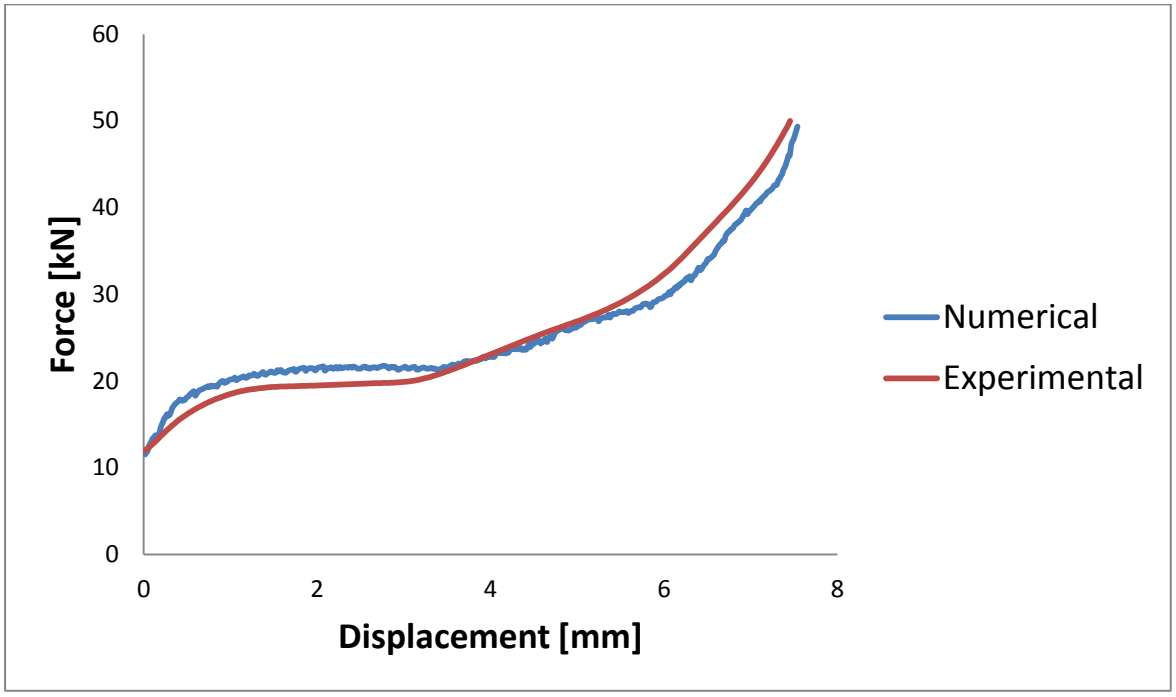

Figure 31. Comparison between force vs displacement curves of experimental and numerical model

Finally, in order to highlight the importance of the need to consider the softening effect of the substrate materials during the SPR process, a finite element model without thermo-mechanical coupling was developed. Figure 32 shows that the numerical cross-section has reported significant variation in comparison to the experimental test. Indeed, the remaining thickness (T_{min}) is greater than the experimental test which indicates that the bottom sheet material has higher resistance to the plastic flow. It can also be noticed that the rivet leg of

the numerical model showed greater compression in comparison to the experimental test. The latter can also be explained by the higher strength exhibited by the substrate materials without taking into account for thermal softening.

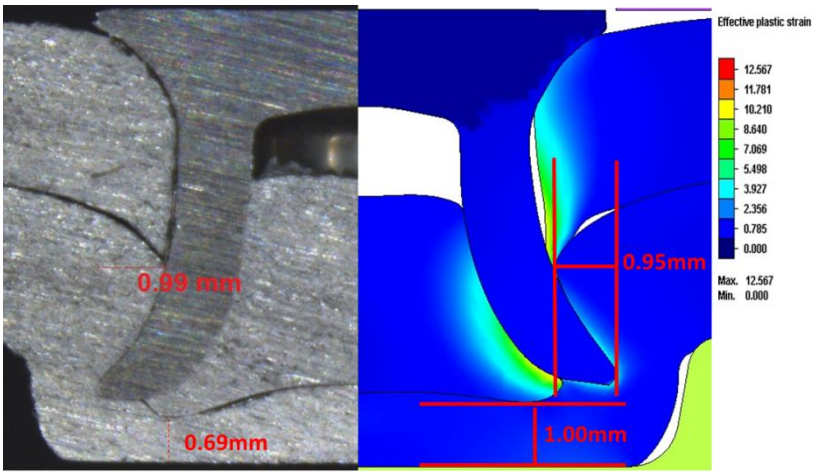

Figure 32. Comparison between experimental and numerical cross-section obtained with isothermal model

5.4 Effect of Punch speed, friction coefficients and thermal conductivity on temperature profile

In this section the sensitivity of the thermo-mechanical model to punch speed, friction coefficients and thermal conductivity will be analysed. Starting from the standard model developed in the previous paragraph and listed as "model 1" in Table 7, a further six simulations have been performed. Two models (2 and 3) consider the effect of different friction coefficients, two models (4 and 5) analyse the effect of the velocity at which the rivet is inserted and finally, two models (6 and 7) consider the effect of the thermal conductivity of the materials. For all the models, the Taylor- Quinney coefficient (β) was set equal to 0.9 while thermal conductivity of the rivet and specific heat capacity of rivet and substrate materials are listed in Table 6.

Table 7. Input parameters for numerical simulations

Model	Friction coefficients	Punch velocity [mm/s]	Thermal conductivity of aluminium [J/m*s*K]
1	0.09 (rivet – sheet) 0.09 (sheet – sheet) 0.15 (bott. sheet – die)	100	188
2	0.06 (rivet – sheet) 0.06 (sheet – sheet) 0.1 (bott. sheet – die)	100	188
3	0.12 (rivet – sheet) 0.12 (sheet – sheet) 0.22 (bott. sheet – die)	100	188
4	0.09 (rivet – sheet) 0.09 (sheet – sheet) 0.15 (bott. sheet – die)	50	188
5	0.09 (rivet – sheet) 0.09 (sheet – sheet) 0.15 (bott. sheet – die)	200	188
6	0.09 (rivet – sheet) 0.09 (sheet – sheet) 0.15 (bott. sheet – die)	100	167
7	0.09 (rivet – sheet) 0.09 (sheet – sheet) 0.15 (bott. sheet – die)	100	200

Figure 33 and 34 show the temperature vs time curves of top and bottom sheets obtained from all the testing conditions. It can be noticed that model 4 and 5, which correspond to the lowest (50 mm/s) and highest (200 mm/s) punch velocities, have shown respectively the

smallest and greatest peak temperature in both top and bottom sheets. This result indicates that the velocity of rivet insertion is the main factor affecting the magnitude of adiabatic heating. It is expected that at high punch speed there is less time to conduct the heat away therefore the adiabatic heating has greater effect on the thermal softening of the material. In this case, at punch speed of 200 mm/s the process was about three times faster than what achieved with the punch speed of 50 mm/s. It can be noticed that all the curves representative of the top layers (Figure 33) showed a drop in temperature which correspond to the time step when the element removal from the top sheet takes place.

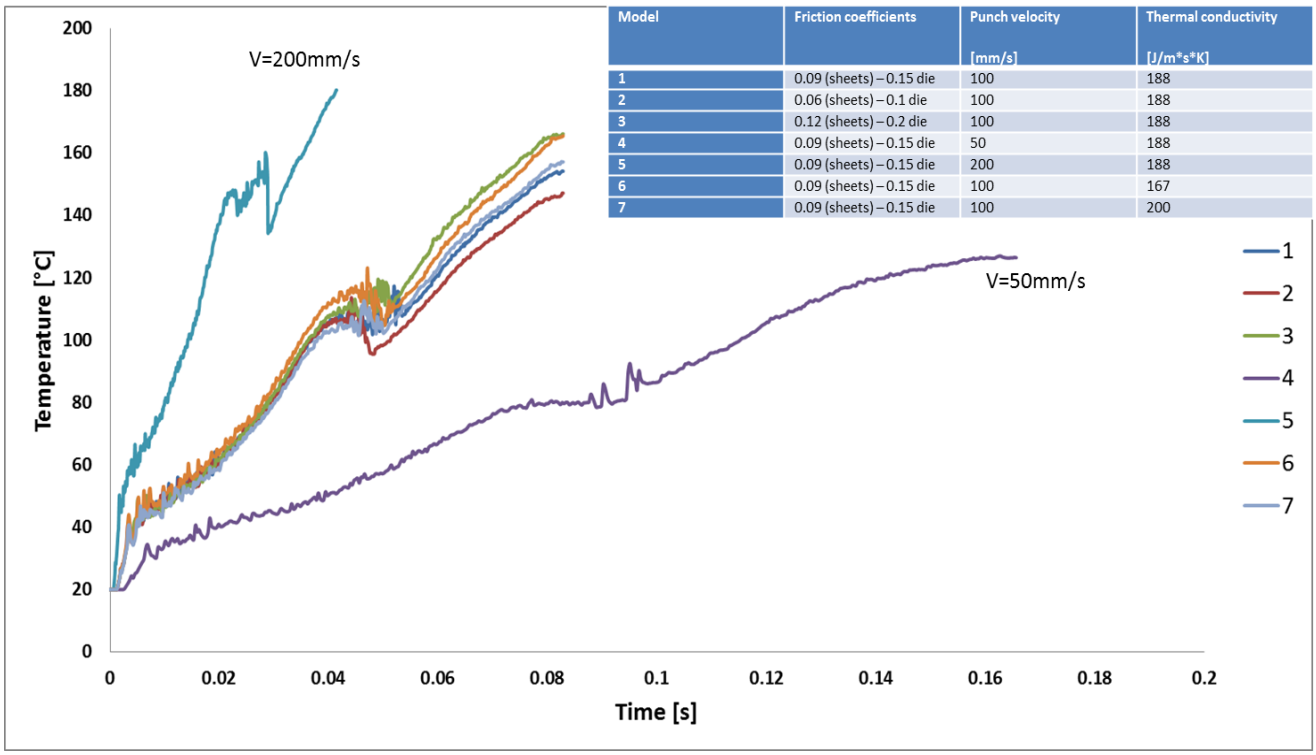

Model	Friction coefficients	Punch velocity [mm/s]	Thermal conductivity [J/m*s*K]
1	0.09 (sheets) – 0.15 die	100	188
2	0.06 (sheets) – 0.1 die	100	188
3	0.12 (sheets) – 0.2 die	100	188
4	0.09 (sheets) – 0.15 die	50	188
5	0.09 (sheets) – 0.15 die	200	188
6	0.09 (sheets) – 0.15 die	100	167
7	0.09 (sheets) – 0.15 die	100	200

Figure 33. Modelled temperature vs time curves of top layers

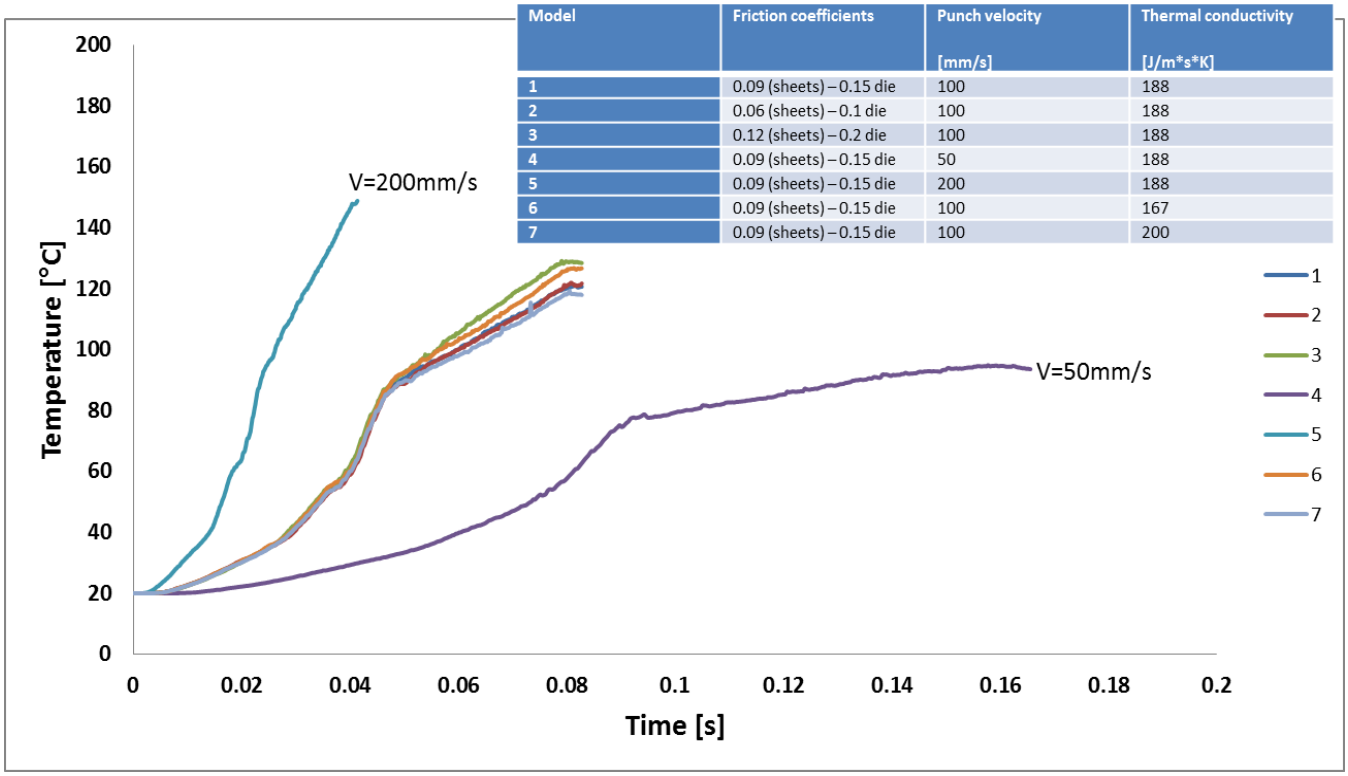

Figure 34. Modelled temperature vs time curves of bottom layers

Table 8 shows the joint characteristics obtained with the seven models. It can be noticed that the highest and lowest value of remaining thickness (T_{min}) are obtained respectively with punch speed of 50 mm/s and 200 mm/s. This result is consistent with the higher softening effect at the velocity of 200 mm/s which increases the plastic flow of the bottom sheet material within the die. A comparison between the cross-section geometries of the two models is shown in Figure 35.

For the interlock, which measures how much the rivet legs are spread within the bottom sheet, one of the main affecting parameter was found to be the friction coefficient. Indeed, model 3, which considered the highest friction coefficient between rivet and substrate materials, showed the lowest value of interlock. This result suggested that for this particular rivet and die combination, by increasing of friction coefficient the rivet goes deeper and flares less. Figure 36 shows the deformation of the rivet leg obtained with model 2 ($\mu = 0.06$) and model 3 ($\mu = 0.12$). Although, the friction coefficient affects the level of spreading of the

rivet leg, its impact on the temperature profile was marginal for the range of values selected. Finally, models 6 and 7 referred respectively to the lowest and highest thermal conductivity. In this case, a slight variation in terms of interlock and temperature profile was observed, however, its effect can be considered negligible.

Table 8: List of joint characteristics and peak temperatures obtained via simulation for the seven models

Model	Interlock [mm]	T_{min} [mm]	Peak temperature of the top sheet [°C]
1	0.96	0.73	154
2	0.97	0.75	146
3	0.86	0.68	166
4	0.95	0.78	126
5	0.92	0.63	182
6	0.96	0.7	165
7	0.92	0.7	151

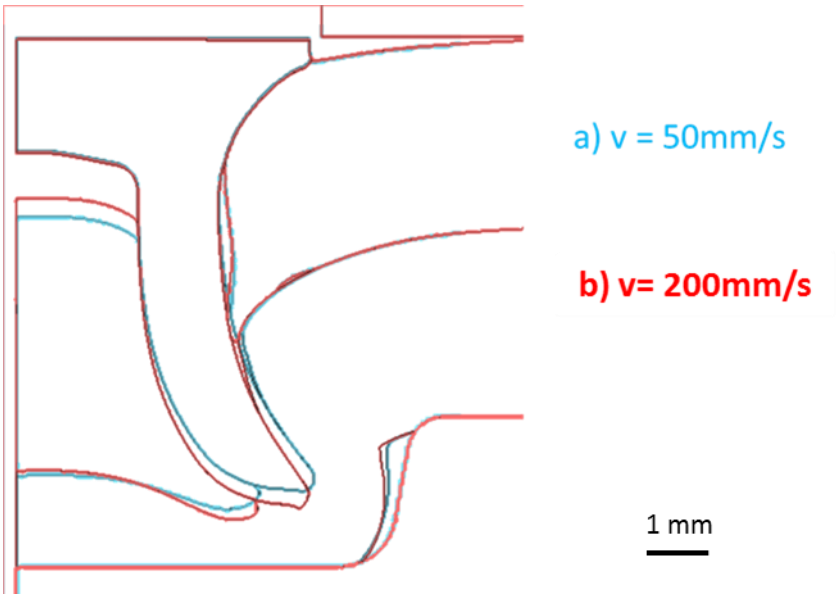

Figure 35.Comparison of cross-section geometries obtained with different punch speed. a)v=50mms, b)v=200mm/s

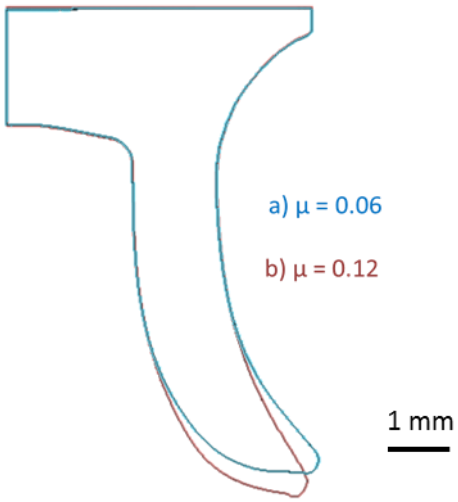

Figure 36. Effect of friction coefficient on the deformation of rivet leg. a) μ=0.06, b) μ=0.12

6. Development of material models

This chapter discusses the material model development for two aluminium alloys: a 5xxx (AA5754) and a 6xxx (AC600T4) series alloys which are widely used in JLR's BIW structures.

Uni-axial tensile tests under different temperature and strain rates have been performed in order to take into account the effect of thermal softening and strain hardening in the material model. It is acknowledged that the adiabatic heating generated during the SPR process does not lead to phase transformations due to the high speed of the process. With respect to the methodology described in Chapter 3 for the tensile tests at high temperature, the materials are exposed at high temperature for longer time (if considering soaking time and testing time) in comparison to what is experienced during the SPR process. However, according to the phase diagram of Al-Mg, it can be assumed that under the specific testing temperatures and chemical composition of the alloys used in this study, no solid solution transformations are expected (King, 1987).

Further, in the case of AC600T4, the effect of natural ageing on the mechanical properties has been reproduced by developing material models representative of different material aging conditions. The validation of the substrate material models was performed using a series of SPR joints representative of JLR industrial applications.

6.1 AA5754

The material under investigation is Novellis AA5754. This alloy is largely used in the automotive industry due to the favourable mechanical properties in terms of high strength to weight ratio, and high formability. Its main application is for structural and inner parts as its employment for outer body is limited by the surface inhomogeneity that occurs during the forming process due to the Portevin-Le Chatelier effect (Bloek, 2012). Table 9 lists the chemical composition of the AA 5754 which emphasise that Mg is the main alloying element:

Table 9: Nominal composition of AA5754 in wt%

Fe	*Si*	*Cu*	*Mn*	*Mg*	*Cr*	*Zn*	*Ti*
0.35	0-0.35	0-0.15	0-0.55	2.9-3.55	0-0.15	0-0.25	0-0.15

6.1.1 True stress and strain curves

The previous chapter showed that the temperature generated during the SPR process affects the plastic deformation of the substrate material. However, as SPR is a fast process which occurs in a fraction of second, the effect of strain rate on the work hardening of the material might affect the plastic behavior of the substrate materials under riveting condition. The experimental procedure used for the tests is described in Submission 2 and (Carandente et all, 2015) whilst the testing conditions used to perform the tests are listed in table 10.

Table 10. Experimental parameters used for tensile testing

Strain rate [s^{-1}]	Temperature [ºC]			
0.01	20	200	250	300
0.1	-	200	250	300
1	20	200	250	300

The true stress and true strain curves at the different temperature regimes are shown in Figure 37. Figure 37a shows that at the ambient temperature, the strain rate does not significantly affect the flow stress of the material. This behaviour is due to the dynamic strain aging, as a result of the interaction between dislocations and solute atoms. As stated in (Kabirian *et al.*, 2014), at low strain rates and room temperature, sufficient time is available for the solute magnesium atoms to merge into larger clusters. As a result, greater resistance to dislocation motion is provided (Abedrabbo *et al.*, 2006). As the temperature is increased, the work hardening behaviour of the material is affected by the strain rate. In Figure 37 (b), (c) and (d) it can be seen that at high temperature the flow stress decreases with decreasing strain rate and at 300°C with a strain rate of $0.01s^{-1}$, the material shows less work hardening behaviour compared to the other testing conditions. As stated in (Abedrabbo *et al.*, 2007) the decrease in flow stress at high temperature is due to the increase in mobility of the solute atoms.

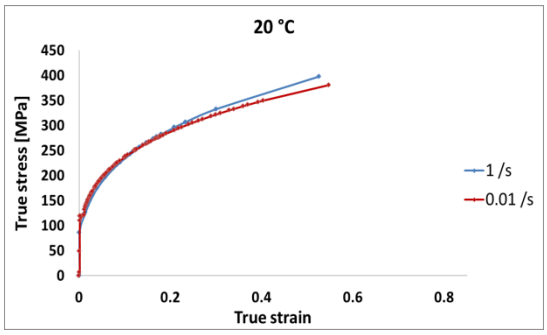

a)

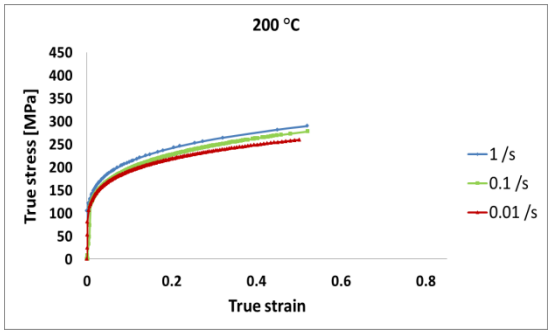

b)

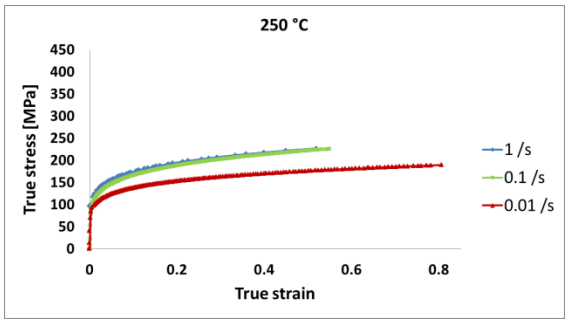

c)

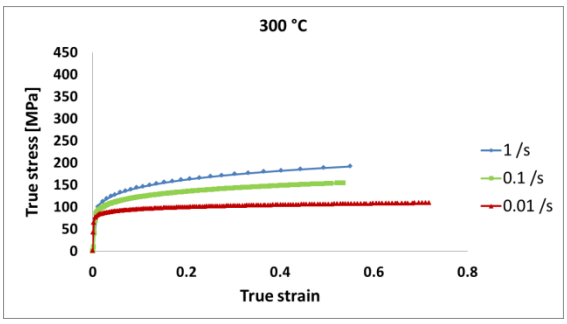

d)

Figure 37. Effect of strain rate on the true stress vs true strain curves at different temperature: a) 25 ºC. b) 200 ºC. c) 250 ºC and d) 300 ºC.

In this study, the deformation of the samples during testing was measured using DIC technique discussed in Chapter 3. However, as a consequence of the localized plastic deformation occurring in the area of the neck, the Aramis ^{tm} system was not able to measure the stress and strain at fracture due to the deterioration of the pattern painted on the sample (Figure 38).

Figure 38. Deterioration of the patter in the area of the neck

Therefore, the true stress at fracture was determined from measurements of the fracture area made in the Scanning Electron Microscope (SEM). This approach was able to take into account changes in both width and thickness due to necking. Figure 39 shows the curves

including stress and strain at fracture. The strain at fracture was calculated assuming volume constancy and using the following equation:

$$\varepsilon_f = \ln(\frac{A_0}{A_f}) \qquad (2)$$

where ε_f is the strain at fracture (Table 11), A_0 is the initial area and A_f is the area of fracture calculated from SEM measurements. The stress at fracture was then calculated using the Holloman equation:

$$\sigma_f = k\varepsilon_f^{n} \qquad (3)$$

where σ_f is the stress at fracture, k is the strength coefficient and n is the strain hardening coefficient listed in Table 11.

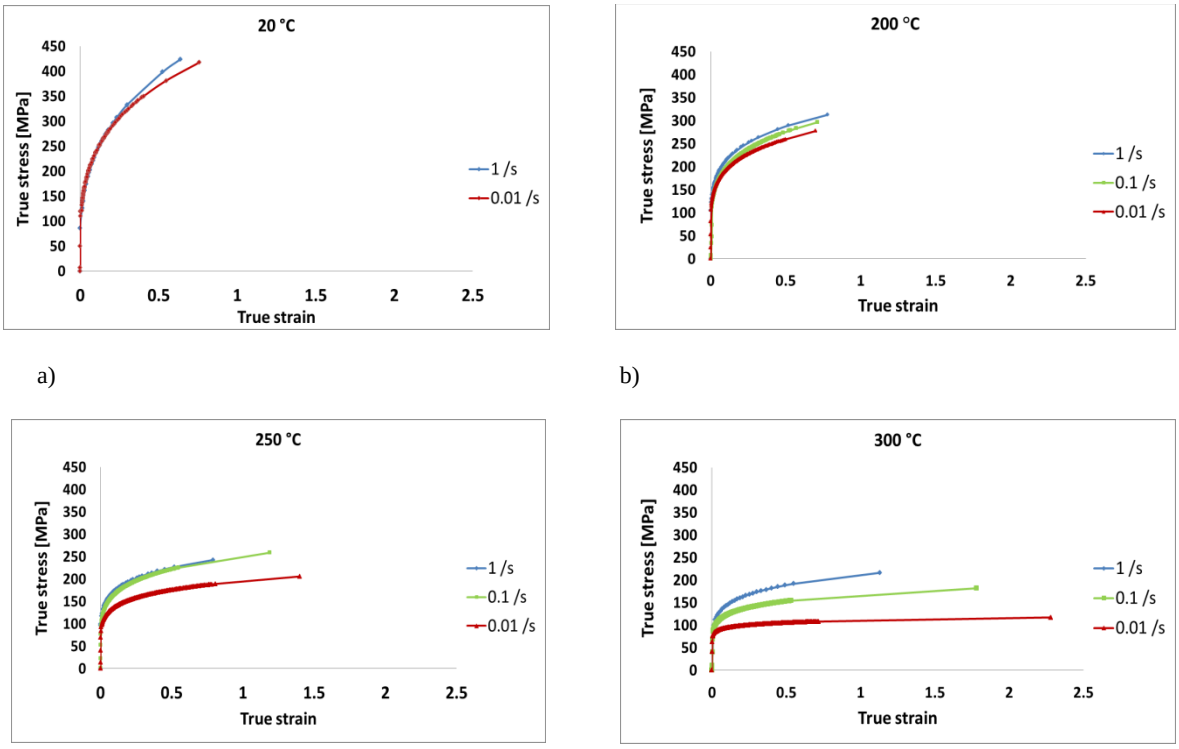

a) b)

c) d)

Figure 39. True stress vs true strain curves at strain rate of 0.01s^{-1}, 0.1 s^{-1} and 1s1 including strain at fracture: a) 25 ºC. b) 200 ºC. c) 250 ºC and d) 300 ºC

It can be noticed that at the ambient temperature and 200 ºC, the strain at fracture is not significantly affected by the strain rate. However, at higher temperatures (250 ºC and 300 ºC) the strain at fracture increases with decreasing strain rate. This behaviour is shown by the evolution of the fracture area as function of the strain rate and temperature in Figure 40.

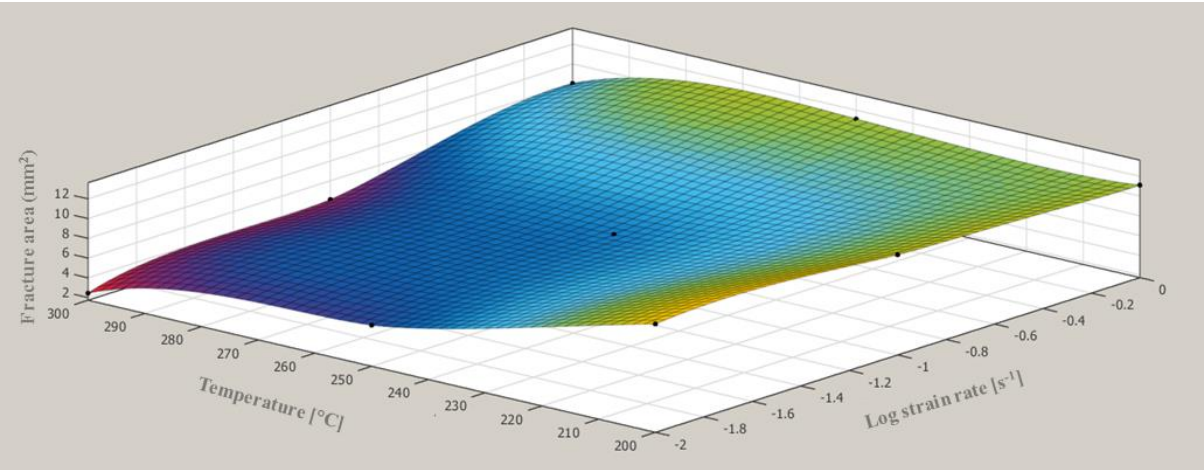

Figure 40. Evolution of the strain at fracture as a function of strain rate and temperature

6.1.2 Calculation of flow curves

The material data are implemented into the FEM by means of flow curves which describe the evolution of true stress and true strain in the plastic regime. The Holloman's equation was used to generate data points for each flow curve in order to implement them into the FEM in the form of a lookup table. The following equation describes the Hollomon hardening rule:

$$Y = k(\varepsilon_p)^n \qquad (4)$$

where Y is the effective plastic stress and ε_p is the effective plastic strain. The proof stresses ($Rp_{0.2}$), strain at fracture and material constants for each test condition are listed in Table 12, while Figure 41 shows the flow curves calculated at the nominal strain rates of $0.01s^{-1}$, $0.1s^{-1}$ and $1s^{-1}$ for each temperature regime. As indicated in Table 12, the strain hardening coefficient (n) increses with strain rate and decreases with temperature. Similar behaviour was observed for the strenght coefficinet (k).

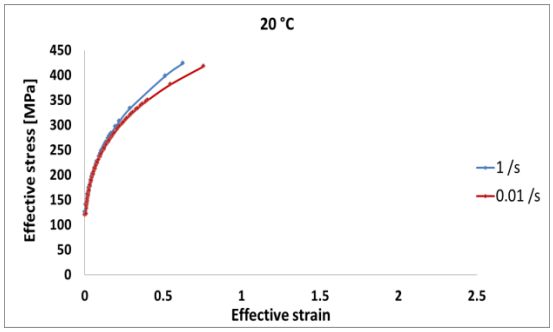

a)

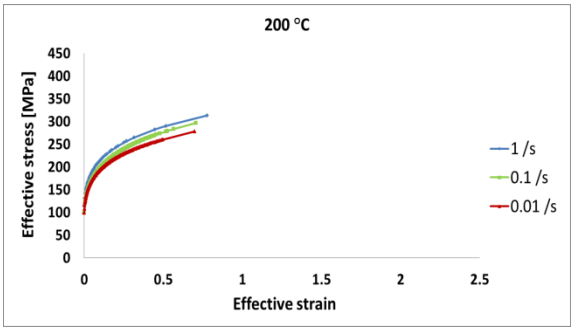

b)

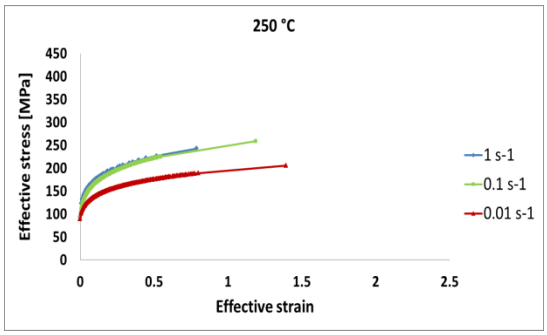

c)

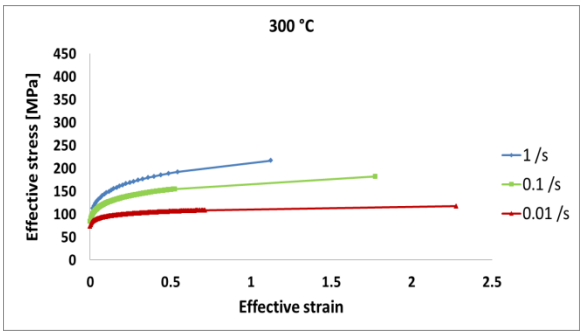

d)

Figure 41. Flow curves at strain rate of 0.01s s-1, 0.1 s-1 and 1s-1: a) 25 ºC. b) 200 ºC. c) 250 ºC. d) 300 ºC.

Table 11. Experimental parameters determined from tensile testing

Temperature [°C]	$Rp_{0.2}$ ($0.01s^{-1}$) [MPa]	$Rp_{0.2}$ ($0.1s^{-1}$) [MPa]	$Rp_{0.2}$ ($1s^{-1}$) [MPa]	k ($0.01s^{-1}$) [MPa]	k ($0.1s^{-1}$) [MPa]	k ($1s^{-1}$) [MPa]	n ($0.01s^{-1}$)	n ($0.1s^{-1}$)	n ($1s^{-1}$)	εf ($0.01s^{-1}$)	εf ($0.1s^{-1}$)	εf ($1s^{-1}$)
20	120	-	122	451	-	489	0.28	-	0.32	0.76	-	0.64
200	99	101	115	296	318	328	0.19	0.21	0.22	0.70	0.71	0.78
250	90	90	94	198	251	252	0.15	0.17	0.18	1.40	1.19	0.79
300	74	83	87	111	170	212	0.072	0.14	0.17	2.28	1.78	1.13

6.1.3 Effect of temperature and strain rate on simulation results

In order to assess the effect of thermal softening and strain-rate hardening, the comparison between three different models will be provided in this section.

In the first, the mechanical behaviour of the substrate materials was defined by only using data derived at room temperature and strain rate of $1s^{-1}$. In the second the flow curves at room temperature, 200 °C, 250 °C and 300 °C and a strain rate of $1s^{-1}$ were implemented in order to take into account the thermal softening of the AA5754 alloy. In the third model, the mechanical behaviour of the substrate material was implemented by means of flow curves obtained at room temperature, 200 °C, 250 °C and 300 °C and strain rate of 0.01 s^{-1}.

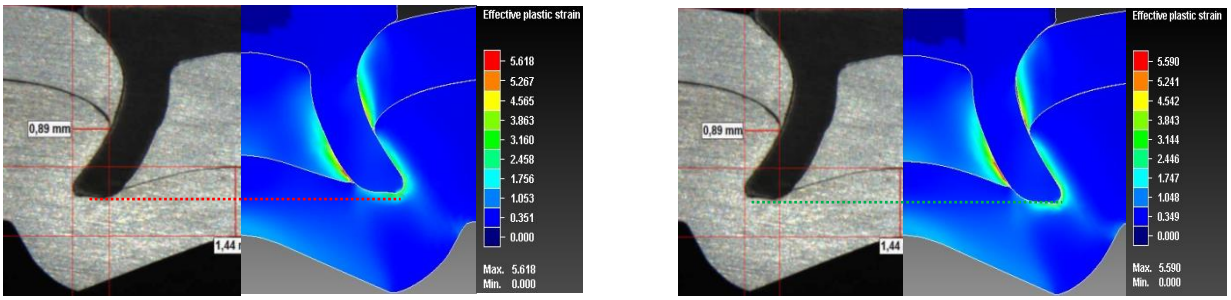

a) b)

Figure 42. Comparison between experimental and numerical cross-sectional geometries: a) Numerical simulation using data derived at room temperature and a strain rate of $1s^{-1}$. b) Numerical simulation using data derived at 25°C, 200°C, 250°C, 300°C and strain rate of $1s^{-1}$.

The cross-sectional geometry obtained from the isothermal model shows that the deformation of the rivet leg is higher compared to the experimental test, while in the thermo-mechanical model the deformation of the rivet leg was more representative of the experimental test (Figure 42). Figure 43 shows the comparison between the deformations of the rivet legs achieved with the two models. The higher compression of the rivet leg obtained with the room temperature model indicates that there was more resistance to the rivet insertion when the softening effect of the substrate

materials was not considered. As discussed in the previous chapter, material in the vicinity of the rivet experiences the largest deformation and hence sees the highest temperature rise. This has the effect of producing soft zones around the rivet which will deform in preference to the rivet, leading to a lower degree of interlock.

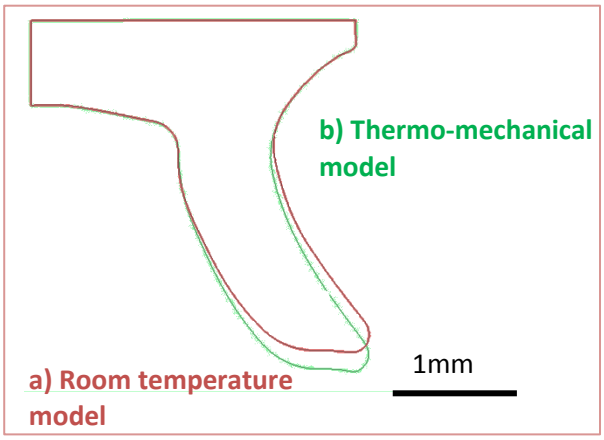

Figure 43. Effect of temperature on plastic deformation of rivet leg: a) Numerical model with only flow curve at room temperature and strain rate of 1s-1. b) Numerical model with flow curves at 25°C, 200°C, 250°C, 300°C and strain rate of 1s-1.

The effect of the strain rate on the final cross section geometry of the SPR joint is shown in Figure 44. In Figure 44a, the mechanical behaviour of the substrate material was implemented by means of a flow curve obtained at the strain rate of 0.01 s^{-1}, whilst in Figure 44b the flow curves were generated at the strain rate of 1 s^{-1}. In both the cases, the flow curves implemented into the finite element model were at room temperature, 200 °C, 250 °C and 300 °C.

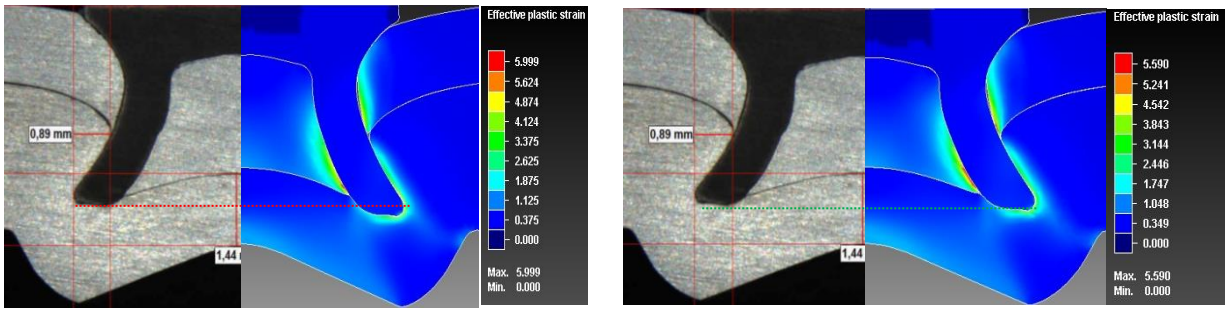

a) b)

Figure 44. Comparison between numerical and experimental cross-sectional geometries: a) Numerical model with flow curve at temperatures of 25°C, 200°C, 250°C, 300°C and strain rate of 0.01s-1. b) Numerical model with flow curves at temperatures of 25°C, 200°C, 250°C, 300°C.

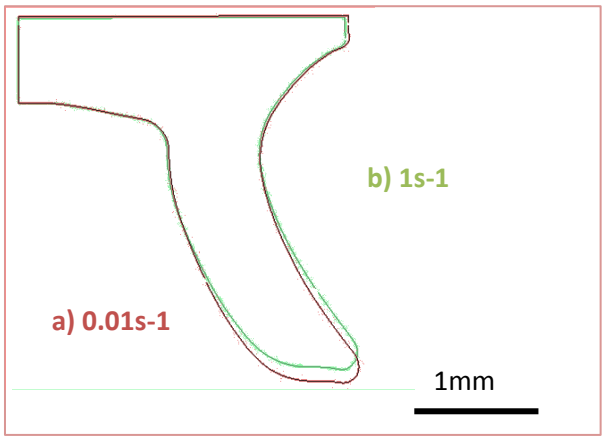

Figure 45. Effect of strain rate on plastic deformation of rivet leg: a) Numerical model with flow curve at temperatures of 25°C, 200°C, 250°C, 300°C and strain rate of $0.01s^{-1}$. b) Numerical model with flow curves at temperatures of 25°C, 200°C, 250°C, 300°C and strain rate of $1s^{-1}$.

The comparison between the two models shows that for model one, the rivet goes deeper compared to the experimental test. For model 2, a better representation of the cross-section with respect to the experimental tests was obtained. Figure 45 shows the comparison between the deformations of the rivet legs achieved with the two models. It can be seen that strain rate of $1s^{-1}$ produces a rivet leg slightly more compressed than the model at the strain rate of $0.01s^{-1}$. This result can be attributed to the higher strength and work-hardening behaviour of the substrate materials at the strain rate of $1s^{-1}$ creating a higher resistance to deformation by the rivet. In general, the strain rate field occurring during the SPR process is affected by the specific application such as rivet length, stack thickness and die shape. A reasonable range of strain rate field could be between 10 s^{-1} – 30 s^{-1}, where the bottom end of the range was calculated assuming a velocity of 100 mm/s and a stack of 9 mm thickness while the top end was calculated assuming a stack of 3 mm thickness. The material data used for the simulation were generated at a strain rate of $1s^{-1}$ due to instrument limitations in achieving higher strain rates. Moreover, this approximation is in agreement with the consideration that for aluminium alloys the strain rate sensitivity is negligible at temperatures below 200 °C (Li and Ghosh, 2003).

6.2.4 Validation of the substrate material model

In order to validate the robustness of the material model together with the boundary conditions, six different material stacks with different rivet and die combinations, representing SPR application in the automotive industry, were simulated using the material data at a strain rate of $1s^{-1}$ and temperatures of 20 °C, 200 °C, 250 °C and 300 °C. The comparisons between the cross-sectional geometries of the numerical and experimental tests were assessed by comparing the joint characteristics parameters indicated in Figure 10. The measurements of the experimental mean values were carried out from the experimental tests by considering five repeats for each joint configuration.

As listed in Table 12, the variables of the seven joins under investigation were: material thicknesses, rivet length, rivet hardness and die profile.

Table 12. Joint variables

Joint No.	Stack	Rivet (length and hardness)	Die
1	1.5mm+1.5mm	5mm-H0	B (Flat)
2	1.2mm+1.5mm	5mm-H0	B (Flat)
3	2mm+2mm	6mm-H0	C (Pip)
4	1.5mm+2mm	6mm-H0	C (Pip)
5	1.5mm+1.5mm+2mm	7.5mm-H4	D (Flat)
6	1.5mm+2.5mm+2.5mm	8mm-H2	D (Flat)

Figure 46 shows the rivets and dies used in this study.

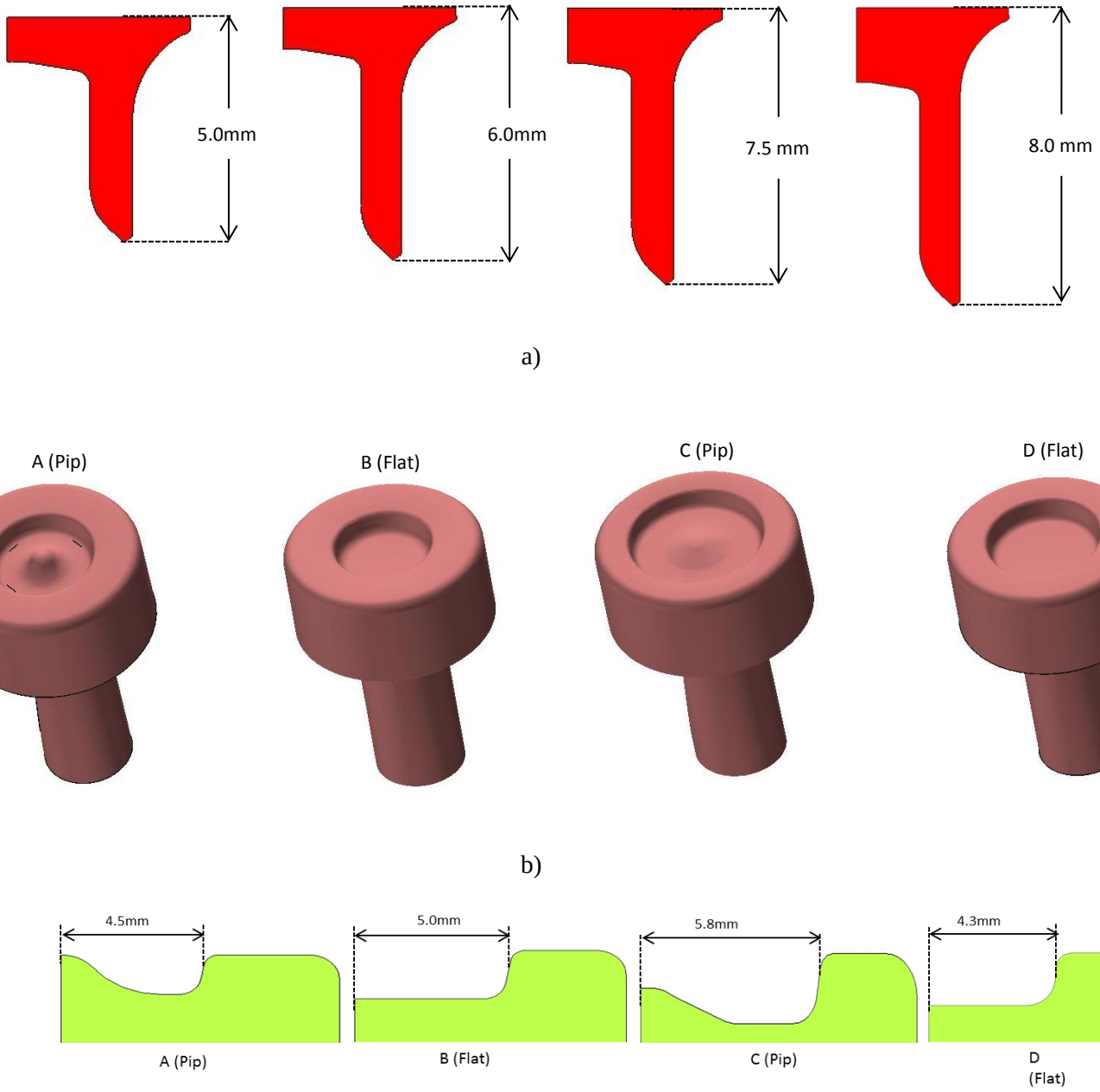

Figure 46. a) Rivet cross-sectional shapes. b) Die geometries. c) Die cross-sectional shapes

Figure 47 shows a comparison between the cross-sectional geometries of the experimental and numerical tests for a joint made of (1.5mm + 1.5mm) AA5754. The measurements of the joint characteristic parameters are listed in Table 14. The

average experimental interlock was 0.42mm while the value predicted from numerical analysis was 0.45mm. The average value of the experimental remaining material thickness (T_{min}) was 0.56mm while the predicted value was 0.53. The same good agreement in terms of cross-sectional geometry and joint characteristics was found for the other five configurations shown in Figures 48, 49, 50, 51, 52. In particular, it is worth noticing that the simulation was capable of predicting some of possible issues such as the gap between rivet head and upper sheet showed in joint 1, 2 and 3 (Figure 47, 48 and 49).

Table 6 shows that regardless of the joint configuration, a margin of error less than 0.1mm was found between experimental and predicted results. A comparison between the experimental and numerical force vs displacement curves was also provided for all joints in Figure 53. The good correlation between the curves indicates the appropriateness of the chosen boundary conditions and material data for the range of joints investigated.

Figure 54 shows comparisons between experimental and numerical joint characteristics measured using respectively room temperature and thermo-mechanical model. It can be noticed that the joint characteristics measured with the thermo-mechanical analysis are all in the range of the experimental results, while the isothermal model shows deviations, particularly in the case of T_{min} for three layer joints were higher thermal softening is expected as a result of the greater plastic work. Less variation between thermo-mechanical and isothermal results was observed for interlock. However, as shown in Figure 43, the numerical results can over predict the compression of the rivet leg without taking into account the thermal softening.

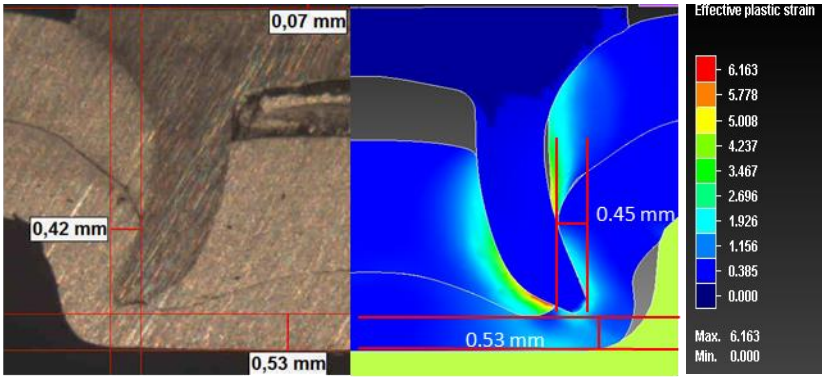

Figure 47. Comparison between cross-sectional geometries of joint 1: (1.5mm+1.5mm) AA5754

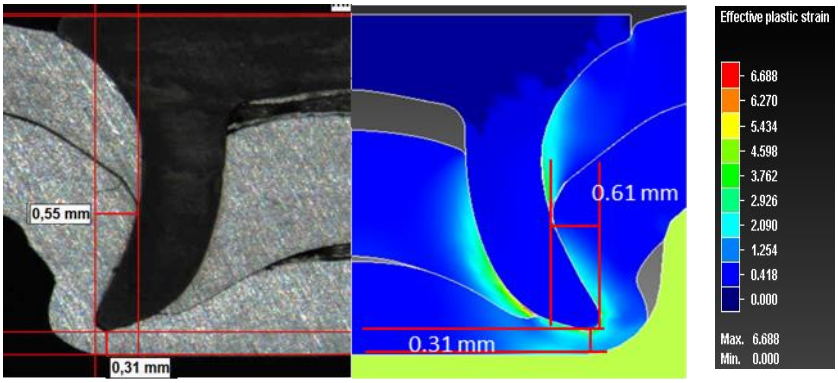

Figure 48. Comparison between cross-sectional geometries of joint 2: (1.2mm + 1.5mm) AA5754

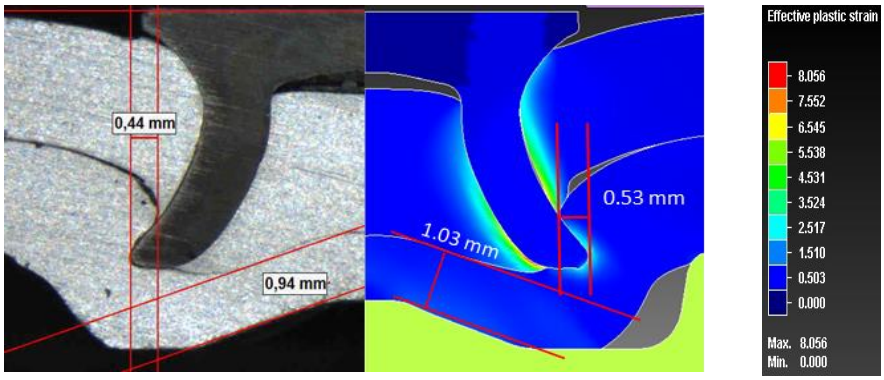

Figure 49. Comparison between cross-sectional geometries of joint 3: (2.0mm+2.0mm) AA5754

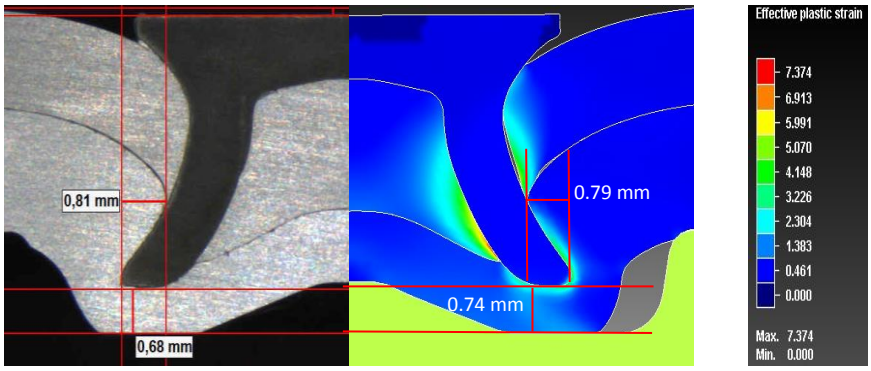

Figure 50. Comparison between cross-sectional geometries of joint 4: (1.5mm+2.0mm) AA5754

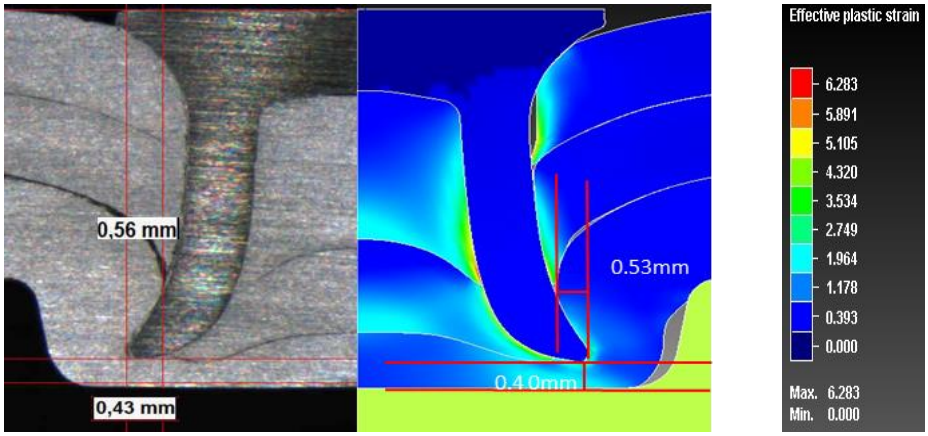

Figure 51. Comparison between cross-sectional geometries of joint 5: (1.5mm+1.5mm+2mm) AA5754

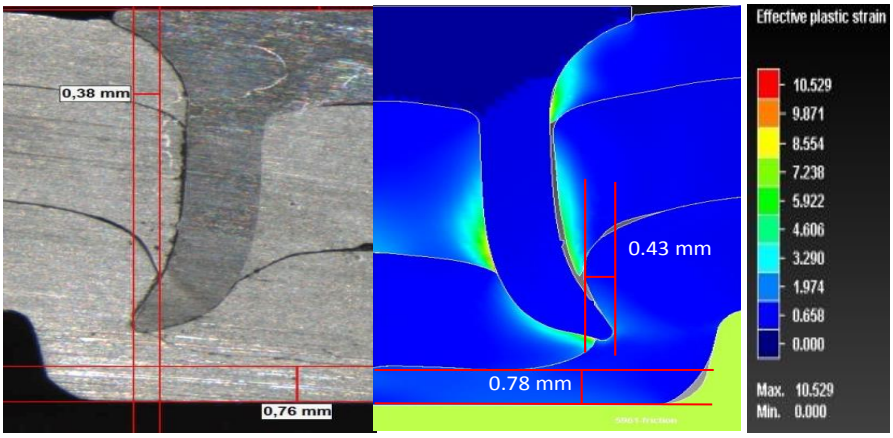

Figure 52. Comparison between cross-sectional geometries of joint 6: (1.5mm+2.5mm+2.5mm) AA5754

Table 13. Comparisons between experimental and numerical joint characteristics values

Joint	**Interlock experimental [mm]**	**Interlock numerical [mm]**	**Δ Interlock (exp.-num.) [mm]**	**T_{min} experimental [mm]**	**T_{min} numerical [mm]**	**Δ T_{min} (exp.-num.) [mm]**
1	0.45±0.09	0.45	-	0.56±0.09	0.53	0.03
2	0.54±0.08	0.61	-0.07	0.32±0.04	0.31	0.01
3	0.48±0.08	0.53	-0.05	0.97±0.08	1.03	-0.06
4	0.78±0.05	0.79	-0.01	0.74±0.1	0.74	-
5	0.55±0.06	0.53	0.02	0.43±0.06	0.4	0.03
6	0.45±0.07	0.43	0.02	0.82±0.17	0.78	0.04

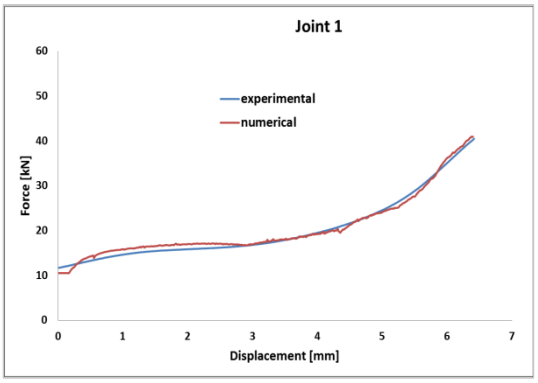

a)

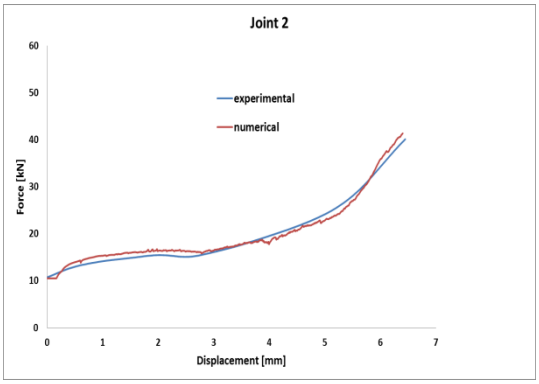

b)

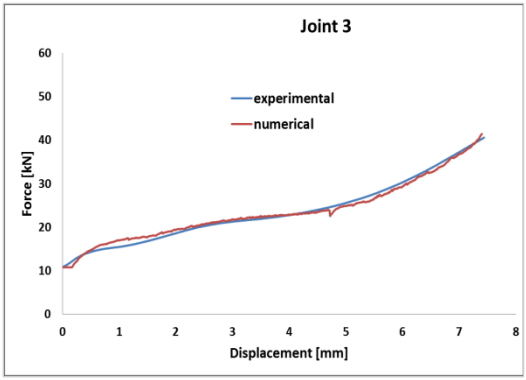

c)

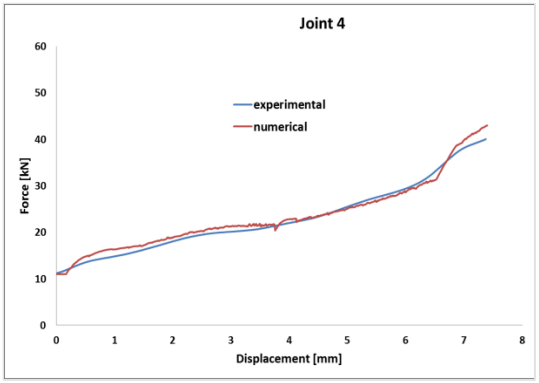

d)

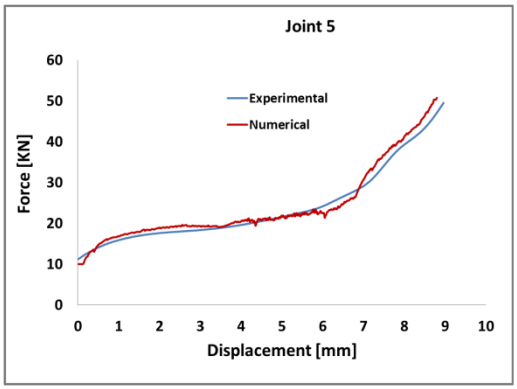

e)

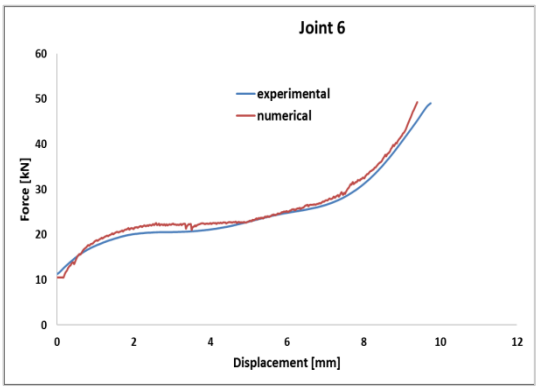

f)

Figure 53: Comparison of numerical (red lines) and experimental (blue lines) force vs displacement curves. a) joint 1, b) joint 2, c) joint 3, d) joint 4, e) joint 5, d) joint 6

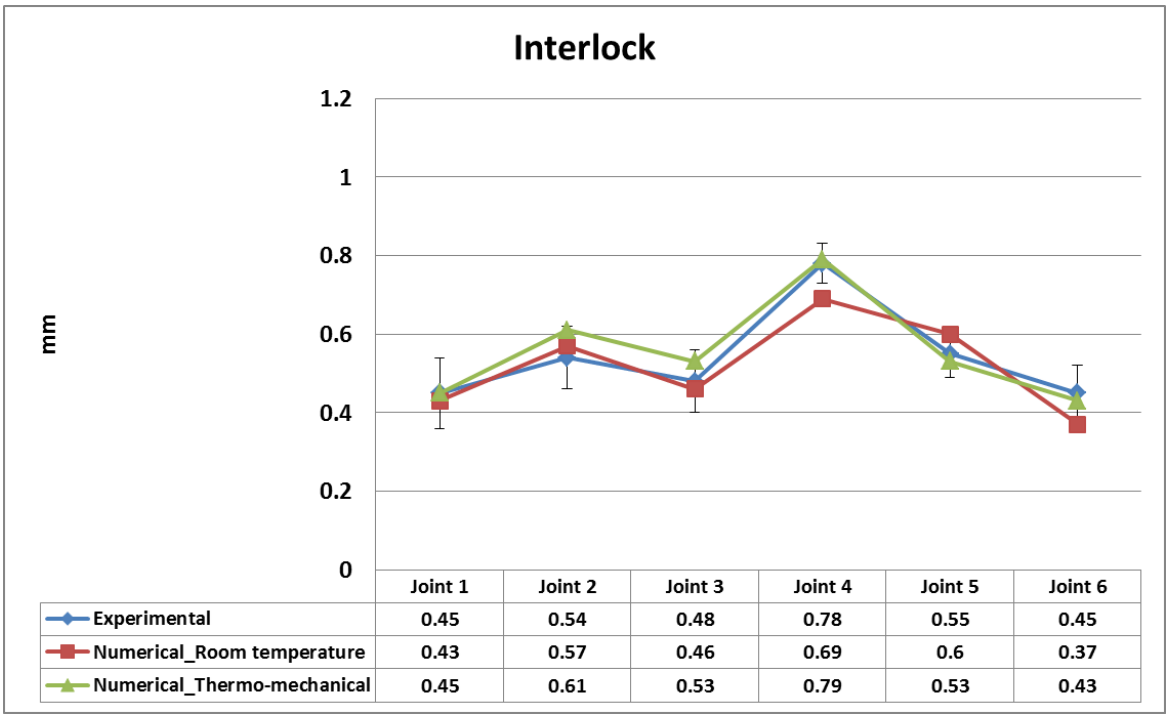

	Joint 1	Joint 2	Joint 3	Joint 4	Joint 5	Joint 6
Experimental	0.45	0.54	0.48	0.78	0.55	0.45
Numerical_Room temperature	0.43	0.57	0.46	0.69	0.6	0.37
Numerical_Thermo-mechanical	0.45	0.61	0.53	0.79	0.53	0.43

a)

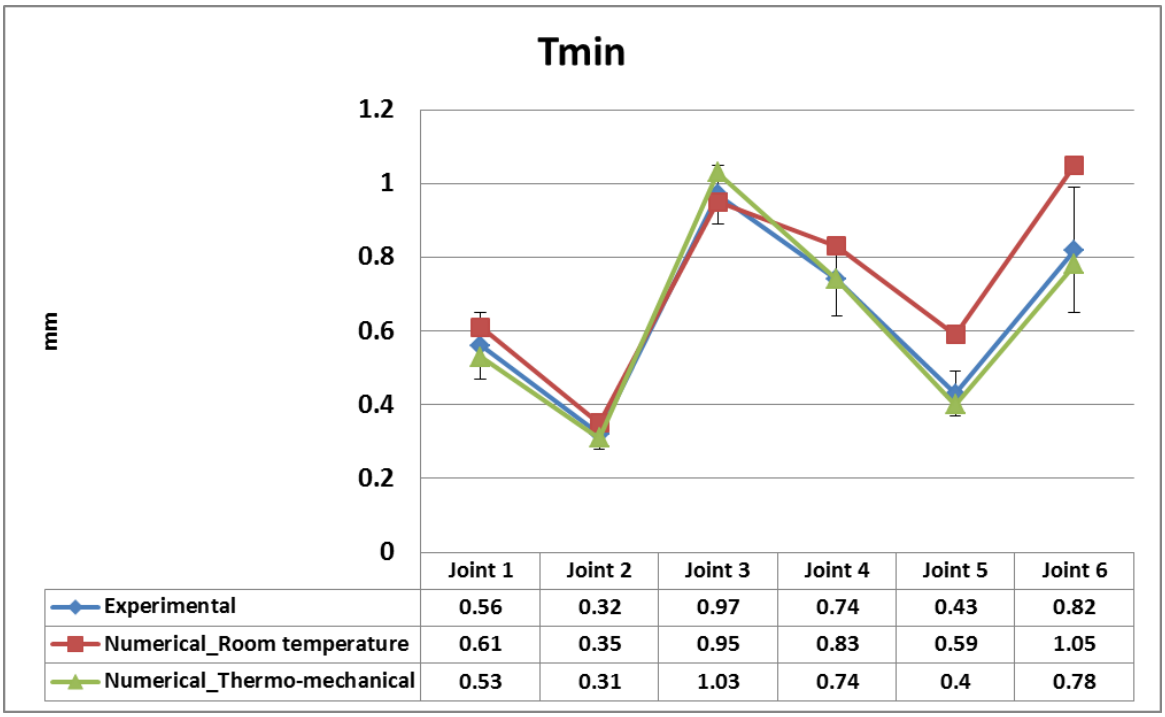

	Joint 1	Joint 2	Joint 3	Joint 4	Joint 5	Joint 6
Experimental	0.56	0.32	0.97	0.74	0.43	0.82
Numerical_Room temperature	0.61	0.35	0.95	0.83	0.59	1.05
Numerical_Thermo-mechanical	0.53	0.31	1.03	0.74	0.4	0.78

b)

Figure 54. Overall comparison between experimental and numerical joint characteristics values: a) Interlock, b)Tmin

6.2 AC600T4

In the next paragraphs the development and validation of the material model of a 6xxx series aluminum alloys will be described. The material under investigation is Novelis AC600 T4 aluminium alloy and its nominal composition is listed in Table 14. This material has been widely used by JLR in body structures for inner and structural applications. Both AA5754 and AC600 T4 alloys are characterized by good formability and energy absorption under crash conditions, however the Al-Mg-Si is preferred for body outer applications due to the surface irregularities (stretcher-strains) developed when press forming Al-Mg alloys (Bloek, 2012).

Table 14. Nominal composition of AC600 T4 in wt%

Fe	*Si*	*Cu*	*Mn*	*Mg*	*Cr*	*Zn*	*Ti*	*V*
0.35	0.3-0.95	0.25	0.15	0.4-0.85	0.15	0.15	0.15	0.15

The AlMgSi alloy gains its mechanical strength from a precipitation hardening process which involves the precipitation of Mg_2Si (magnesium silicide) particles (Mukhopadhyay, 2012) (Polmear, 2004).

The precipitation hardening is generally characterized by three main steps:

1. Solution treatment
2. Quenching
3. Ageing

During the solution treatment, the alloy is heated at a temperature just below the eutectic (Figure 55) in order to dissolve any precipitates and to ensure that the alloying elements are in the solid solution. During the quenching, the material is rapidly cooled in order to obtain a supersaturated solid solution (Mohamed and Samuel, 2012).

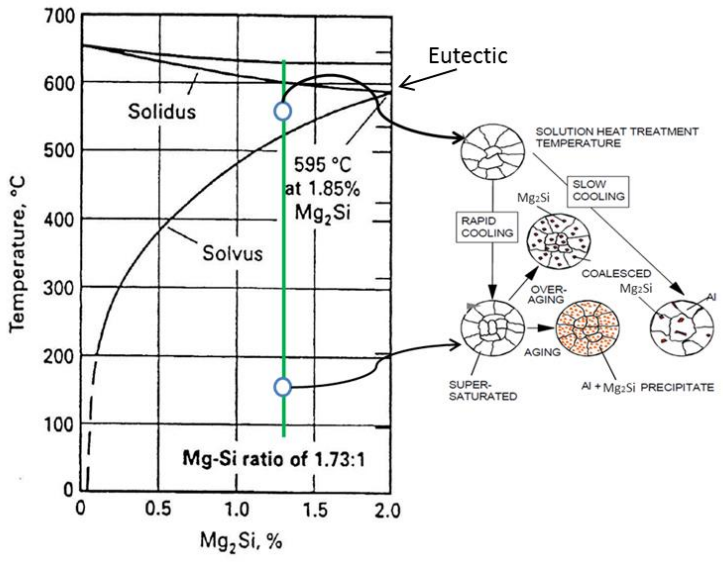

Figure 55: Phase diagram of Al-MgSi alloy showing the mechanism of precipitation hardening (Mohamed and Samuel, 2012)

The ageing process can be natural or artificial. In the first case, no heating processes are involved after quenching (Figure 56).

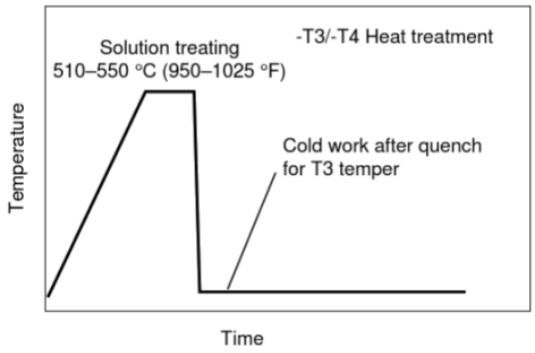

Figure 56: Time-Temperature profile for a solution treated and naturally aged alloy (Campbel, 2008).

This is the case of temper T4 which is used in automotive industry to enhance good formability during stamping operations. However, this is an unstable condition and the material hardens with time due to natural ageing of the material as a result of the precipitation of Mg_2Si at room temperature (Cao *et al.,* 2012). In general, three Mg_2Si precipitates having different sizes can be obtained: β", β' and β (Mariora et all. 2000). It was found that the particles β", which are characterized by a fine needle shape, have major contribution on the material strength (Tekada et all.,1998).

Although, the final strength of AC600T4 is achieved during the paint baking process, the effect of natural ageing on the mechanical properties is an important aspect that

needs to be considered in particular during the joining of the body panels through the SPR process. In JLR applications, this material can only be used for stamping and joining processes in a fixed time window in order to minimize the effect of natural ageing on the mechanical properties.

In the next paragraphs the effect of natural ageing on the joint characteristics will be discussed and material models representative of different age will be developed.

6.2.1 True stress and strain curves

In order to consider the effect of natural ageing on the mechanical properties of the AC600 T4, tensile tests at 3 months and 6 months were performed. Moreover, the effect of strain rate was analyzed by testing three months old samples at the strain rate of 0.01s-1, 0.1s-1 and 1s-1. The testing conditions used to perform the tensile tests are listed in Table 15.

Table 15: Experimental parameters used for tensile testing

Shelf life	Strain rate [s-1]	Temperature [°C]			
3 months	0.01 – 0.1 -1	20	200	250	300
6 months	1	20	200	250	300

Figure 57 shows the true stress vs true strain curves at 3 and 6 months ranging from room temperature to 300 °C. It can be observed that at each testing condition the flow stress increases with the natural ageing as a result of the precipitation hardening process. Similar to the AA5754 alloy, it was observed that the work-hardening decreases with temperature.

Figure 58 shows the true stress vs true strain at different strain rates for the three months old material. In this case the effect of strain rate on the work-hardening was less than what observed with the AA5754 alloy (Figure 37). Similar behaviour was

also observed by (Li and Ghosh, 2003) where the effect of strain rate was studied on a 5xxx and 6xxx-T4 aluminium alloy.

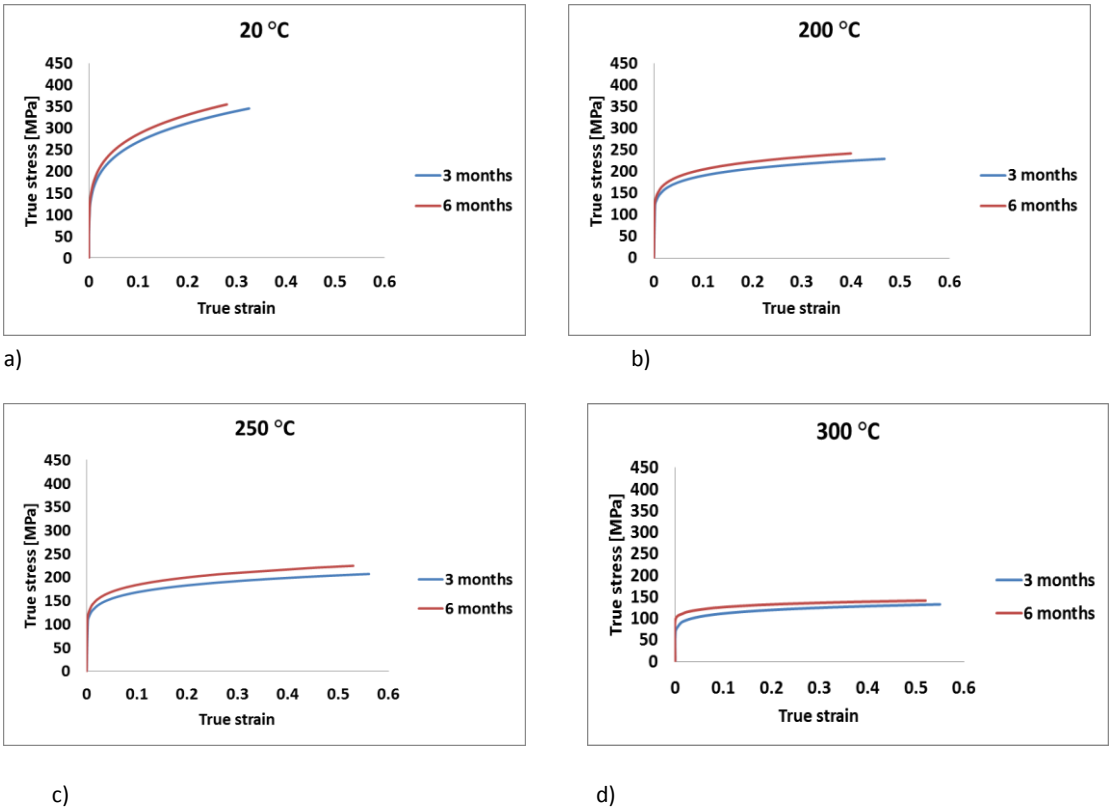

Figure 57: Comparison of true stress vs true strain curves at strain rate of s-1 and age of 3 and 6 months: a) 25 ºC, b) 200 ºC, c) 250 ºC, d)300 ºC

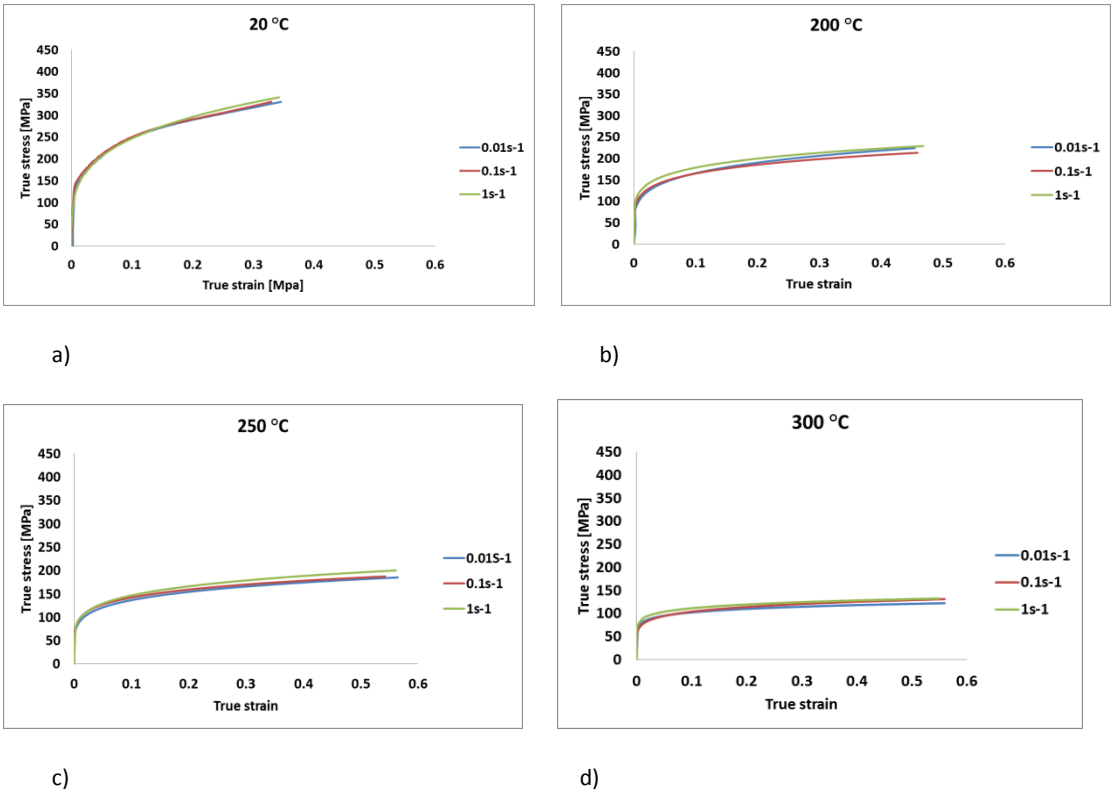

Figure 58: True stress vs true strain curves at strain rate of 0.01s-1, 0.1 s-1 and 1s1 and 3 months age: a) 25 °C. b) 200 °C. c) 250 °C and d) 300 °C

6.2.2 Calculation of flow curves

The procedure used for the calculation of the flow curves to implement into the FE models is the same as that discussed in the previous chapter for the calculation of the AA5754 flow curves. Figure 59 shows the flow curve at the strain rate of $1s^{-1}$ and temperature ranging from ambient to 300 °C including strain at fracture. The parameters of the Holloman equation are listed in Table 16.

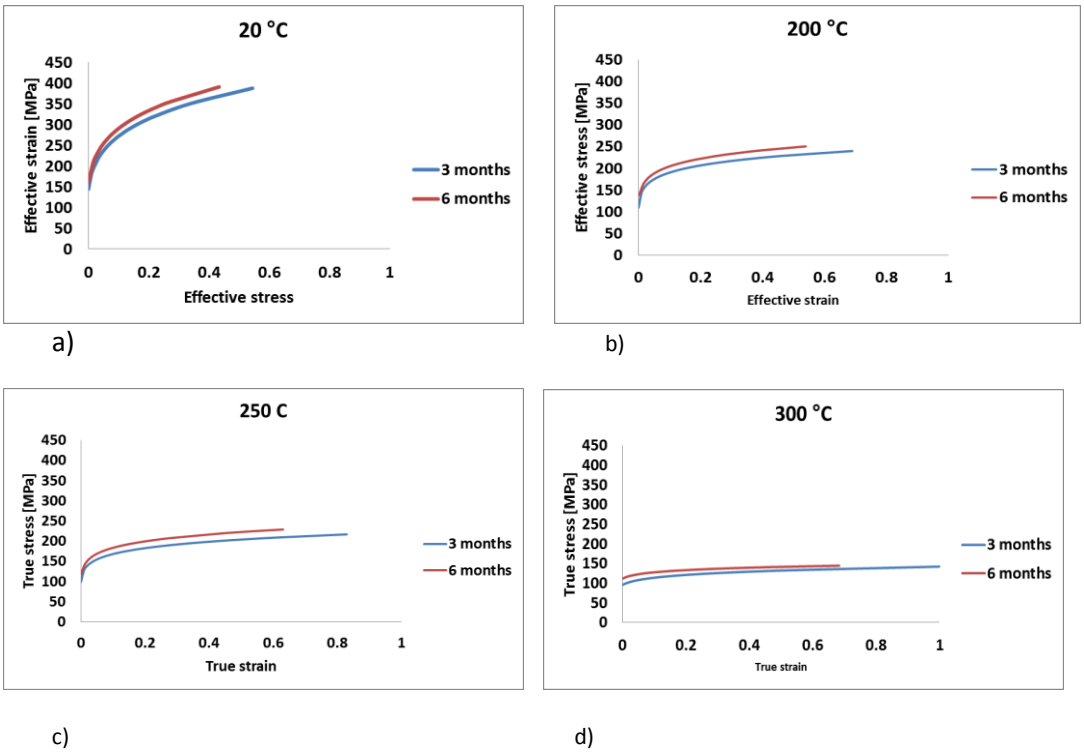

Figure 59: Comparison of flow curve at 3 and 6 months age: a) 25 ºC. b) 200 ºC. c) 250 ºC. d) 300 ºC.

It can be noticed that the strain at fracture increases with the temperature while the strain hardening coefficient decreases. The latter indicates the increases in ductility and decrease in work-hardening with the temperature. Moreover, it can be observed that the 3 months old material showed higher strain at fracture than the 6 months old material, in particular at high temperature. Figure 60 shows the fracture morphologies of the 3 and 6 months tensile specimens. It can be noticed that regardless of the ageing effect; the fracture surfaces show a dimple morphology which indicates ductile failure.

a) 3 months

b) 6months

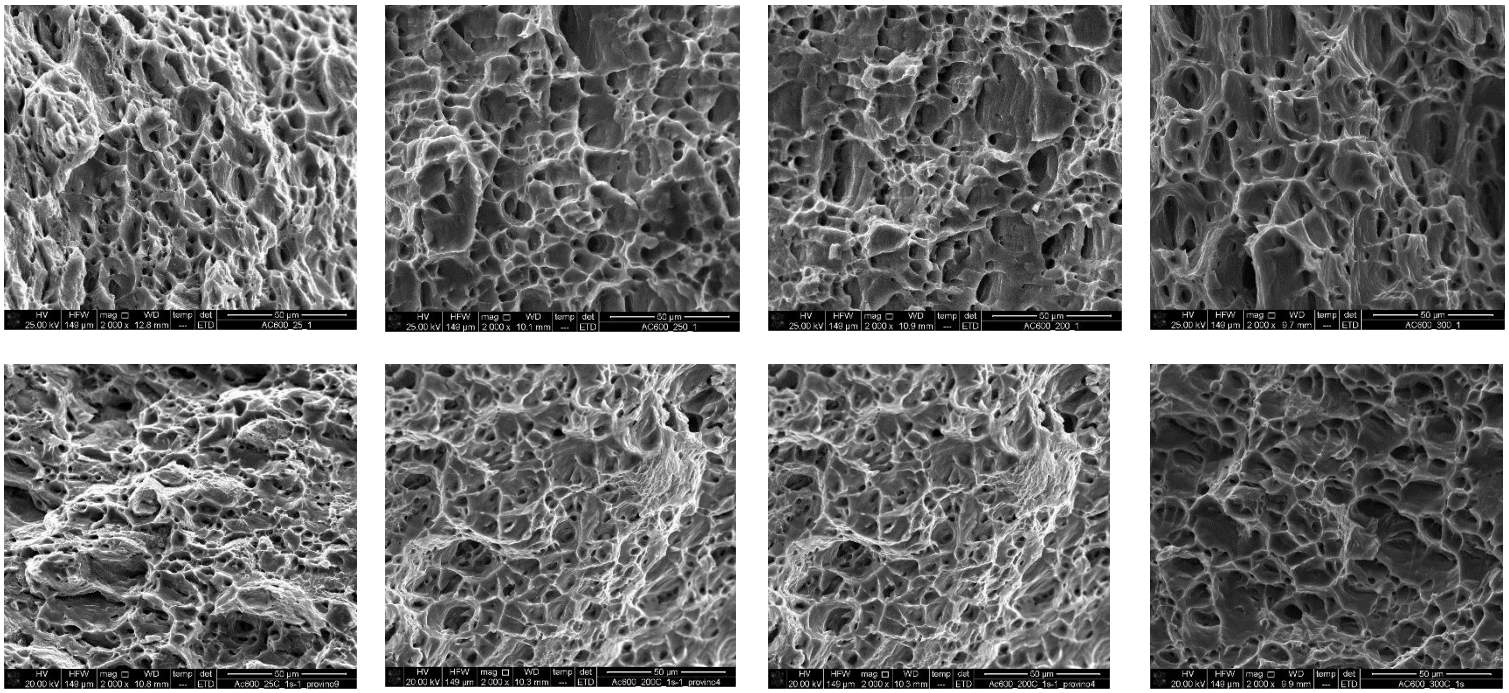

20 °C 200 °C 250 °C 300 °C

Figure 60: Effect of natural ageing and testing temperature on fracture morphology. a) 3 months, b) 6months

Table 16. Experimental parameters determined from tensile testing

Temperature [°C]	$Rp_{0.2}$ 3 Months [MPa]	$Rp_{0.2}$ 6 Months [MPa]	k 3 months [MPa]	k 6 months [MPa]	n 3 months	n 6 months	εf 3 months	εf 6 months
20	142	161	440	464	0.21	0.21	0.55	0.44
200	110	130	251	270	0.12	0.12	0.69	0.54
250	102	120	221	242	0.12	0.12	0.83	0.63
300	90	112	140	147	0.09	0.07	1.07	0.70

6.2.3 Effect of natural ageing on joint characteristics

The previous section has shown that the Novelis AC600 in temper T4 is affected by natural ageing, as a result its mechanical properties changes with time. In this context, as SPR is a mechanical joining process which involves the plastic deformation of the substrate materials, natural ageing can affect the SPR joint characteristics. A detailed study on the effect of paint baking and natural ageing on SPR joint strength was provided by (Han, 2003) where the aluminium alloy AA6111 T4 was used.

In this study, the effect of natural ageing on the change in joint characteristics of AC600T4 was investigated by means of SPR coupon tests performed at the age of three and six months . The SPR stacks used for this study are listed in Table 17 whilst the geometries of rivet and die are showed in Figure 46.

Table 17. List of SPR stacks

Stack No	*Mat 1*	*Thick 1 [mm]*	*Mat 2*	*Thick 2 [mm]*	*Die*	*Rivet*
1	**AC600 T4**	**2.5**	**AC600 T4**	**2.5**	**D (Flat)**	**7.0H4**
2	**RC5754**	**2**	**AC600 T4**	**2.5**	**C (Pip)**	**6.5H2**

The coupon tests were performed with a repetition of 20 samples for each joint and the same riveting parameters were applied for the three months and six months old material.

Figure 61 and 62 show the trends of T_{min} and Interlock respectively for the two stacks under investigation. It can be observed that, for the joints under investigation, the mean values of T_{min} increase with natural ageing. This behaviour indicates that the increase in strength due to the natural ageing affects the plastic deformation occurring during the SPR process which as a result changes the shape of the riveted joints. Figure 63 shows a comparison between the cross-sections of stack 1 obtained at month 3 and 6 respectively. It can be observed that the increase in natural ageing led to an increased gap between the rivet head and top sheet which indicates that the material is less prone to flow into the rivet bore as consequence of the increased strength and reduced ductility. Moreover, the increase in distance between the rivet tip

and the die side surface of the bottom layer can be justified by the greater flaring of the rivet legs which indicates the increased resistance of the substrate materials to the rivet penetration. The latter explains the increase in T_{min} and interlock values with natural ageing. Similar trends for interlock and T_{min} were observed in stack 2 where the top layer was made of AA5754 and the bottom layer was made of AC600T4 (Figure 64). However, in this case the difference in distance between the rivet tip and die side surface of the bottom layer was less than for stack 1. This result is in line with the choice of the AA5754 as top layer which is not affected by natural aging and therefore reduces the overall strengthening of the stack with time. Furthermore, it can be observed that no gaps between the rivet head and top sheet were observed due to the different die profile that was selected to enhance the plastic flow of the substrate materials into the rivet bore.

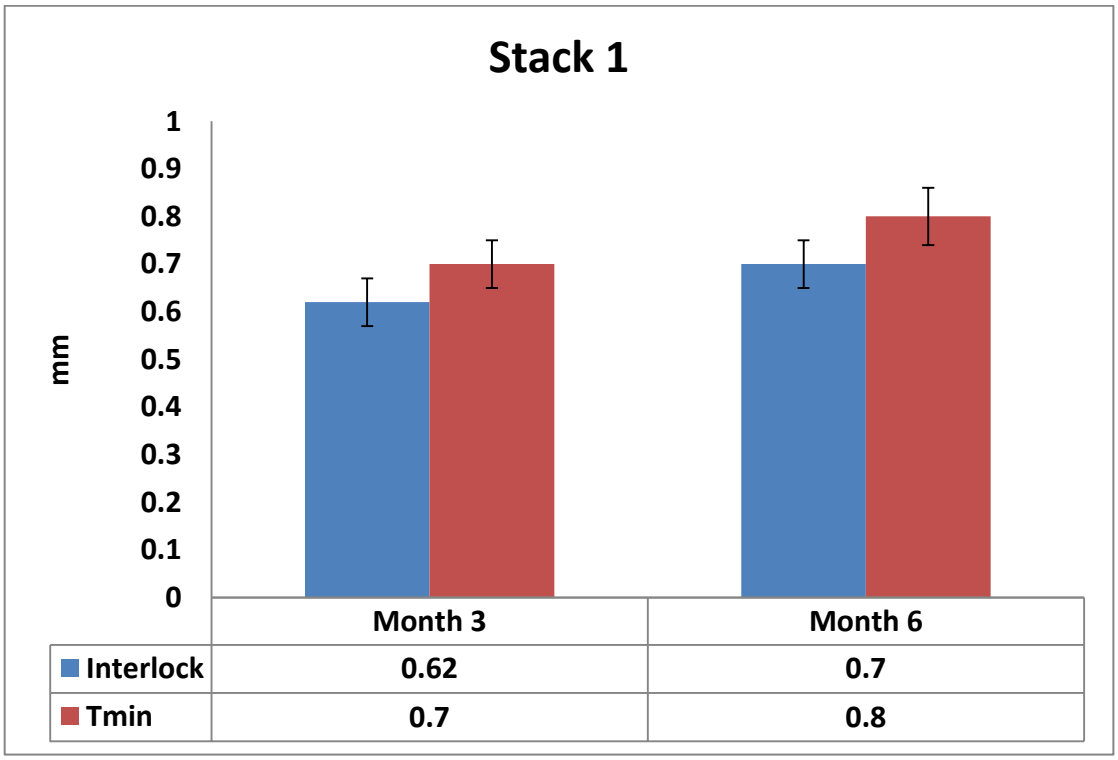

Figure 61: Effect of natural ageing on Tmin values for joint 1 (2.5mm AC600T4 + 2.5mm AC600T4)

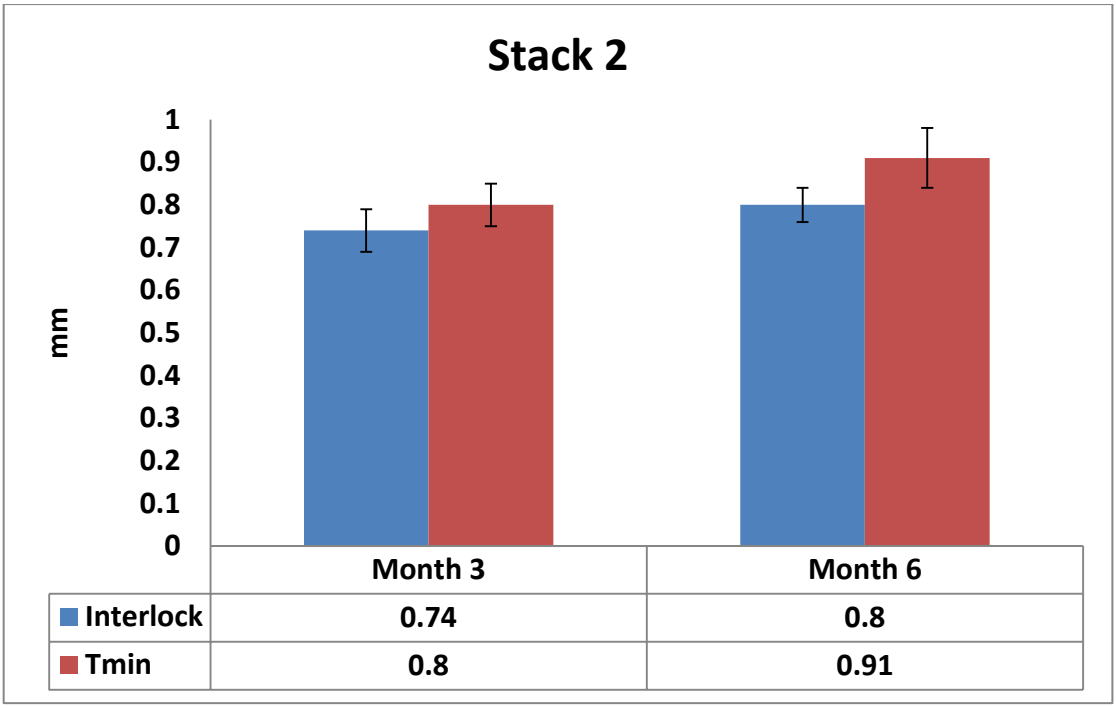

Figure 62: Effect of natural ageing on Interlock values for joint 2 (2mm AA5754 + 2.5mm AC600T4)

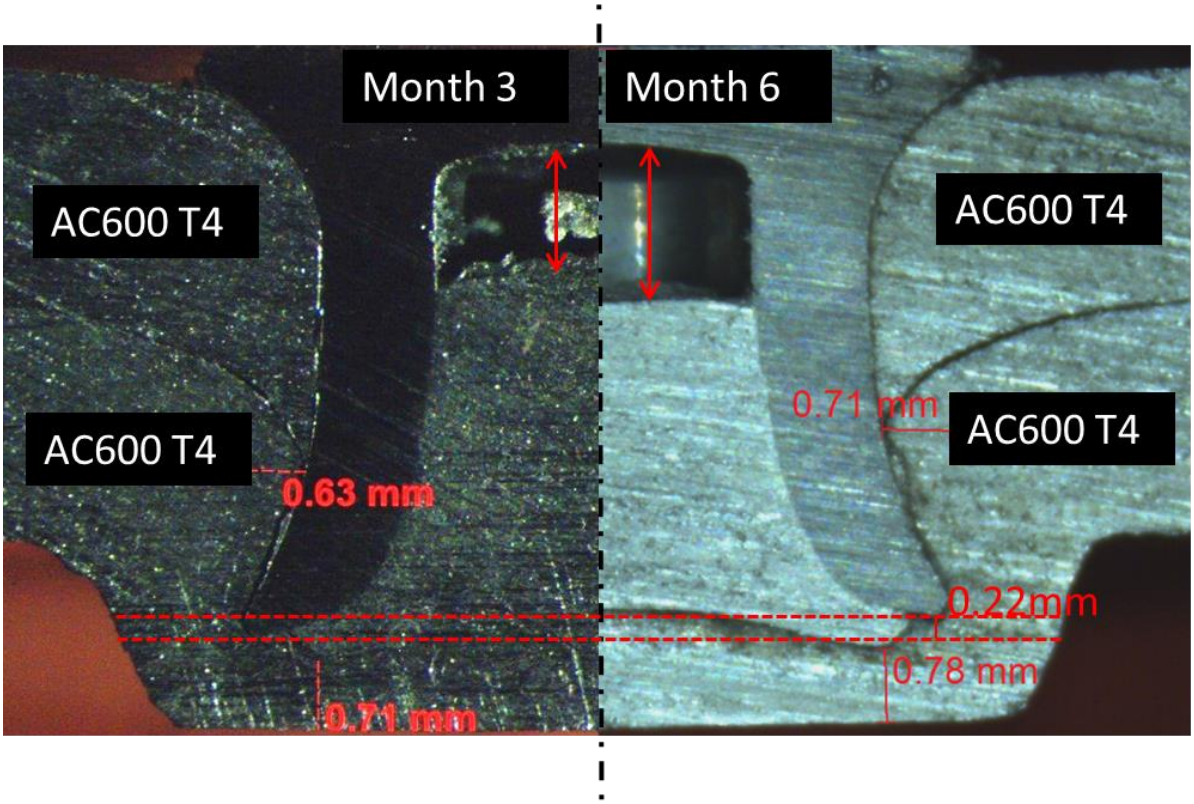

a) b)

Figure 63: SPR cross section geometries for stack 1 at: a) month 3 and b) month 6

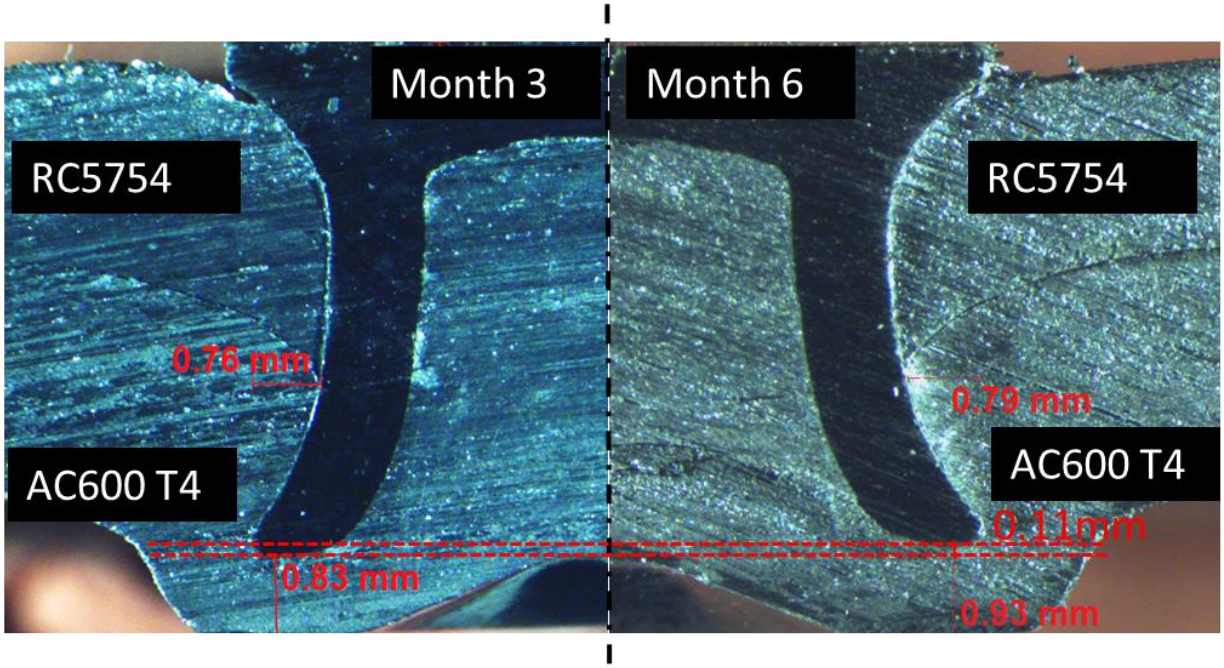

a) b)

Figure 64: SPR cross section geometries for stack 2 at: a) month 3 and b) month 6

6.2.4 Validation of the substrate material model

FE simulations using material data at 3 and 6 months were performed for the two joint configurations discussed in the previous section.

Figure 65 shows a comparison of the numerical cross-sections representative of stack 1 obtained using respectively 3 and 6 month material models. It can be observed that the gap between top layer and rivet head increases with natural ageing which is in agreement with the experimental results. As discussed in the previous paragraph, this result is justified by the reduced capability of the substrate material to flow into the rivet bore due to the increase in flow stress with ageing time. Figure 66 shows the overlapping of the two numerical cross sections which highlight that the increase in natural aging lead to higher plastic deformation of the rivet leg.

As shown in Figure 67, the numerical cross-sections reported a gap between the interface of rivet leg and top sheet (1) and another small gap between the interfaces of

the two sheets (2). Although, this behaviour was not evident in the original experimental cross-section (Figure 63), a more in depth analysis of a polished cross-section with a higher magnification optical microscope showed comparable results between numerical and experimental tests.

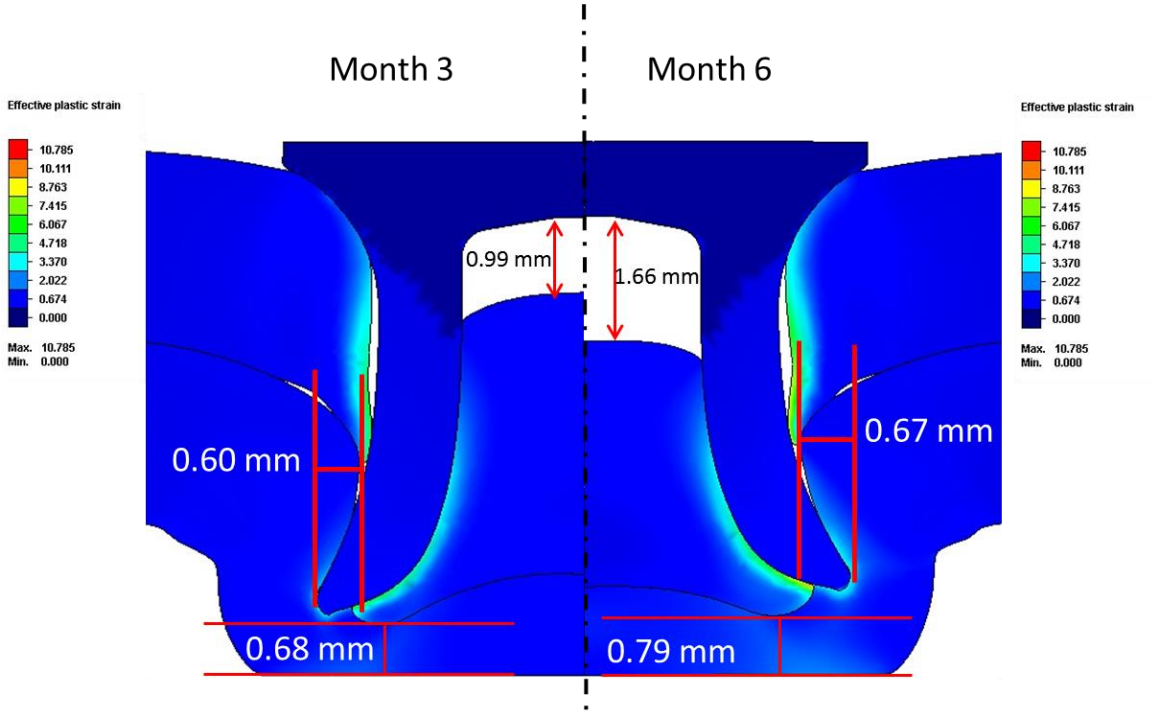

a) b)

Figure 65: Comparison of numerical SPR joint characteristics for stack 1: a)month 3 and b) month 6

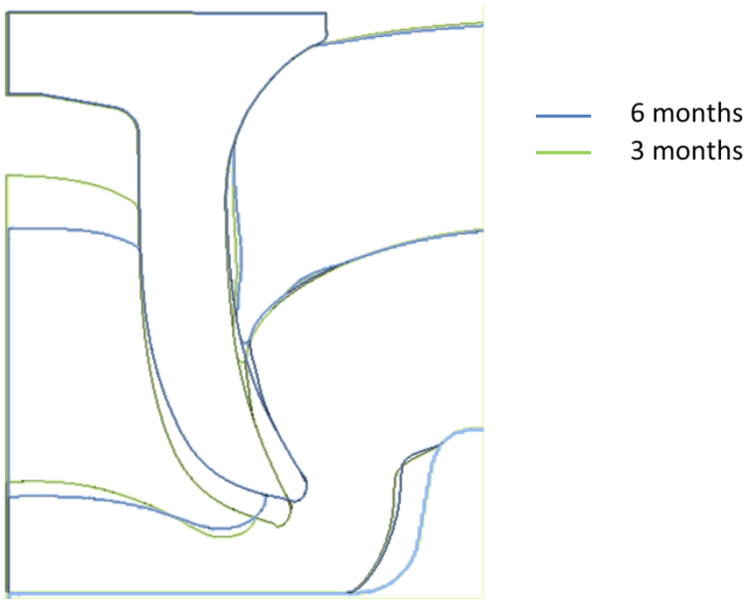

Figure 66: Comparison of numerical SPR cross-sections at 3 and 6 months for stack 1

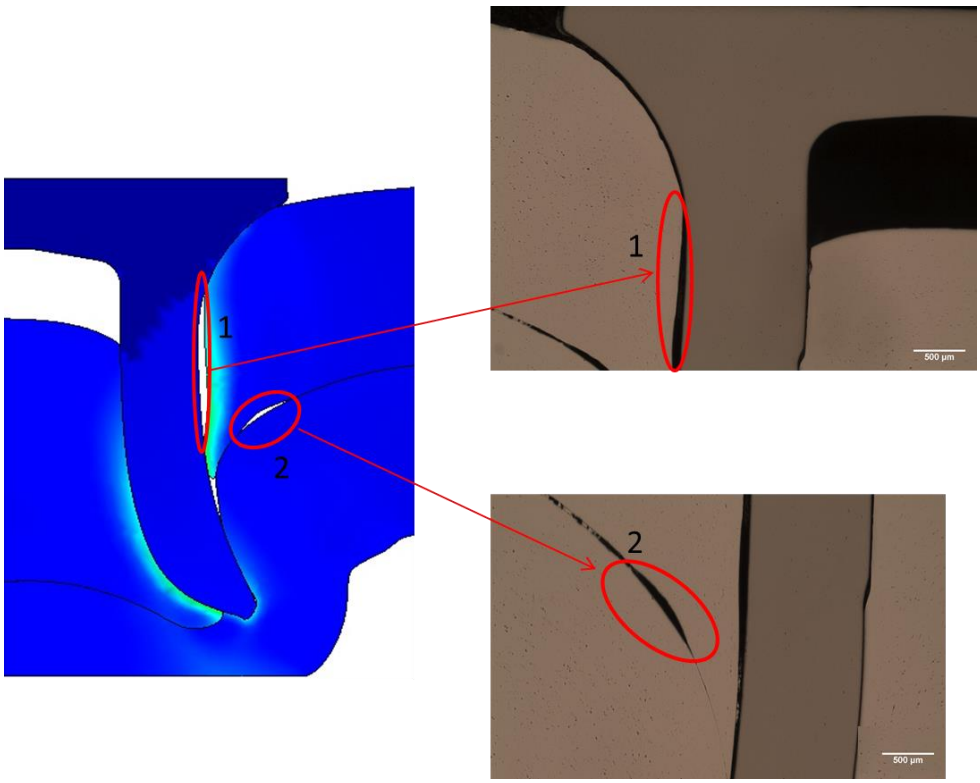

Figure 67. Comparison between numerical and experimental results for stack 1 showing gaps between rivet leg and substrate material (1) and top and bottom sheet (2)

Figure 68 shows a comparison of the numerical cross-sections representative of stack 2 obtained using material models representative of 3 and 6 months ageing respectively. It can be observed that in this case the two sections showed similar rivet flaring (Figure 69) which is also in agreement with the experimental observations reported (Figure 64). This result can be justified by the fact that only the bottom layer of the stack is made of AC600T4 whilst the material of the top layer was made of AA5754 aluminium alloy which is not affected by natural aging.

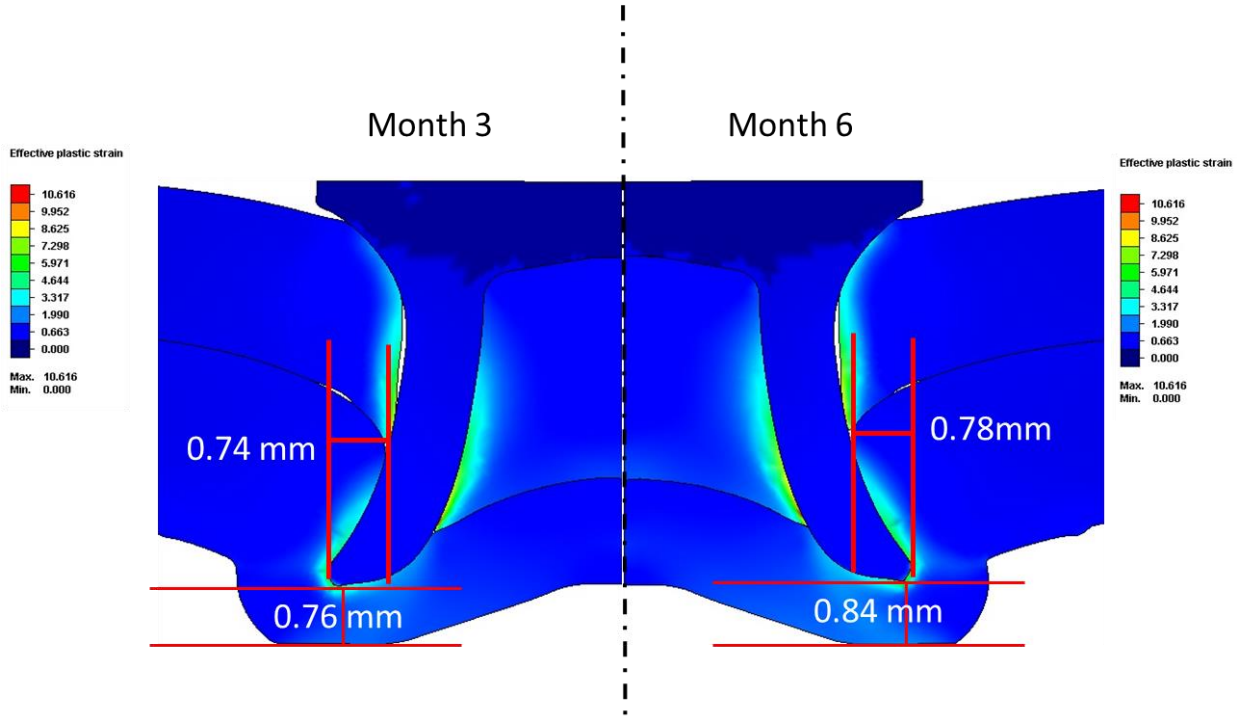

a) b)

Figure 68: Comparison of numerical SPR joint characteristics for stack 2: a)month 3, b) month 6

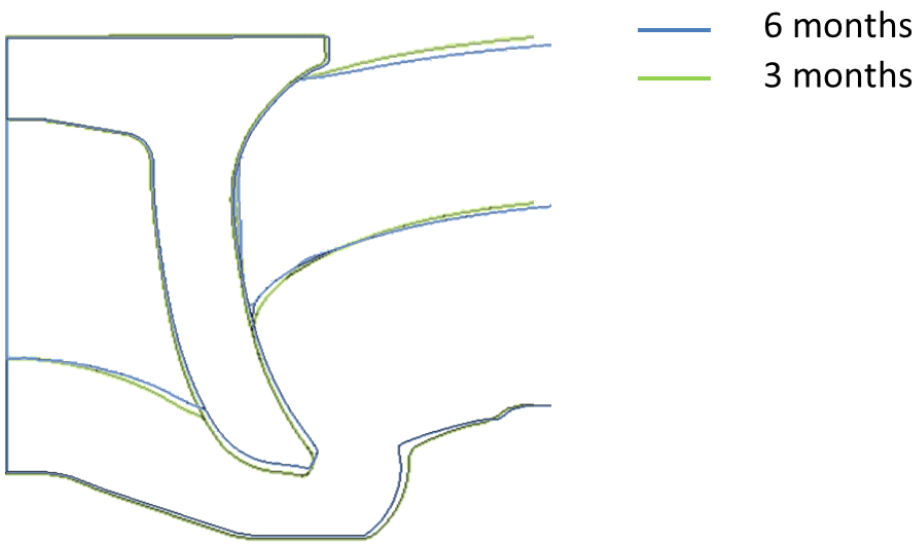

Figure 69: Comparison of numerical SPR cross-sections at 3 and 6 months for stack 1

The comparison between numerical and experiment joint characteristics are listed in Table 18 which indicates that a margin of error less than 0.1mm was found between experimental and predicted results.

Table 18: Comparisons between numerical and experimental joint characteristics

Joint / age	**Interlock experimental [mm]**	**Interlock numerical [mm]**	**Δ Interlock (exp.-num.) [mm]**	**T_{min} experimental [mm]**	**T_{min} numerical [mm]**	**Δ T_{min} (exp.-num.) [mm]**
1 / 3month	0.62 ± 0.05	0.6	0.02	0.7± 0.06	0.68	0.02
1 / 6 months	0.7± 0.05	0.67	0.03	0.8± 0.06	0.79	0.01
2 / 3month	0.74± 0.05	0.74	-	0.8± 0.05	0.76	0.04
2 / 6 months	0.8± 0.06	0.74	0.06	0.91± 0.06	0.84	0.07

These results showed that despite the natural ageing, the joint characteristics of a SPR joint, can be controlled via selection of suitable material stack design and rivet/die

combinations. In this context, the use of the developed simulation technique can be a powerful tool that can provide faster engineering recommendations on the material stack design and the selection of optimum rivet/die combinations.

7. Validation of the developed technique using a JLR vehicle platform

7.1 Method of the validation

To validate the simulation technique developed, a JLR vehicle platform has been used to prove the robustness and accuracy of the tool in predicting the SPR joint characteristics.
The test matrix used for the validation was characterized by over 100 SPR joint configurations made of 5xxx and 6xxx series alloys and representative of over 1000 of the joints used in vehicle BIW.

A numerical simulation was performed for each joint configuration and the simulated values of interlock and T_{min} were recorded. In order to assess the correlation between simulated and experimental values, linear regression analysis and regression plots were provided. The simulated values were compared with experimental mean values of interlock and T_{min} based on five repeats for each joint configuration.

7.2 Validation results

To assess the correlation between numerical and experimental results, linear regression models for both interlock and T_{min} were generated. The equation of a linear regression model is given by:

$$Y = A + BX \qquad (5)$$

In this case, the simulated values represent the predicted variables (Y-axis) whilst the experimental values (X-axis) represent the variables we are comparing the prediction to. This equation provides a line of best fit where A is the intercept and B is the slope. The values of A and B are determined through the least square method in order to minimize the error sum of square (ESS) (Mendenhall and Sincich, 1996):

$$ESS = \sum_{i=1}^{n} (y_i - \widehat{y_i})^2 \qquad (6)$$

where y_i represents the simulated results and $\widehat{y_i}$ represents the value estimated by the regression line. Thus, the difference between y_i and $\widehat{y_i}$ represents the prediction error (Mendenhall and Sincich, 1996):

$$e = y_i - \widehat{y_i} \qquad (7)$$

As in our case X and Y represents the same entities, for good correlation between numerical and experimental data it is expected that "A" is as close as possible to zero and "B" as close as possible to 1. The coefficients "A" and "B" determined from the linear regression models of both interlock and T_{min} are listed in Table 19:

Table 19: Coefficients A and B obtained from the linear regression model for both Interlock and T_{min}

	A	B
Interlock	**0.002**	**0.94**
T_{min}	**-0.03**	**1.035**

The values indicate that the fitted line plot exhibits a good approximation to the line with an intercept equal to zero and slope equal to one.

The agreement of a regression model is generally assessed by looking at two values: standard error (S) and coefficient of determination (R-sq).

The standard error indicates the average prediction error and is given by the square root of the mean square error (MSE) defined as (Mendenhall and Sincich, 1996):

$$MSE = \frac{\sum_{i=1}^{n}(y_i - \widehat{y_i})^2}{n-1} \qquad (8)$$

where the numerator is the error sum of square (ESS) while the denominator is given by the sample numbers minus the number of degrees of freedom. The coefficient of determination, instead, indicates the percentage of variation in Y which is explained by the variation of the predictor X. This means that the greater is R-sq the more are the number of data points that fall perfectly on the regression line.

Table 20 lists the values of S and R-sq carried out from the two regression models:

Table 20: standard error (S) and coefficient of determination (R-sq) for Interlock and T_{min}

	S [mm]	R-sq [%]
Interlock	**0.064**	**90.2**
T_{min}	**0.090**	**93.6**

It was observed that the R-square values are above 90% in both the cases which indicate good correlation between the simulation and the experimental results. Moreover, the standard error reported by Interlock was about ±0.06 while T_{min} showed an error of ±0.09.

Figures 70 and 71 show the fitted line plot obtained with the regression models respectively for Interlock and T_{min} and highlight that the majority of data fall within the prediction intervals.

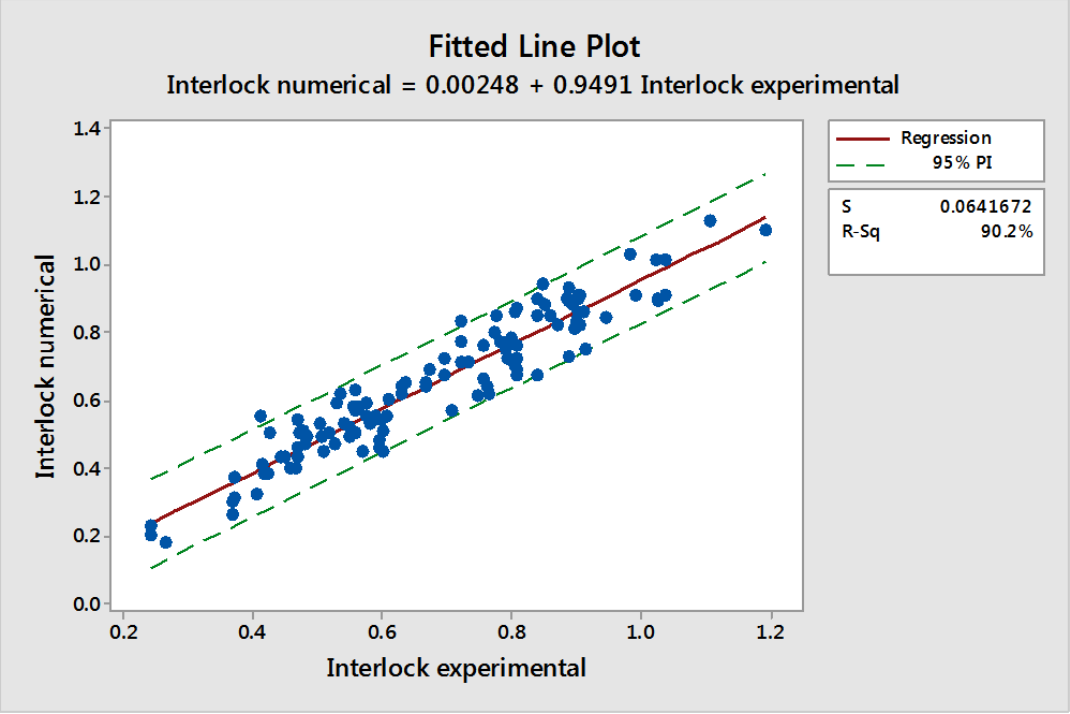

Figure 70: Fitted line plot obtained from the linear regression model between Interlock numerical and Interlock experimental

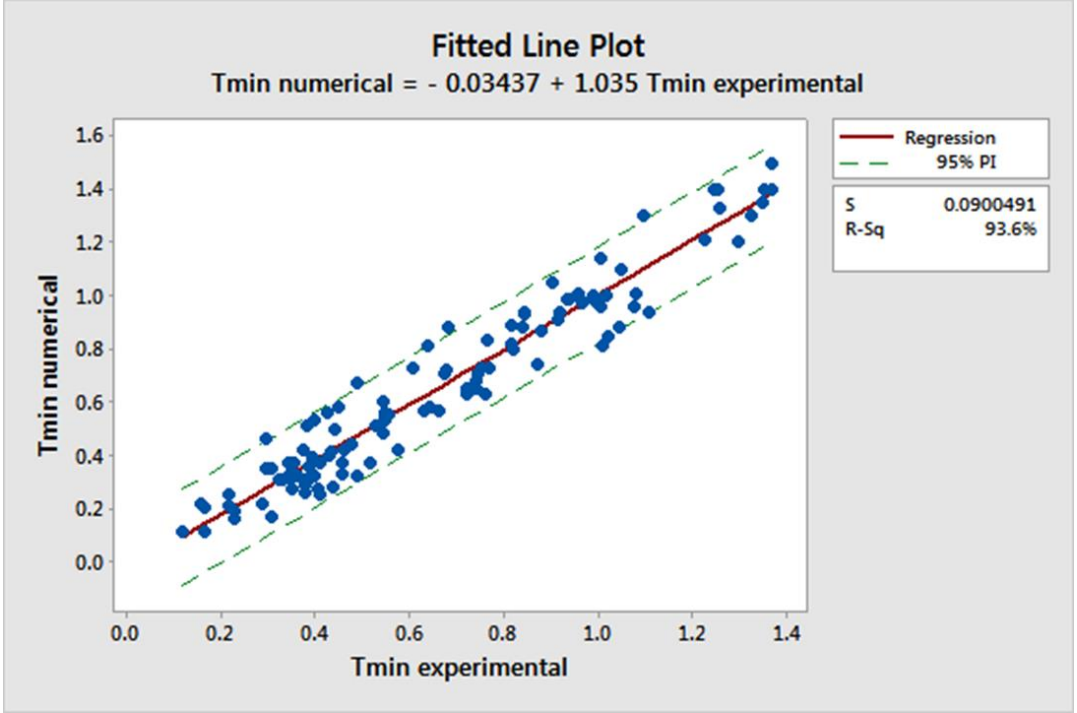

Figure 71: Fitted line plot obtained from the linear regression model between T_{min} numerical and T_{min} experimental

Figures 72 and 73 show the residual plots for the Interlock distance and T_{min}. The residual indicates the difference between the numerical and experimental values. Figure 73b shows the normal probability plot for Interlock which indicates that 90% of the residuals fall within the range of ±0.1mm whilst in the case of T_{min} the range is ±0.15mm (Figure 74b).

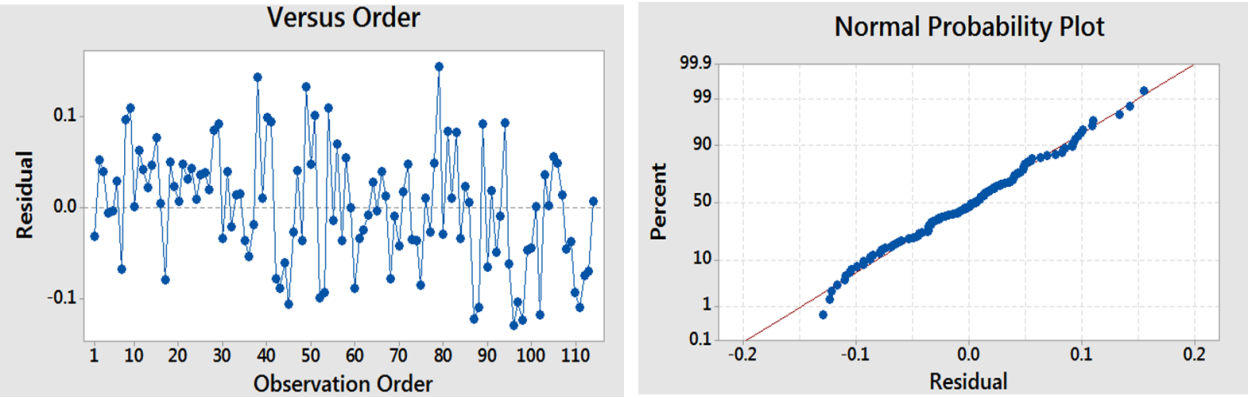

a) b)

Figure 72: Residual plots for interlock. a) Versus order, b) Normal probability plot

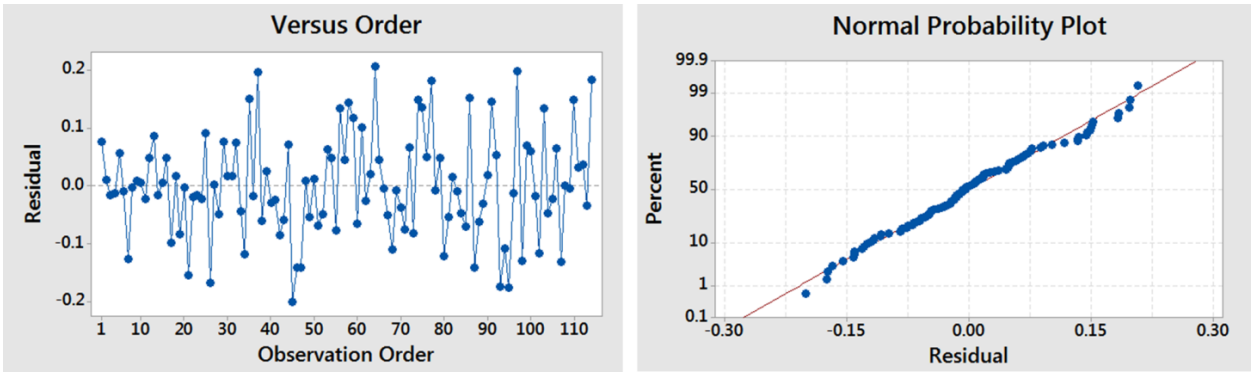

a) b)

Figure 73: Residual plots for interlock. a) Versus order, b) Normal probability plot

The results are relevant if considering that several bias factors might affect the experimental results such as material batch variation, age hardening, tooling tolerances / wearing and human error during experimental measurements. Moreover, as indicated in Figure 74 and 75, the residuals for both interlock and T_{min} follow a normal distribution centred around zero.

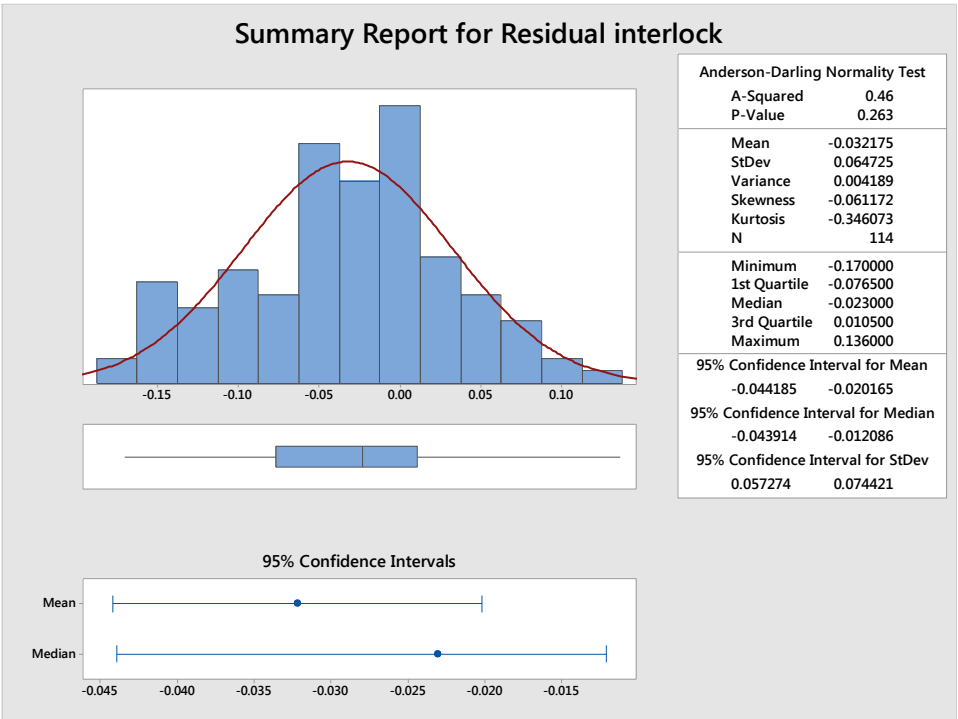

Figure 74: Normal distribution of Interlock residual

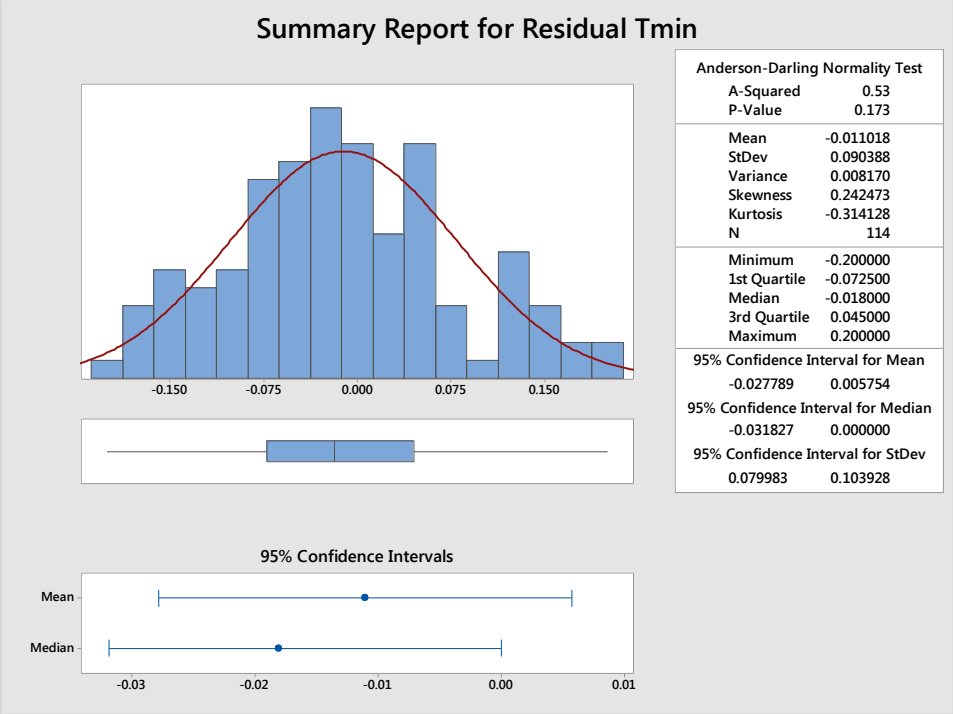

Figure 75: Normal distribution of Tmin residual

8. Industrial benefits and Research dissemination

This study has developed a simulation technique for prediction of the SPR joint characteristics in a timely fashion and high correlation between the simulation and the experimental tests results has been achieved. These innovations, coupled with the high robustness of the technique, make its application possible within a manufacturing environment bringing several benefit to the business:

1) Reduced time:

One of the main innovations is the significant reduction of time in comparison to the experimental tests. Figure 76 shows a flow chart indicating all the steps involved in the experimental process. It starts with the order of the material blanks for each different material grade and gauge. These need to be cut in the shape of 40mmx40mm coupons and then sent to the supplier for coupon tests to be performed.

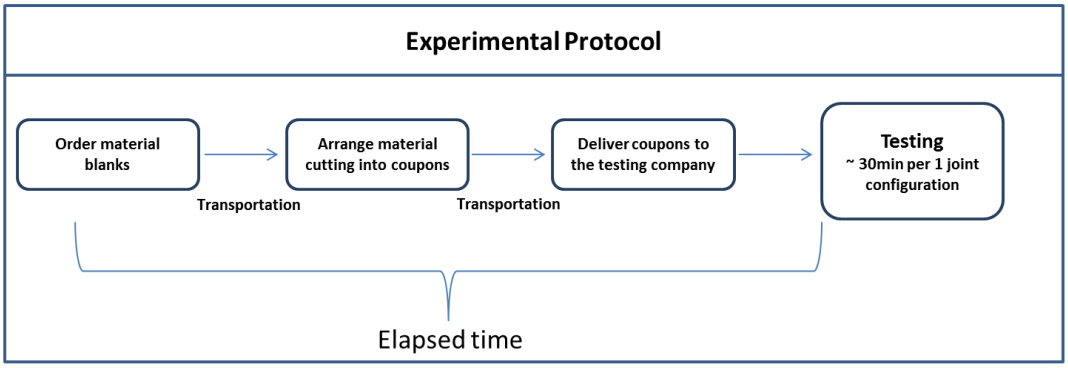

Figure 76: Time flow with experimental method

In contrast to the experimental tests, the simulation technique only matches the "testing" with its virtual testing thus eliminating the elapsed time, as indicated in Figure 77. In addition, virtual testing, only requires a fraction of the time needed for the experimental testing. For example, a typical joint, normally requires 30 minutes for experimental testing alone, while the current virtual test method can deliver the results for three joint configurations within 15 minutes using a common 8 CPUs machine.

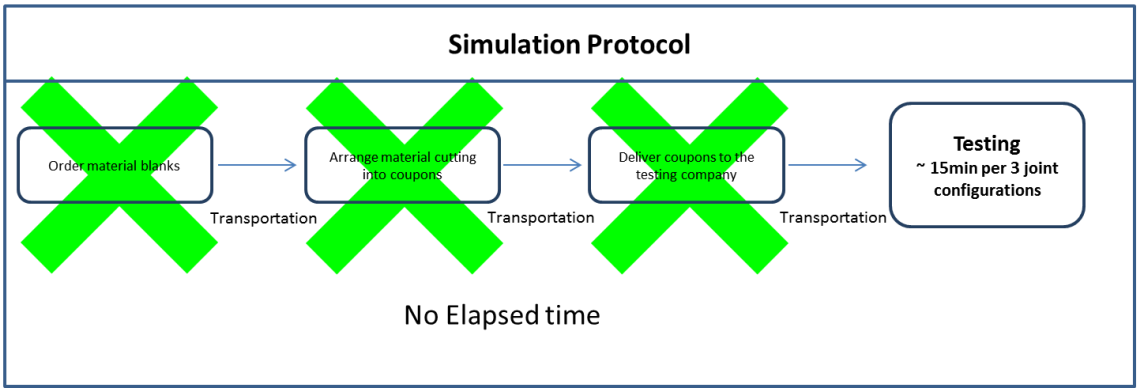

Figure 77: Time flow with simulation method

2) Smooth implementation:

The time savings, accuracy and robustness of the developed simulation technique could allow achieving more robust implementation of the SPR process by providing engineering recommendation rapidly and consistently. The latter is extremely

important for the business in the case where re-testing or re-processing of joint configurations is required during vehicle implementation.

3) Reduced costs:

Despite the benefit of time reduction, the simulation technique would also enable significant reduction of engineering investment due to the decrease in labour and materials requirement for coupon testing

4) Environmental impact & Safety:

The application of the developed simulation technique will reduce usage of heavy duty equipment, intensive labour, material and transportation which were involved in experimental tests. Therefore, it allows protecting humans ergonomically by saving energy consumption and CO_2 emissions.

All these features, combined with the accuracy and robustness have enabled the application of the developed tool into JLR business. Due to the commercial sensitive nature of the data, detailed information about costs and time savings are omitted in this report. However, these business benefits are emphasized by the fact that the developed simulation technique is currently being used by one of JLR strategic programmes for new model development.

The innovation and contribution to the knowledge provided by this research are demonstrated by several achievements which enable the dissemination of this research:

Publication - Journal of Material Processing and Technology

- Title: Improvements in numerical simulation of the SPR process using thermo-mechanical finite element analysis

Award:

- Jaguar Land Rover Innovista Award 2016
    - Finalist in the category of Promising Innovations

Conference presentation:

- Joining in car body engineering, March 2015, Bad Nauheim, Germany
    - Title: Feasibility evaluation of self-pierce riveting process

- Joining in car body engineering, April, 2016, Bad Nauheim, Germany
    - Title: Challenges in application and simulation of Self-pierce riveting process

9. Conclusions

This research has developed a novel simulation technique for the SPR process and enabled simulation and prediction of SPR joint characteristics.

The outcome of this study has produced a 2d axisymmetric model which allows short CPU time (~15 minute x 3 joints in parallel) and high accuracy and robustness. These have been proved by validating the technique using more than 1000 joints taken from a JLR vehicle platform.

The simulation technique developed is based on new inventions which consider thermo-mechanical finite element analysis for simulation of the SPR process. By incorporating key mechanical properties of the substrate material such as, thermal softening and strain hardening, as well as accurate development of the finite element models, good agreement between numerical and experimental results have been achieved. It has been shown that by ignoring these material features, serious errors in the numerical solution related to higher resistance of the substrate material to the rivet penetration, will occur.

In the absence of thermal softening the deformation of rivet leg and T_{min} values (key feature in determining the integrity of the joint) can significantly be over-predicted. The heating generated during the SPR process was also confirmed with experimental tests using infrared thermography. The project has also revealed insights on the effect of frictional force on the deformation mechanism of a SPR joint. It was found that by increasing of friction coefficient, the rivet is less prone to flare and goes deeper into the bottom layer. This result could trigger the development of new coatings with specific coefficient of friction to achieve desired flaring behaviour of the SPR rivets.

Thermo-mechanical material models have been developed for 5xxx and 6xxx series aluminum alloys which constitute the majority of the materials in a typical JLR lightweight body structure. The effect of natural aging on the rivetability for 6xxx-T4 aluminium alloy has been studied. It was found that due to precipitation hardening, a strengthening mechanism caused by the precipitation of Mg_2Si needle particles, the ability of the material to plastically deform during the SPR process was affected. Such effect was also reproduced in the FE simulation by developing material models representative of different age.

The developed simulation technique brings significant business benefits such as: time and cost savings, smother implementation and positive environmental impact in comparison to the experimental coupon tests.

10. Future work

The FE model developed in this study has been validated for a 5xxx and 6xxx series aluminium alloys, therefore, the application to different grades of materials used in automotive industry such as casting, extrusion and steel would require further consideration on their plastic behaviour under riveting conditions. One of the main concerns would be the modelling of the top layer splitting. In this study, an erosion element technique has been used and it was proved to be a good approximation in the case of materials which exhibit sufficient ductility. However, in the case of brittle materials, this assumption might be a constraint due to possible crack propagation occurring during the rivet insertion. In this case, an appropriate damage model would be required. A preliminary investigation on this subject has already started using the Johnson-Cook damage model which considers the strain at fracture as a function of stress triaxiality, strain rate and temperature (Johnson and Cook, 1985). Figure 78 shows an application of this model for simulation of cracking issues generated during the rivet insertion.

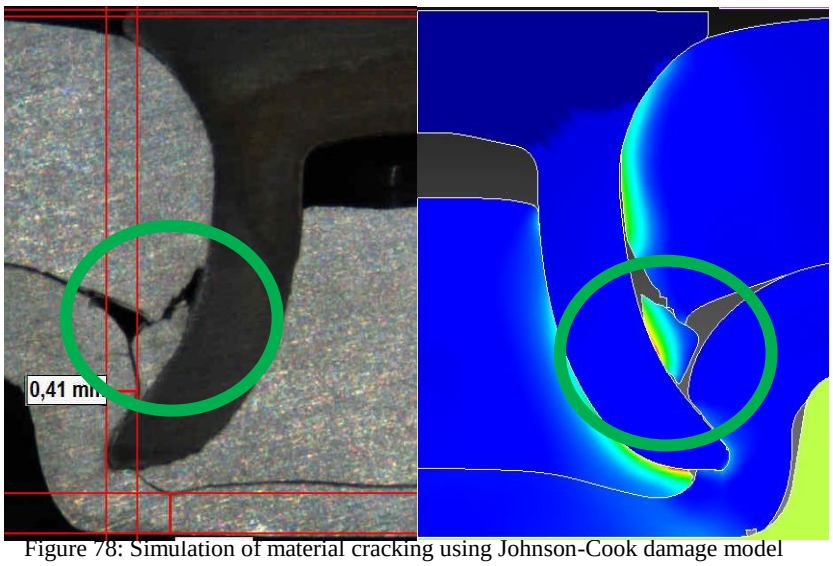

Figure 78: Simulation of material cracking using Johnson-Cook damage model

This model is still under development and its robustness for different material stacks and rivet die/combinations need to be proved.

The modelling of friction behaviour constitutes another challenge to take into account during simulation of the SPR process. Inverse analysis method to determine friction coefficients are widely used due to the difficulties in measuring the friction forces by in-situ methods. However, as SPR involves several interfaces coming into contact, a good understanding of the frictional behaviour is fundamental for a robust numerical simulation. Indeed, factors like die wear, material lubricants and variation in rivet coating can all affect the joint characteristics.

Finally, as SPR is used quite often in combination with adhesives, the development of a finite model, which takes into the effect of adhesive in Riv-bonding application and considers the variation in joint characteristics is beneficial for the automotive industry.

References

ABEDRABBO, N., POURBOGHRAT, F., & CARSLEY, J., 2006. Forming of aluminum alloys at elevated temperatures – Part 1: Material characterization. Int. J. Plasticity 22 (2), 314–341.

ABEDRABBO, N., POURBOGHRAT, F., & CARSLEY, J., 2007. Forming of AA5182-0 and AA5754-0 at eleveted temperatures using coupled thermo-mechanical finite element models. *International Journal of Plasticity.* 23**,** 841–875.

AMBROZIAK, A. & KORZENIOWSKI, M. 2010. Using Resistance Spot Welding for Joining Aluminium Elements in Automotive Industry. *Archives of Civil and Mechanical Engineering,* 10**,** 5-13.

AWANG, M., MUCINO, V. H., FENG, Z., & DAVID, S. A., 2005. Thermo-mechanical modelling of friction stir sot welding (FSSW) process: Use of an explicit adaptive meshing scheme. SAE International. 01-1251

ARCHARD, J., 1959. The temperature of rubbing surfaces. Wear. 2, 438–455

BARNES, T. A. & PASHBY, I. R. 2000a. Joining techniques for aluminium spaceframes used in automobiles: Part I — solid and liquid phase welding. *Journal of Materials Processing Technology,* 99**,** 62-71.

BARNES, T. A. & PASHBY, I. R. 2000b. Joining techniques for aluminium spaceframes used in automobiles: Part II — adhesive bonding and mechanical fasteners. *Journal of Materials Processing Technology,* 99**,** 72-79.

BLOECK, M., 2012. Chapter 5 – Aluminium sheet for automotive applications*. Advanced materials in automotive engineering*. Rowe, J., Woodhead publishing limited

BOOMER, D. R., HUNTER, J. A., & CASTLE, D. J., T., HOPPERSTAD, O. S., BERSTAD, T. & LANGSETH, M. 2001. A new approach for robust high productivityresistance spt welding of aluminium.SAE technical paper 2003-01-0575.

BOOTH, G., OLIVIER, C., WESTGATE, S., & LIEBRECHT, F., 2000. Self-piercing riveted joints and resistance spot welding joints in steel and aluminium. SAE technical paper 2000-01-2681.

BOVRIK, T., HOPPERSTAD, O. S., BERSTAD, T., & LANGSETH, M., 2001. A computational model of viscoplasticity and ductile damage for impact and penetration. *European Journal of Mechanics – A/Solids.* 20, 685-712

BOUCHARD, P. O., LAURENT, T. & TOLLIER, L. 2008. Numerical modeling of self-pierce riveting - From riveting process modeling down to structural analysis*. Journal of Materials Processing Technology,* 202**,** 290-300.

BRISKHAM, P., BLUNDELL, N., HAN, L., & BOOMER, D. J., 2006. Comparison of self-pierce riveting, resistance spot welding and spot friction joining for aluminium automotive sheets. SAE technical paper 2006-01-0774.

CAMPBELL, F. C. 2006. Chapter 8 - Adhesive Bonding and Integrally Cocured Structure. *Manufacturing Technology for Aerospace Structural Materials.* Oxford: Elsevier Science.

CAMPBELL, F. C. 2011. Chapter 1: Introduction to joining. *Joining: understanding the basics.* ASM.

CAOE, L., ROMETSECH, P. A., & COUPER, M. J., 2012. Clustering behaviour in Al-Mg-Si-Cu alloy during natural ageing abd subsequent under ageing. Materials science & engineering A. 599, 257-261

CARANDENTE, M., DASHWOOD, R. J., MASTERS, I. G., & HAN, L., 2016. Improvements in numerical simulation of the SPR process using a thermo-mechanical finite element analysis. Journal of Material Processing Technology. 236, 148-161

CASALINO, G., ROTONDO, A. & LUDOVICO, A. 2008. On the numerical modelling of the multiphysics self piercing riveting process based on the finite element technique. *Advances in Engineering Software,* 39**,** 787-795.

CHENOT, J. L. & MASSONI, E. 2006. Finite element modelling and control of new metal forming processes. *International Journal of Machine Tools and Manufacture,* 46**,** 1194-1200.

CHRYSANTHOU, A., 2014. Chapter 1: Introduction. *Self-piercing riveting: Properties, Processes and Applications.* ASM. A. Chrysanthou and X. Sun, Editors, Woodhead Publishing. p. 1-7.

DAVIES, G. 2012a. Chapter 2 - Design and material utilization. *Materials for Automobile Bodies.* Oxford: Butterworth-Heinemann.

DAVIES, G. 2012b. Chapter 6 - Component assembly: materials joining technology. *Materials for Automobile Bodies.* Oxford: Butterworth-Heinemann.

DI FRANCO, G., FRATINI, L. & PASTA, A. 2013. Analysis of the mechanical performance of hybrid (SPR/bonded) single-lap joints between CFRP panels and aluminum blanks. *International Journal of Adhesion and Adhesives,* 41**,** 24-32.

FAYOLLE, S., 2008. Modelisation numerique de la mise en forme et de la tenue mecanique des assemblages par deformation plastique : application au rivetage auto-poinconneur., *in PhD thesis.* Ecole Nationale Superieure des Mines de Paris.

FARREN, W., & TAYLOR, G., 1925. The heat developed during plastic extension of metals. Proceedings of the Royal Society of London. Series A 107, 422–451

HAN, L., 2003. Mechanical behaviour of self-piercing riveted aluminium joints, *in PhD thesis.* University of Hertfordshire.

HAN, L., M. THORTON & SHERGOLD M., 2009. A comparison of the mechanical behaviour of self-piercing riveted and resistance spot welded aluminium sheets for the automotive industry. Materials and Design, 31, 1457–1467

HAN, L., THORNTON, M., BOOMER, D. & SHERGOLD, M. 2010. Effect of aluminium sheet surface conditions on feasibility and quality of resistance spot welding. *Journal of Materials Processing Technology,* 210**,** 1076-1082.

HAYAT, F. 2011. Comparing Properties of Adhesive Bonding, Resistance Spot Welding, and Adhesive Weld Bonding of Coated and Uncoated DP 600 Steel. *Journal of Iron and Steel Research, International,* 18**,** 70-78.

HE, X., PEARSON, I. & YOUNG, K., 2008. Self-pierce riveting for sheet materials: State of the art. *Journal of Materials Processing Technology,* 199**,** 27-36.

HE, X., PEARSON, FENGSHOU, G., & BALL, A., 2012. Recent development in finite element analysis of self-piercing riveted joints. The International *Journal of Advanced Manufacturing Technology,* 58**,** 643-649.

HOANG, N. H., PORCARO, R., LANGSETH, M. & HANSSEN, A. G., 2010. Self-piercing riveting connections using aluminium rivets. *International Journal of Solids and Structures,* 47**,** 427-439.

HOANG, N. H., LANGSETH, M., PORCARO, R., & HANSSEN, A. G., 2011. The effect of the riveting process and ageing on the mechanical behaviour of an aluminium self-piercing riveted connection. *European Journal of Mechanics – A/SOLIDS***.** 30, 619-630.

HOANG, N. H., HOPPERSTAD, O. S., LANGSETH, M., & WESTERMANN, I., 2013. Failure of aluminium self-piercing rivets: An experimental and numerical study. *Materials & Design***.** 49, 323-335.

HOLST, G. C., 2000. Common sense approach to thermal imaging. SPIE Optical Engineering Press. Bellingham WA, ETATS-UNIS

HOU, W., MANGIALARDI, E., HU, S. J., WANG, P. C., & MANESS, R., 2004. Characterization for quality monitoring of a self-piercing riveting process. *Engineering fracture mechanics.* 21, 31-48

JONSON, G. R., & COOK, W. H., 1985. Fracture characteristics of three metals subjected to various strains, strain rates, temperature and pressures. *Journal IN: Proceeding of the Sheet Metal Welding conference XI, Sterling Heights, mi, Paper No. 8-3.*

MUKHOPADHYA, P., 2012. Alloy designation, processing and use of AA6XXX series aluminium alloys. ISRN Metallurgy

KABRIAN, F., KHAN, A., & PANDEY, A., 2014. Neagtive to positive strain rate sensitivity in 5xxx series aluminium alloys: Experiment and constitutive modeling. International Journal of Plasticity, 55, 232-246.

KAPOOR, R., & NEMAT-NASSER, S., 1998. Determination of temperature rise during high strain rate deformation. *Mechanics of Materials*. 27, 1-12

KING, F., 1987. Chapter 5 – Properties of aluminium alloys. Aluminium and its alloys. Ellis Horwood limited

KING, R. P., 1995. Setting load requirements and fastening strenght in the self-pierce riveting process. *In Proceedings of the 11th National Conference on Manufacturing Research,* UK. 57 - 61.

KING, R. P., 1997. Analysis and quality monitoring self-pierce riveting process, *in PhD thesis.* University of Hertfordshire.

LI, D., & GHOSH, A. 2003. Tensile behaviour of aluminium alloys at warm forming temperatures. *Materials Science and Engineering,* A352**,** 279-286.

LI, D., CHRYSANTHOU, A., PATEL, I, & WILLIAMS, G., 2016. Self-piercing riveting- a review. Working paper. Coventry: University of Warwick, WMG

LUYTSEY, N. 2010. Review of technical literature and trends related to automibile mass-reduction technology. University of California.

MAYYAS, A., SHEN, Q., MAYYAS, A., ABDELHAMID, M., SHAN, D., QATTAWI, A. & OMAR, M. 2011. Using Quality Function Deployment and Analytical Hierarchy Process for material selection of Body-In-White. *Materials & Design,* 32**,** 2771-2782.

MENDENHALL, W., SINCICH, T., & BOUDREAU, S. 1996. Chapter 3 – Simple linear regression. A secound course in statistics: regression analysis. Vol. 5. Upper Saddle River eNew Jersey: Prentice Hall

MESCHUT, G., LANZEN, V., & OLFERMANN, T. 2014. Innovative and higly productive joining technologies for multi-material lightweight car body structures. Joornal of Materialsn Engineering and Performance*,* 23**,**1515-1523.

MESSLER JR, R. W. 2004. Chapter 1 - Introduction to Joining: A Process and a Technology. *Joining of Materials and Structures.* Burlington: Butterworth-Heinemann.

MICHALOS, G., MAKRIS, S., PAPAKOSTAS, N., MOURTZIS, D. & CHRYSSOLOURIS, G. 2010. Automotive assembly technologies review: challenges and outlook for a flexible and adaptive approach. *CIRP Journal of Manufacturing Science and Technology,* 2**,** 81-91.

MORI, K., KATO, T., ABE, Y. & RAVSHANBEK, Y., 2006. Plastic Joining of Ultra High Strength Steel and Aluminium Alloy Sheets by Self Piercing Rivet. *CIRP Annals - Manufacturing Technology,* 55**,** 283-286.

MORI, K.-I., BAY, N., FRATINI, L., MICARI, F. & TEKKAYA, A. E. 2013. Joining by plastic deformation. *CIRP Annals - Manufacturing Technology,* 62**,** 673-694.

MORTIMER, J. 2001. Jaguar uses X350 car to pioneer use of self-piercing rivets. *Industrial Robot,* 28**,** 192-198.

MARC, 2013. Theory and users information. Volume A.

MARC, 2013. Theory and users information. Volume C.

MUCHA, J. 2011. A study of quality parameters and behaviour of slef-piercing riveted aluminium sheets with different joining conditions. *Journal of Mechanical Engineering.* 57**,** 323-333.

PEREZ-CATELLANOS, J. L., 2012. Temperature increase associated with plastic deformation under dynamic compression: application to aluminium alloy AL 6082. Journal of theoretical and applied mechanics. 2, 377-398

POLMEAR, I. J., 2004. Aluminium alloys – A century of age hardening. Materials Forum. Volume 28

PORCARO, R., HANSSEN, A. G., LANGSETH, M. & AALBERG, A. 2006. The behaviour of a self-piercing riveted connection under quasi-static loading conditions. *International Journal of Solids and Structures,* 43**,** 5110-5131.

ROGERS, H. C., 1979. Adiabatic plastic deformation. *Annual Reviews Materials Science*. 9, 283-311

SMITHELLS, C. J., 1990. Chapter 14 – General physical properties. Smithells Metals Reference Book. Gale W. F., & Totemeier T. C., pp. 1-43

STEPHENS, E. V, 2014. Chapter 2: Mechanical stenght of self-piercing riveting (SPR). *Self-piercing riveting: Properties, Processes and Applications.* ASM. Chrysanthou A. & Sun X. Woodhead Publishing. p. 11-32.

TAKEDA, M., OHKUBO, F. & SHIRAI, T., 1998. Stability of metastable phases and microstructures in the ageing process of AL-Mg-Si ternary alloys.

WEBER, A., 2015. Assembling Ford's aluminium wonder truck, in Assembly.